2012

Proton dose calculations in homogeneous media

John Wesley Chapman, Jr.
Louisiana State University and Agricultural and Mechanical College, jw_chapman@hotmail.com

PROTON DOSE CALCULATIONS IN HOMOGENEOUS MEDIA

A Thesis

Submitted to the Graduate Faculty of the
Louisiana State University and
Agricultural and Mechanical College
in partial fulfillment of the
requirements for the degree of
Master of Science

in

The Department of Physics and Astronomy

by
John Wesley Chapman, Jr.
B.S., Louisiana State University, 2008
May 2012

ACKNOWLEDGMENTS

In order to complete this study, a substantial amount of background theory beyond the traditional Medical Physics curriculum was necessary. I am grateful to Dr. Kenneth Hogstrom for providing additional instruction in these areas and recognize that I am fortunate to have learned this material from a prominent expert in this field. I also owe a large debt of gratitude to my very patient and dedicated advisor, Dr. Jonas Fontenot. His expert guidance has been very helpful in improving my technical writing, research and presentation skills, data analysis, and problem solving. I would also like to thank Dr. Fontenot for his guidance in issues outside of academics and for his understanding during difficult times. I greatly appreciate the time that my advisory committee (Drs. Jonas Fontenot, Kenneth Hogstrom, Wayne Newhauser, and Jeffrey Blackmon) devoted towards my project. I have benefitted from their wisdom and experience in the field, constructive criticism and helpful comments, and willingness to provide direction. In addition, I am grateful to the late Dr. George Ciangaru for devoting time to corresponding with me and for his recommendations concerning Moliere scatter theory. Further, I thank Dr. Bernard Gottschalk (Harvard University) for the FORTRAN code that he provided freely on his website (http://physics.harvard.edu/~gottschalk) and for his assistance in compiling the code.

I am thankful to my fellow students, Mary Bird Perkins Cancer Center (MBPCC) faculty, and post-doctoral fellows for their readiness to discuss my research project and their helpful insights. I especially thank Mr. David Perrin for helping me develop a preliminary electron dose calculation algorithm. I also am grateful to Mr. Gordon Mancuso for providing his distance-to-agreement MATLAB routine, which served as the framework for the distance-to-agreement routine written for this project. The daily research discussions that I shared with Dr. Robert Carver and Mr. James Kavanaugh have also been helpful, and I feel that we all have advanced our own understanding of our projects by discussing them. I also would like to thank Mr.

Michael Thomas, software engineer at MBPCC, for his hard work and quick turnaround time on converting the pencil beam code from MATLAB to the C language.

I am grateful for the Medical Physics instruction that has served as a solid basis for my thesis work. I owe much gratitude to Drs. Jonas Fontenot, Kenneth Hogstrom, John Gibbons, Polad Shikhaliev, Kip Matthews, Erno Sajo, Brent Parker, Michael Price and all of those that have provided clinical instruction at MBPCC. The administrative staffs, both at Louisiana State University (LSU) and MBPCC, also deserve recognition for their hard work.

I acknowledge my entire family for their encouragement and support. I owe a great debt of gratitude to my parents, who have shown me that no matter what one's experience has been, a new destiny can be achieved through proper initiative and dedication. I believe that my parent's love, support, and openness to my decisions made have been integral to forming the person that I currently am and has helped greatly in all of my endeavors, including the current project. I am grateful to both my parents and siblings for their willingness to listen to my research progress and feign interest. More importantly, I am grateful to them for becoming my biggest fans, even though I still have not properly explained to them exactly what it is that I do.

I thank both my wife, Rebecca, and her family, for their love, encouragement and unconditional support. The support that they have provided to both my family and me will never be forgotten. I am grateful to Rebecca for being patient with the career options that I have explored and for her generosity and support. She was a constant source of inspiration to me throughout this project, finding unique ways to make me laugh in any given situation. Rebecca has helped me to remain positive and focused.

I thank LSU and MBPCC for providing resources that supported this project. Furthermore, I acknowledge LSU for providing the computational resources that were necessary

to complete this project; portions of this research were conducted with high performance computational resources provided by LSU (http://www.hpc.lsu.edu).

This research was supported by contract W81XWH-10-1-0005 awarded by The U.S. Army Research Acquisition Activity, 820 Chandler Street, Fort Detrick, MD 21702-5014. This report does not necessarily reflect the position or policy of the Government, and no official endorsement should be inferred.

TABLE OF CONTENTS

LIST OF TABLES

LIST OF FIGURES

ABSTRACT

In this study, a proton pencil beam dose calculation algorithm was developed for a parallel, monoenergetic beam incident on a homogeneous water phantom. Fermi-Eyges theory (Eyges 1948) was used to transport pencil beams, and the characteristic width of elastic scatter events was modeled using the differential Moliere scattering power (Gottschalk 2010). The incorporation of this scattering power formalism allowed our model to account for multiple Coulomb scattering, single scattering, plural scattering, and rigorously accounted for material effects on scatter. Nonelastic nuclear interactions were incorporated into an additional pencil beam model. The attenuation of primary fluence due to nuclear events was accounted for using a weighted sum of primary and nuclear pencil beam components (Pedroni *et al.* 2005, Soukup *et al.* 2005). Free parameters of the nuclear pencil beam model were determined by a non-linear least squares fit to narrow field Monte Carlo data. Our dose calculation model was commissioned using central-axis depth dose data extracted from Monte Carlo simulations. Analytical corrections were incorporated to ensure that all input central-axis data satisfied side scatter equilibrium.

The dose calculation model was evaluated against Monte Carlo simulations of dose in a simplified beamline. Proton beam energies of 50, 100, 150, 200, and 250 MeV and field sizes of 4x4 cm^2 and 10x10 cm^2 were evaluated in three geometries: (1) flat phantom; (2) step phantoms (step heights of 1 and 4 cm); and (3) oblique phantom (rotation angle of 45°). All geometries evaluated with Monte Carlo dose calculations yielded 100% of points passing *distance-to-agreement* (*DTA*) $\leq$ *1 mm* or *Percent Dose Difference* $\leq$ *3%*. At least 99% of points passed with a *DTA* $\leq$ *1 mm* or *Percent Dose Difference* $\leq$ *2%*. The pencil beam dose calculation model provided excellent results when compared with Monte Carlo data.

CHAPTER 1. INTRODUCTION

1.1 Background and Significance

1.1.1 Fundamental Advantages of Proton Therapy

Current clinical standards for use of external beam radiation in cancer treatment include photon and electron therapy. The success of these methods is due, in part, to reliable technology that is easy to operate and useful in treating a wide variety of diseases. However, the exponential attenuation of photon beams results in excess dose delivered to healthy tissue proximal and distal to the treatment site (see Figure 1.1). Electron dose falloff results in minimal dose distal to the treatment site, but excessive multiple Coulomb scatter limit the applications of electrons to sites within 6 cm of the surface (Hogstrom 2003).

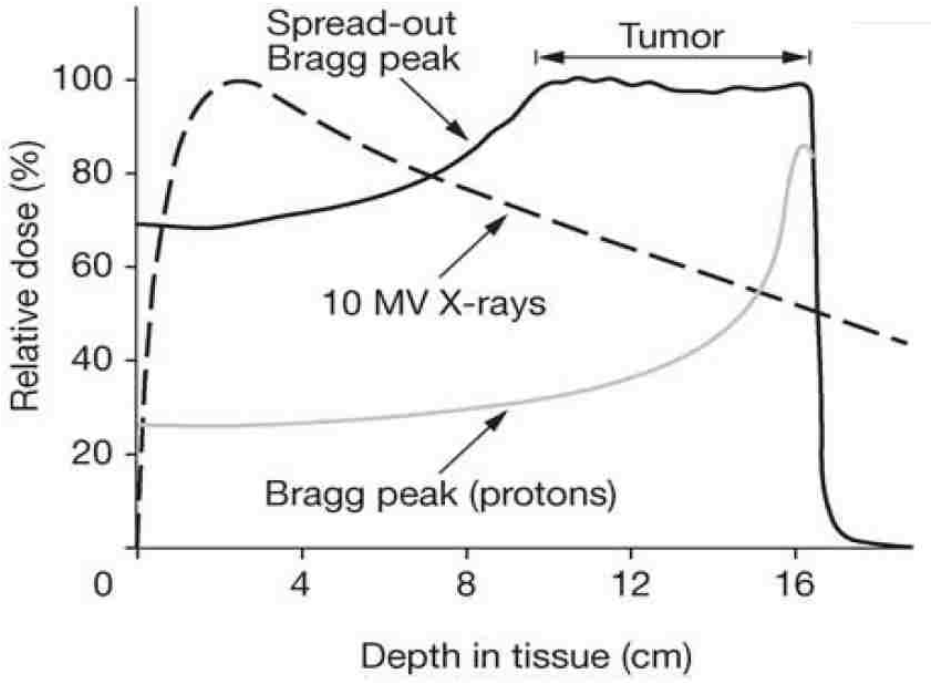

Figure 1.1: Central-axis depth dose comparisons of a pristine (grey) and spread-out proton beam (solid black curve) to 10 MV x-rays (dashed black curve) (Koehler and Preston 1972). Note the sharp distal dose falloff of the Bragg peak, and the insignificant dose beyond the proton range.

Protons offer significant benefits in radiation therapy because they travel in nearly straight lines (small amount of multiple Coulomb scatter), they have a narrow Bragg peak that

can be modulated to create peaks of arbitrary widths, and there is clinically insignificant dose beyond treatment sites (Wilson 1946). These properties have led to the hypothesis that protons can provide increased local control of tumors while sparing normal tissue (Koehler and Preston 1972). As seen in Figure 1.1, a single field proton beam can achieve high, uniform doses with significant proximal (for a spread-out Bragg peak), but no excess distal dose, compared with a single field photon beam, which gives a non-uniform distribution over the tumor with both significant proximal and distal dose.

The potential clinical benefits of protons proposed by Wilson (1946) encouraged the first clinical evaluations (Tobias *et al.* 1958). Several studies produced results that confirmed the dose localization and normal tissue sparing advantages offered by protons over photons (Terasawa *et al.* 2009). However, many of these studies were performed in research institutions with limited treatment options and were completed when proton therapy was in its infancy; thus, the results from these studies might represent a minimum on the potential advantages of protons over photons. The positive results obtained in these early studies garnered further interest in the field of proton therapy and in 1990, one of the earliest hospital-based proton treatment centers opened at Loma Linda University Medical Center in California (Slater *et al.* 1991). Currently, there are 37 proton treatment facilities in operation around the world (PTCOG 2012) with 22 more planned over the next three years.

1.1.2 Beam Broadening

The spread-out Bragg peak shown for the proton beam in Figure 1.1 depicts a clinical, modulated proton beam. The narrow "pristine" peaks that are characteristic of monoenergetic proton beams (Figure 1.1) are too narrow to treat most tumors uniformly so they must be spread out in depth and width. There are two techniques for producing adequate clinical beams: passive scattering and active scanning. Most proton treatment facilities currently use passive scattering

techniques. The passive scattering method typically uses a double scattering foil system. The first foil in these designs is typically made of a high-Z material that spreads the beam laterally. This results in a forward-peaked beam whose lateral distribution is approximately Gaussian in shape. The second foil used in these systems is typically a contoured scatterer made of high-Z and low-Z components; the high-Z component is used to scatter the central part of the beam to the periphery and the low-Z component is used to modulate the energy of protons while minimizing scatter. The combination of the two scattering foils produces a laterally broad, uniform field.

To spread the beam in depth using the passive scattering technique, a range modulator wheel (RMW) is typically used. The RMW rotates various thicknesses of material into the beam as a function of time, producing beams with modified ranges and intensities. After several such modified beams have been directed into the patient, the cumulative result is the spread-out Bragg peak (SOBP, see Figure 1.2). Collimators are used in passive scattering systems to define the lateral extents of the treatment field. Finally, the dose falloff of the proton beam (range) is modulated laterally using a range compensator, so as to conform to the distal edge of the planning target volume (PTV). The range compensator is made of tissue-equivalent material (usually polymethyl methacrylate (PMMA)), and its thickness controls how much the SOBP shifts towards the patient surface. Figure 1.3(a) shows a typical passive scattering system.

As an alternative to passive scattering techniques, the active scanning method has been used in only a few clinics (Pedroni *et al.* 1995). In this form of beam broadening, individual small beam spots are controlled under magnetic deflection (along two axes) with the ability to modulate the energy and fluence of each spot. The typical method of active scanning is to first deliver dose to the spots at the distal edge of the PTV then proceed with scanning proximal spots until the entire volume has been treated by varying intensity and energy for each spot. A typical

active scanning system, illustrated in Figure 1.3(b), does not require a range modulator, dual scattering foil system, collimator, or range compensator as does the passive scattering system.

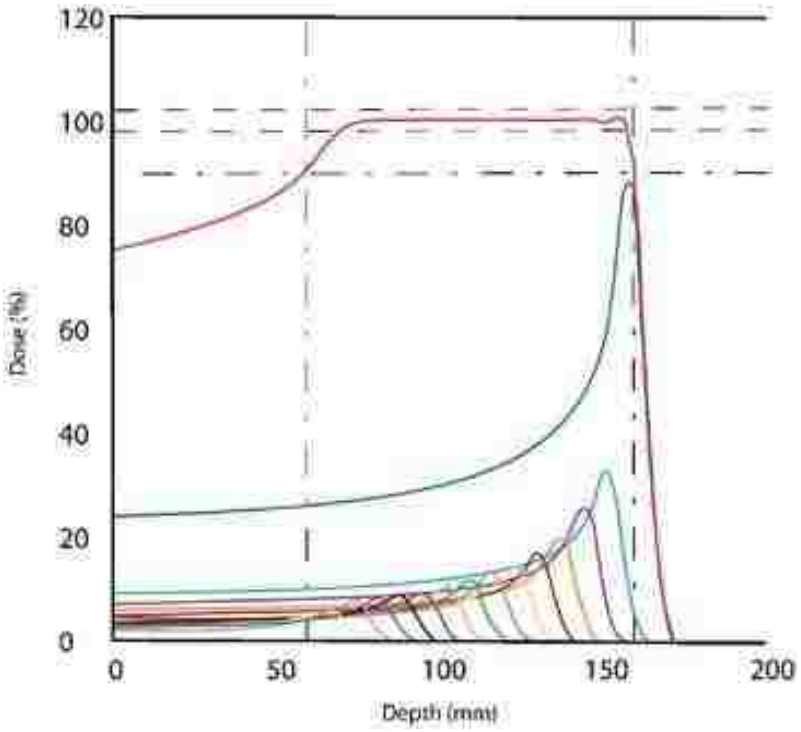

Figure 1.2: Multiple narrow Bragg peaks of proton beams of differing fluence and energy can be optimally superimposed to form a spread-out Bragg peak (SOBP). The solution above produced a flat SOBP of 10 cm that penetrates (90% depth) approximately 16 cm in water (Khan 2010).

1.1.3 Basic Proton Interactions

Protons undergo various physical interactions with atomic electrons and nuclei in a calculation medium. Most of these interactions will be discussed in this section, but those interactions that are relevant to clinical dose calculations will be highlighted.

As protons penetrate through a medium, they lose energy at the expense of excitation and ionization of electrons in the target atoms. At therapeutic energies, radiation loss is negligible, so the energy loss per path length (stopping power) is given by

$$S = \left(\frac{4\pi e^4 NZ}{m\beta^2 c^2}\right)\left\{\ln\left[\frac{2mc^2\beta^2}{I(1-\beta^2)}\right] - \beta^2 - \sum_j \frac{C_j}{Z}\right\} \ (MeV\ cm^{-1}), \qquad (1)$$

where e is the charge of the incident proton, β is the speed of the proton (in units of c – the speed of light in vacuum), m is the electron mass, Z is the mean nuclear charge, N is the mean density, I is the mean excitation energy of the target atoms, and C_j/Z is a shell correction that is only important at low proton velocities (ICRU 1998). Stopping power is typically more useful when divided by the material density; when in this form, it is referred to as mass stopping power.

(a)

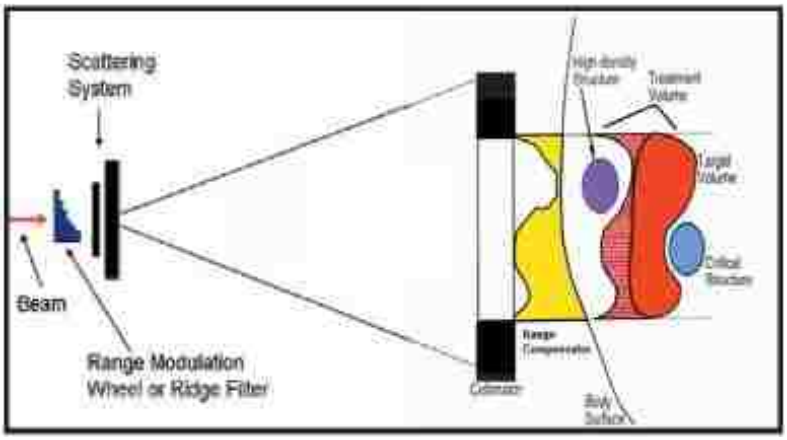

(b)

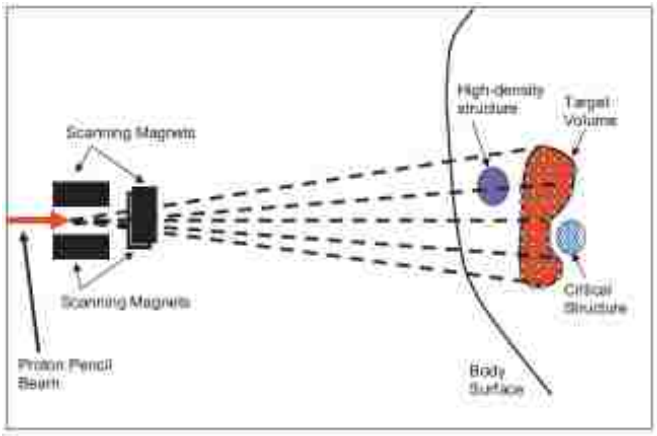

Figure 1.3: Beam broadening systems including (a) a passive scattering system, and (b) an active scanning system (Chu *et al*. 1993).

Stopping power (and therefore, mass stopping power) exhibits a *1/E* dependence (Figure 1.4), and this energy dependence is the main factor that causes the formation of a Bragg peak. Statistical fluctuations due to the discrete energy loss events (energy straggling) cause monoenergetic protons to stop at different depths (Bohr 1948). This effect, called range

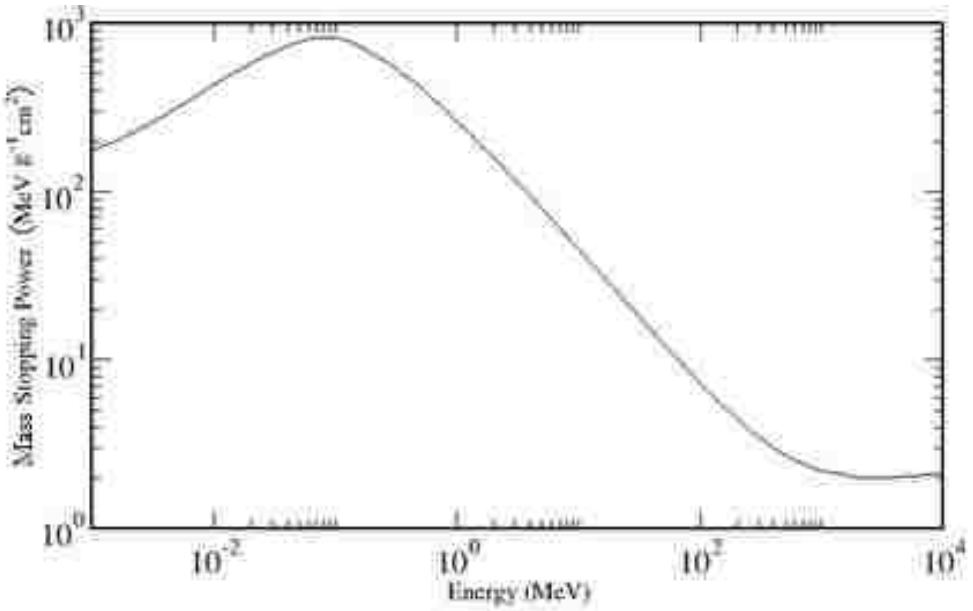

Figure 1.4: Mass stopping power of protons in liquid water (from Berger *et al.* 2005).

straggling, causes the narrow Bragg peak predicted by stopping theory to have increased width – even for initially monoenergetic beams (Gottschalk 2004). Another effect that protons experience as they lose energy in a target material is scattering. Because of the large mass of protons relative to electrons, the deflections that protons experience in electromagnetic interactions with electrons are negligible. As protons interact with atomic nuclei, the Coulombic force tends to deflect protons away. Single deflections with atomic nuclei still tend to be small, but as protons proceed through the medium, the cumulative effect of very many of these small events becomes significant. The accumulated deflections are often given a statistical treatment, and because there are numerous small deflections, the central limit theorem is invoked; thus, the probability density describing these *multiple Coulomb scatter* (MCS) deflection angles is modeled by a Gaussian.

In order to build an accurate model of MCS, an accurate account of *single scatter* events with the atomic nuclei must first be determined (Gottschalk 2004). The probability of single scatter events is described by the Rutherford formula, which has χ^{-4} dependence, where χ refers

to the single scattering angle. Figure 1.5 shows the comparison between a Gaussian ($e^{-\chi^2}$) and the Rutherford dependence (χ^{-4}). The Rutherford dependence falls off much more slowly than a Gaussian does. However, it is also clear that at large angles the Gaussian predicts that multiple scattering is less than single scattering (Gottschalk 2004), which cannot be true and is a limitation of the Gaussian approximation of MCS. Therefore, the true scatter distribution should approach χ^{-4} at large angles and remain Gaussian for small angles. Moliere scatter theory (c.f. Bethe 1953) includes MCS and single scattering, as well as a correction term to account for an intermediate number of scatters (called plural scattering). Moliere theory is considered to be the definitive scatter theory, and it has been shown to agree well with measurements (Gottschalk *et al.* 1993).

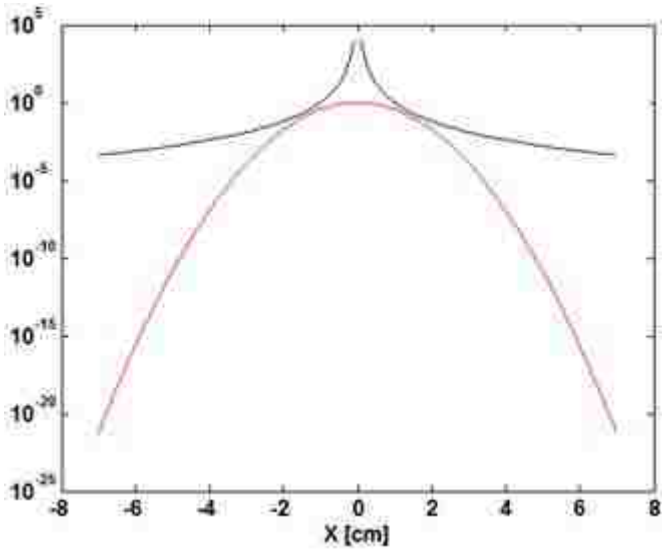

Figure 1.5: Comparison of Gaussian (red) and single scatter dependence (black).

Protons undergo nuclear interactions at a rate of about 1.2% $g^{-1}cm^2$ (Gottschalk 2004). There are three types of nuclear reactions recognized by ICRU report 63 (ICRU 2000): (1) elastic, (2) inelastic, and (3) nonelastic. Elastic interactions with atomic nuclei have already been discussed (MCS, single, plural scattering) and inelastic interactions are a special case of nonelastic interactions. Thus, nonelastic nuclear interactions will be the focus in this section.

This type of interaction is nonelastic in the sense that total kinetic energy is not conserved because various secondary particles are created that carry energy away from the original nucleus (Table 1.1). The secondary particles created in nonelastic nuclear interactions include short-range charged secondary particles (which acquire about 60% of the incident proton energy) and long-range neutral particles (which acquire about 40% of the incident proton energy) (Gottschalk 2004). The portion of incident proton energy carried off by neutral particles is essentially lost (*i.e.,* deposited far away from the interaction point) (Gottschalk 2004). This 'lost energy' phenomenon caused by the neutral products effectively removes energy from the Bragg peak (Gottschalk 2004). Some of this lost energy gets redistributed in the target and some exits the target completely (Gottschalk 2004). However, these neutral particles (including neutrons and photons) do not necessarily have a negligible effect on patient dose; the high relative biological effectiveness (RBE) of neutrons and the dose imparted by photons may add a background component of dose to the patient. Figure 1.6 shows the redistribution of the Bragg peak due to the neutral particles carrying away some of the incident proton energy. The short-range particles that are created in nonelastic nuclear events carry much lower energies than the incident proton, and they scatter out into a faint halo of secondary dose that surrounds the primary proton (Pedroni *et al.* 2005). For this reason, the secondary dose effect is often called the "nuclear halo" (Pedroni *et al.* 2005, Soukup *et al.* 2005).

1.1.4 Dose Calculation Methods

In order for a linear accelerator to be effectively utilized, an interface between the accelerator hardware and the patient data must exist. In clinics, this interface is referred to as a treatment planning system (TPS). A TPS is a sophisticated computer software package that is used to evaluate dose delivered to a planning target volume (PTV) and normal tissues for one or more treatment setups. By comparing the dose delivery for multiple treatment setups, a TPS

allows the end user to decide which setup is most appropriate for the patient anatomy and disease. Most TPSs include the ability to import patient data (such as computerized tomography (CT) scans), select the beam arrangement around the patient, calculate dose, provide dose optimization algorithms to allow intensity modulation, allow one to set prescription dose as well as parameters relevant to intensity modulation treatments (*e.g.*, uniformity of dose over tumor, dose constraints on healthy tissue and organs at risk), and to view and analyze results. Figure 1.7 shows a breakdown of the role of a TPS in implementing a new machine into a treatment clinic.

Table 1.1: Secondary particles formed in nonelastic nuclear interactions. The mean fraction of energy carried away by each particle is indicated for an incident proton energy of 150 MeV (Seltzer 1993). Presumably, the remaining 16.5% of energy not accounted for is carried away by photons (Gottschalk 2004).

Type	**Fraction of Initial Energy Carried by Secondary Particle**
Proton	0.57
Deuteron	0.016
Triton	0.002
^3He	0.002
Alpha Particle	0.029
Nucleus (recoil)	0.016
Neutron	0.20

The dose calculation model in a TPS must balance accuracy and computational speed. Dose calculation speed is critical for a clinical TPS because patient throughput can often become an issue. However, the dose model must be sufficiently accurate to estimate the dose received by patients in radiation treatments. As the field of radiation therapy advances and new technology is introduced, there will be an increasing demand for accuracy and speed in dose calculation models.

Dose calculations involving little or no anatomical heterogeneities (*e.g.*, uveal melanoma) have been accurately modeled using broad beam (ray-tracing) methods. In a broad beam dose calculation, pre-calculated (or measured) dose distributions are scaled by the water equivalent

depth along the ray; because only heterogeneities encountered by the ray are considered, this scaling relationship is one-dimensional. Broad beam dose calculations also execute in a very short amount of time relative to other methods because of this simplistic scaling technique. Koch *et al.* (2008) described a very accurate and very fast broad beam proton dose calculation model used to treat uveal melanoma.

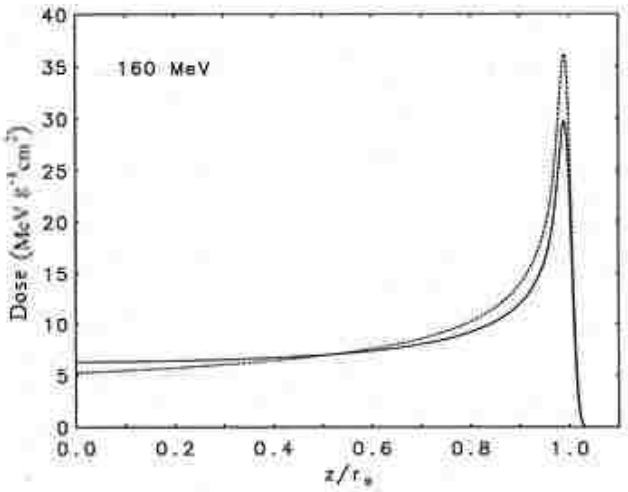

Figure 1.6: Monte Carlo calculations of the Bragg peak with nuclear reactions turned off (dashed) and the actual Bragg peak (solid) (Berger 1993). The *x*-axis displays depth normalized by the proton range for a 160 MeV beam ($r_o \approx 17.7$ cm in water).

For dose calculations requiring high accuracy for heterogeneous (patient-like) mediums, Monte Carlo (MC) simulations are currently accepted to be the gold standard. MC may have achieved this status because they simulate detailed interactions for numerous particle types and secondary particles, and the randomness of radiation is explicitly accounted for. However, because MC simulations often involve keeping a detailed history of the physical interactions of particles and secondary particles, this method requires long simulation times and expansive computer processing capabilities. The most time consuming MC methods are the original detailed history methods. With detailed history MC simulations, the energy, direction, and position of a particle are simulated after each collision (Berger 1963). Random sampling of

single scattering probabilities is used to define subsequent collisions and the collection of the saved parameters from all collisions defines the trajectory of the particle (Berger 1963).

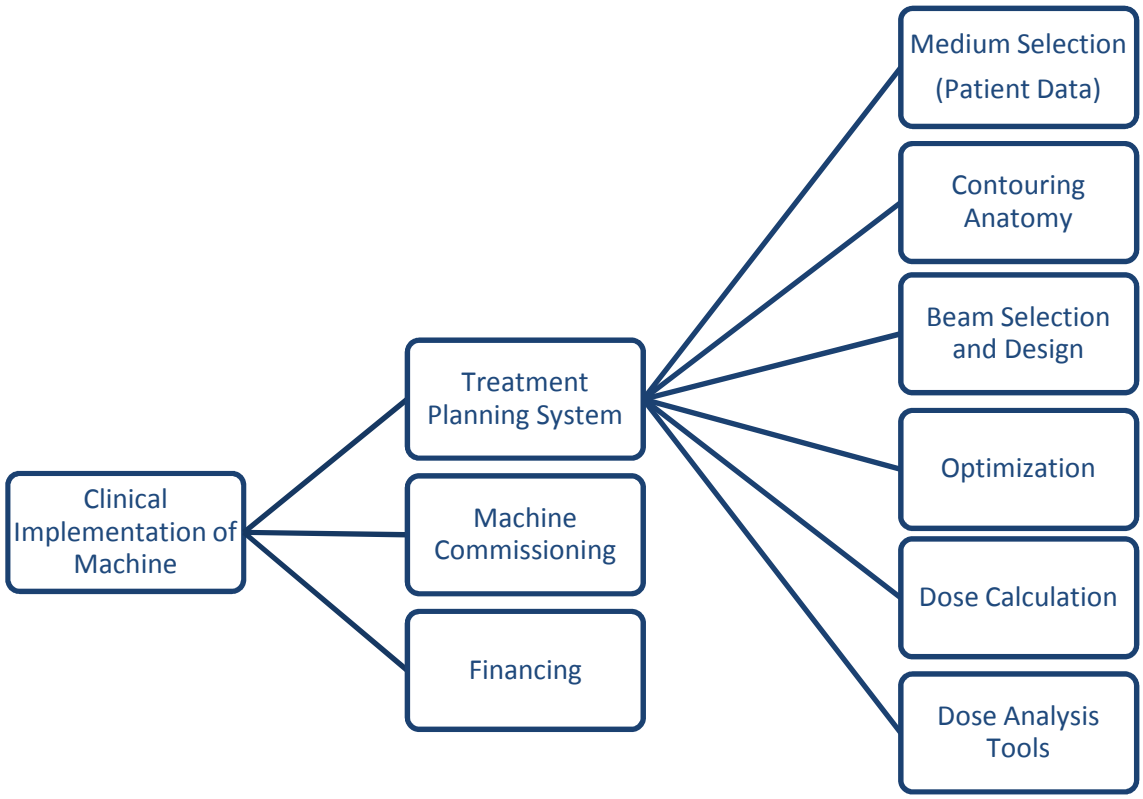

Figure 1.7: The role of a treatment planning system (TPS) in a clinic.

Detailed history MC simulations have been largely replaced by condensed history MC codes (*e.g.,* Monte Carlo N-Particle eXtended (MCNPX)), which were designed to address the significant speed limitation imposed by detailed history MC. Condensed history MC codes sample particle trajectories over a series of step lengths (along the pathlength of the particle); the exact selection of the step lengths is determined by scatter theory (Berger 1963) and step lengths must be chosen such that a random walk is formed (Berger 1963). The random walk effectively accounts for the collective effects of several collisions; this approximation is the factor that allows condensed history MC codes to reduce simulation times relative to detailed history MC simulations. These methods have comparable accuracy to detailed history methods and decreased computation time, but they are still considered too slow for clinical dose calculations.

Track-repeating algorithms are another viable option for MC simulations, and they offer further improvement in computational speed. One such algorithm by Yepes *et al.* (2008) showed that the dose calculation time for their track-repeating algorithm was improved by two orders of magnitude over a condensed history MC code. Track-repeating MC algorithms use proton trajectories that are pre-simulated in water (including path length, angles, energy loss, energy deposited, and stopping power information for each step) and these trajectories are scaled to other materials, typically by a stopping power ratio of the medium of interest to water (Yepes *et al.* 2008). Because the proton trajectories are pre-simulated, the calculation speed of track-repeating algorithms is fast; however, a large number of trajectories are needed, and these methods are most useful when implemented in a graphical processing unit (GPU) environment (Yepes *et al.* 2010). GPU simulations require sophisticated programming expertise and expansive computer resources. For these reasons, track-repeating algorithms are currently not used in the clinical environment.

There are presently no MC codes that achieve the simulation speed required for clinical dose calculations. Furthermore, commissioning a beam requires exact and often tedious modeling of multiple beamline components which could be time-consuming and difficult. As such, MC simulations are presently considered to be too time-intensive for routine clinical treatment planning. However, MC methods are still used to develop and test analytical dose models used for routine patient treatments (Newhauser *et al.* 2007b, Koch *et al.* 2005).

As an alternative to MC and broad beam techniques, appropriate analytical solutions can achieve the necessary balance of accuracy and speed for proton dose calculations (Table 1.2). One such solution is referred to as a pencil beam algorithm (PBA). In a typical PBA, a broad beam is divided into a grid of smaller pixels. Each of these beam segments, called pencil beams, are then individually transported through the target material and the resulting dose distributions

from each pencil beam are then summed to produce the total dose. PBAs are discussed in greater detail in the Chapter 2.

Table 1.2: Descriptions of analytical and Monte Carlo methods used for proton dose calculations, along with indications of calculation speed and accuracy.

ANALYTICAL METHODS			
Method	**Ray-Tracing**	**Pencil Beam**	
Description	Water equivalent depth along one dimension is used to extract pre-determined dose in water.	Divides broad beam into discrete pixels. Dose from each pencil beam is calculated and summed to produce the broad beam dose.	
Calculation Speed	Very Fast	Fast	
Accuracy	Accurate (except for heterogeneities)	Very Accurate	
MONTE CARLO METHODS			
Method	**Detailed History (Type I)**	**Condensed History (Type II)**	**Track-Repeating**
Description	Simulates collisions of each particle one-by-one. All secondary particle collisions are simulated one-by-one as well.	Effect of many small collisions condensed into a single, large effect using a probability density derived from scatter theory.	Uses pre-simulated proton trajectories in water and scales them to other materials. This greatly reduces the number of collisions that are modeled in MC.
Calculation Speed	Very Slow	Slow	Fast
Accuracy	Very Accurate	Very Accurate	Very Accurate

1.1.5 Application of Pencil Beam Theory to Protons

It is generally desirable for a PBA to use some form of measured data and manipulate that data according to the physics involved. A dose calculation model typically increases in accuracy in accordance with the amount of physical phenomena modeled in the PBA. Therefore, a PBA for protons would be most useful if a rigorous account of all the basic physical interactions discussed in section 1.1.3 were included in the dose calculation model. In this

discussion, several scattering theories will be referenced; more details on these theories can be found in Appendix D.

The earliest dose calculation models for protons implemented one-dimensional broad beam (ray-tracing) algorithms (see Table 1.2), which did not account for scatter and modeled only energy losses using measured dose data in water. Experiments performed by Urie *et al*. (1986a) demonstrated that MCS from inhomogeneities reduced the Bragg peak dose significantly, compared with ray-tracing calculations, which would shift the unmodified Bragg peak measured in water to a different position in depth. This data indicates that ray-tracing techniques are only suitable for simple inhomogeneities. To accurately account for more complex inhomogeneous regions, MCS effects must be included in PBAs (Urie *et al.*1986a).

A proton dose calculation paper by Petti (1991) included both a ray-tracing algorithm and a differential pencil beam (DPB) model that included MCS effects. The results from both algorithms were compared, using a custom MC dose calculation method as the baseline data, to determine the additional accuracy achievable by incorporating MCS effects. MCS was incorporated into the MC dose model, and pencil beams were determined from a MC dose distribution in water rather than explicitly using scatter theory to incorporate MCS effects into the pencil beams. Material dependence was accounted for by using the cumulative electron density relative to water.

By incorporating MCS effects into the DPB model, Petti (1991) showed increased accuracy in: the shape of the lateral penumbra, location and magnitude of hot spots, estimates of the dose at a given point, and estimates of the uncertainty in the dose at a point due to patient motion over ray-tracing techniques. The hot spots predicted by the DPB model occurred in generally the same locations as the MC model with magnitudes 2-3% lower than what was predicted by the MC model. The ray-tracing model did not predict hot spots. However, the dose

predicted by both the DPB and ray-tracing algorithm downstream from the inhomogeneity did not change as the inhomogeneity depth was altered, whereas the MC dose values changed by 40% over the range of depths tested. The DPB was subject to this limitation because only an integrated electron density was used in determining the dose. Thus, for points proximal and distal to the inhomogeneity, the integration gave the same cumulative electron density regardless of the depth of the inhomogeneity; thus, hot and cold spots of dose caused by inhomogeneities were not appropriately altered with the inhomogeneity depth.

Studies by Urie *et al.* (1986b) and Sisterson *et al.* (1989) showed that in addition to the degradation of the Bragg peak due to inhomogeneities, beam-modifying devices upstream of the patient can affect the lateral penumbra and the dose falloff beyond the proton range. Hong *et al.* (1996) developed a PBA to account for these effects using a passive scattering system. For beam elements upstream of the patient, the characteristic scattering angle was calculated using the Highland (1975) equation and the lateral projection of this scattering angle was taken as increases in source size or the radial spread at the point of interest, depending on the location of the beam element relative to the collimator. The total root mean square (RMS) width (sigma) of the pencil beam was then taken to be the sum in quadrature of the source size projected by the collimator to the depth of interest, the sigma due to elements downstream of the collimator, and the patient sigma.

The patient sigma was calculated from a lookup table pre-calculated by thick target Highland theory at the depth equal to the radiologic path length through the patient. Radiologic path length was determined by an integral over the water equivalent density determined in the patient. Hence, the Hong *et al.* (1996) PBA neglected the location of an inhomogeneity in calculating MCS effects, as did the Petti (1991) DPB model. However, some improvements offered by this model included the use of measured central-axis depth dose profiles, which

inherently incorporated range straggling effects, and MCS was explicitly modeled using a Gaussian with a sigma given by contributions from the source, beam elements, and the patient.

The Hong *et al.* (1996) PBA was shown to predict 20%-80% penumbra widths within 1 mm of measurements for air gaps over the range of 5 cm to 20 cm. Inhomogeneities were tested by using a water phantom with half of the beam covered by a Lucite block 5 cm thick and a 5.3 cm gap between the Lucite block and the water tank. MCS effects due to the Lucite block were appropriately modeled, as the hot and cold spots determined by the PBA had the same general shape; however, the magnitude of the hot spot on the unblocked side were underestimated by the PBA; Hong *et al.* (1996) attributed this to neglecting nonelastic nuclear interactions created in the Lucite block, which causes secondary protons to scatter out into the unblocked side of the water tank. This effect was lowered with increasing depths due to the short ranges of secondary protons.

In a paper by Russell *et al.* (1995), a method was described which incorporated both MCS and large-angle single scattering effects. MCS effects were accounted for using Fermi-Eyges theory (Eyges 1948) with scattering powers related to the Hanson *et al.* (1951) approximation of Moliere theory (c.f. Bethe 1953). To include large-angle scattering effects, the water equivalent surface energy required to give the same shape of the Moliere distribution in water was found. The water equivalent surface energy was used to interpolate previously stored Moliere distributions and the *1/e* width of this distribution was rescaled to the RMS value found using Fermi-Eyges theory. All results showed excellent agreement between experiment and calculation of radial spreads in water. Because Fermi-Eyges theory was used and because the energy scaling technique relied on a depth-dependent calculation, the Russell *et al.* (1995) algorithm accounted for the scattering effects due to the location on an inhomogeneity. However, results were not shown for inhomogeneous phantoms.

Another interesting topic introduced in the Russell *et al.* (1995) paper was range straggling correction. While this inclusion of this correction reproduced the experimentally determined depth dose falloff near the proton range in water, its derivation was based on lateral scattering effects. It has since been demonstrated that this approach is invalid and that range straggling is instead due to energy straggling (Berger 1993, c.f. Deasy 1998). Hence, the best approach for including range straggling in a PBA is by incorporating measured central-axis data which already account for this effect (Deasy 1998). In a later publication, Russell *et al.* (2000) developed a PBA that used measured central-axis data to account for range straggling caused by energy straggling. However, the range straggling correction in Russell *et al.* (1995) was included in this publication as well. In addition, the Russell *et al.* (2000) model did not include the single scattering correction provided in Russell *et al.* (1995). In the same manner as Hong *et al.* (1996), the Russell *et al.* (2000) model accounted for the initial beam phase space. The 20%-80% penumbra width predicted by the Russell *et al.* (2000) PBA at 10 cm depth, over a range of air gaps from 0 to 16 cm were within 1 mm of measured data. The prediction of hot and cold spots due to inhomogeneites and lateral dose falloff results were comparable with other PBAs previously mentioned.

Deasy (1998) introduced a PBA based on Hanson's approximation of Moliere theory to include large-angle single scattering effects. This formalism was implemented by forcing all the material dependent parameters in Moliere theory (*e.g.*, atomic number, atomic mass, material density, fraction by weight of elements) to be functions of depth, which Deasy (1998) stated was valid since Moliere made no assumptions about the composition of the dose calculation medium. With these depth-dependent material parameters included, this model rigorously accounted for material dependence; this feature was novel because it represented a significant improvement over prior algorithms using convolution methods (Petti 1991, Russell 1995, 2000), which simply

scaled pre-calculated doses in water to the material of interest. Thus, the explicit depth dependence of the material parameters allowed this PBA to account for the scattering effects due to the location of an inhomogeneity. To account for range straggling effects and the attenuation of the primary proton fluence by nuclear interactions, Deasy (1998) multiplied the fluence distribution given in Hanson's approximation by a MC central-axis depth dose curve measured in water. The MC data was determined in water and scaled to the correct depth using cumulative electron density. Full width at half maximum (FWHM) values near the end of the range predicted by the PBA were shown to be within 1% of predicted theoretical values for incident energies of 160 MeV and within 3% at 250 MeV (Deasy 1998). However, the results were only demonstrated in a homogeneous water phantom.

Ciangaru *et al.* (2005) extended Deasy's (1998) model for dose calculations in heterogeneous phantoms. Several mixed material phantoms were tested using this PBA, including an air-bone interface in water, bone parallelepiped in water, bone slab in water, homogeneous bone phantom, and a homogeneous water phantom. One feature highlighted in the Ciangaru *et al.* (2005) PBA was energy-dependent calculations of stopping power ratios[1]. Typically, PBAs will use energy-independent stopping power ratios to calculate the effective depth in a target material; however, Ciangaru *et al.* (2005) showed that this approximation was not valid for protons in high density materials (such as bone) at energies below 20 MeV. Therefore, assuming energy-independent stopping power ratios could affect the calculation of the clinically important Bragg peak region for phantoms containing high density heterogeneities. The Ciangaru *et al.* (2005) model was compared to several MC dose calculations, and the agreement in general was very good for inhomogeneities located in the first half of the proton

[1] Energy-dependent stopping power ratios were first investigated by Newhauser (2001) and later described in Newhauser *et al.* (2007a), as well as Zhang and Newhauser (2009).

range, but the agreement between PBA and MC results diminished for inhomogeneities located in the latter half of the proton range. For most comparisons, the 20%-80% penumbras predicted by the PBA and MC were within 1 mm with the PBA predicting the smaller value, but for some comparisons, this discrepancy rose to as high as 2.5 mm. The worst results were seen for lateral profiles taken through the center of a bone slab placed at the Bragg peak. As in most PBAs, the distant lateral dose falloff tails for the PBA were smaller compared with the MC results; Ciangaru *et al.* (2005) attributed this effect to the Gaussian approximation introduced by using Hanson's approximation of Moliere theory. However, Moliere theory was included into the Deasy (1998) and Ciangaru *et al.* (2005) models to account for these large-angle tails. Thus, it is not clear that this model is appropriate for inhomogeneous phantoms.

Two different analytical algorithms were introduced by Schaffner *et al.* (1999) for active scanning proton dose calculations. One of these algorithms, a ray-casting model, included a formalism for modeling range straggling, which was empirically characterized by fits to probability distributions modeled using scatter theory over a span of depths and incident energies (Schaffner *et al.* 1999). The ray-casting model inherently accounted for proton energy loss since it was based on pre-measured spot beam data in water, and the modeling of the degradation of the Bragg peak was also improved because of the inclusion of a range straggling model. However, this model was very limited as it did not account for MCS.

Another algorithm proposed by Schaffner *et al.* (1999) was a pencil beam model that was designed as a dose kernel convolution. In this model, dose and fluence calculations were performed separately; hence, the name of this method was the fluence-dose calculation. The beam fluence inherently modeled the spread of the beam due to phase space and air gap contributions, and the spread of the beam due to scatter in the patient was estimated using a dose kernel. The dose kernel itself was determined using analytical functions that were fitted to MC

calculated depth dose curves (Schaffner 2007). Because depth dose curves were obtained for both primary and secondary protons, the transverse kernel distribution was determined by a two-Gaussian fit to the primary proton MCS and large-angle scatter events (one Gaussian for each). Once the dose kernel was modeled analytically, it was scaled to the water equivalent range (WER) to account for material effects; however, because the WER is an integral quantity, this model was not capable of accounting for scatter effects due to inhomogeneity location, as in the Petti (1991) model. An optimization method was also used in this model to produce SOBP doses.

Most proton PBAs prior to 2005 incorporated the attenuation of primary protons due to nuclear interactions by using measured MC central-axis depth dose data. According to Pedroni *et al.* (2005), neglecting the effects of nonelastic nuclear interactions on the pencil beam width could lead to predicted dose uncertainties of up to 10%, depending on the size of the target volume; therefore, nonelastic nuclear interactions have a non-negligible effect on the proton dose distribution (Pedroni *et al.* 2005, Soukup *et al.* 2005). These factors were the motivation for incorporating a "nuclear halo" pencil beam into the Pedroni *et al.* (2005) dose calculation model. The Pedroni *et al.* (2005) model was the first PBA to incorporate the effects of beam attenuation and the nuclear halo caused by nonelastic nuclear interactions. The model used two Gaussians to determine the fluence: one Gaussian was used to account for primary scatter (a modified version of the Highland equation was used) and the second Gaussian represented the nuclear halo. The nuclear halo parameters were experimentally determined by scanning pencil beams in concentric square frames at varying distances from a small ion chamber. The overall dose equation was taken as a weighted sum of these two Gaussians, multiplied by the measured integral dose to convert the fluence to dose. The model was highly empirical, and many values were parameterized on the basis of the treatment machine at Paul Scherrer Institute (PSI, Switzerland);

however, excellent results with measurements made on their treatment machinery were observed. SOBP depth dose curves were predicted within 1% of measurements. Comparison of dose calculations with a charge-coupled device (CCD) used to measure dose from an intensity modulated proton therapy (IMPT) treatment showed excellent agreement. Accuracy of the model was with 1% to 2% (standard deviation) of ionization chamber measurements.

The Pedroni *et al.* (2005) PBA accounted for MCS effects by using a modified version of Highland theory and transport was accomplished using Fermi-Eyges theory. However, the Highland formula was only evaluated at the surface, and a scaling relation (Overas 1960) was used to find the scattering power at deeper depths. This scaling relation depended on depth in the phantom, the proton range, and an empirically determined exponent which scaled the scattering power to the material at depth z. It is not clear that this scaling method is entirely appropriate for an inhomogeneous phantom.

Soukup *et al.* (2005) developed a PBA which was very similar in form to the Pedroni *et al.* (2005) algorithm. This PBA accounted for the nuclear halo and the beam attenuation of primary protons. Stopping power ratios for materials encountered in the phantom were performed as energy-dependent calculations. The Soukup *et al.* (2005) algorithm incorporated adaptive division of pencil beams to more accurately model heterogeneities. Scattering effects were calculated using a user-selected scattering power given by the Rossi formula (Rossi and Griesen 1941), corrected Rossi, or Highland / Lynch formula (c.f. Gottschalk *et al.* 1993). Beam transport was accomplished using Fermi-Eyges theory. For homogeneous and slab phantoms in water, the agreement between the PBA and MC was 3% and 1 mm. However for water phantoms with a bone-air interface occurring in the longitudinal center of the phantom, 49 subspots of the pencil beam were necessary to produce adequate results (*i.e.*, pencil beams in the area of the interface were each divided in 49 sub-pencil-beams). More clinically relevant

inhomogeneous phantoms, including a head and neck and prostate IMPT, did not reach the accuracy of the MC simulations. Soukup *et al.* (2005) has deferred the treatment of these inaccuracies for future publication.

1.2 Motivation for Research

From section 1.1.5, the most important effects to include in a PBA include MCS as calculated by scatter theory, the effects of nonelastic nuclear interactions on primary beam attenuation and the nuclear halo, experimentally determined central-axis depth dose data to account for energy loss and range straggling, and material- and energy- dependent calculations of energy loss. Additionally, the dose calculation model should be able to account for the location of an inhomogeneity and provide a rigorous account on the influence of materials on scatter events. Ideally, the dosimetric effects of large-angle single scattering and plural scattering should be included as well.

Using a two pencil beam model, as in Pedroni *et al.* (2005) and Soukup *et al.* (2005), Fermi-Eyges theory is well suited to account for all of these effects since both pencil beams are modeled as Gaussians. The inherent structure of Fermi-Eyges theory accounts for scatter effects due to the location of inhomogeneities. However, an accurate scattering power is needed to account for MCS, large-angle single scattering, plural scattering, and an explicit account of material properties on scatter events.

Gottschalk (2010) provided a comprehensive review of all available scattering power formulas for protons, and he introduced a new formula: the differential Moliere scattering power. By comparing all scattering power data, Gottschalk (2010) showed that the differential Moliere formula was the only method capable of producing results within 2% of measurements over a wide range of materials (including beryllium, aluminum, copper, and lead) at clinically relevant proton energies. The differential Moliere method was derived directly from a bilinear fit to

Hanson's approximation of Moliere theory in four materials and therefore includes MCS, single scattering, and plural scattering. The material-dependence in the differential Moliere method is encapsulated in a 'scattering length' term, which rigorously accounts for material parameters.

The purpose of the present work is to incorporate all of these effects into a PBA sufficient for clinical dose calculation. Fermi-Eyges theory is chosen for this purpose because it retains a high degree of flexibility in transport calculations. The differential Moliere scattering power is also implemented because it accounts for high-order scatter events and incorporates material dependence into these calculations. A two pencil beam model is designed; one pencil beam is assigned to primary events and another is used for nonelastic nuclear events. The undetermined parameters in the nonelastic nuclear model are parameterized on the basis of MC dose calculations. Finally, central-axis depth-dose data from MC simulations is incorporated to determine energy loss and range straggling effects and stopping power ratios are evaluated as material- and energy- dependent calculations.

1.3 Hypothesis and Specific Aims

The hypothesis of this work was that a pencil beam dose calculation will predict the dose imparted to a homogeneous phantom by a parallel, monoenergetic proton beam with a uniform beam fluence under a variety of conditions* within 2% dose difference or 1 mm distance-to-agreement (using a 1% dose threshold) compared with a Monte Carlo dose model subject to the same conditions.

* The hypothesis is proposed for the following conditions:

- Incident energies: 50, 100, 150, 200, 250 MeV;
- Field sizes: 4x4 cm^2, 10x10 cm^2;
- Beam angles: 0°, 45°;
- Step discontinuity heights along surface: 0, 1, 4 cm (0° only).

1.3.1 Specific Aim 1: Develop Dose Calculation Algorithm

Develop a monoenergetic, parallel beam dose calculation algorithm to calculate dose in a homogeneous phantom. The dose model will (1) consist of two pencil beams to account for primary and nonelastic nuclear events, (2) use Fermi-Eyges theory to transport pencil beams, (3) calculate scattering power using the differential Moliere formula, which includes material effects on scatter events, as well as MCS, single scatter, and plural scatter.

1.3.2 Specific Aim 2: Configure and Commission Algorithm Using Monte Carlo Simulations

Develop a Monte Carlo dose model in MCNPX to generate dose distributions that will serve as a source of commissioning data for the PBA. These simulations will be used as an analog for physical measurements. Analytical corrections to narrow field MC data will be applied to convert the data to infinitely broad beams.

1.3.3 Specific Aim 3: Evaluate Dose Calculation Accuracy of Algorithm in Homogeneous Media

Three distinct simulations (including flat phantoms, phantoms with a step discontinuity along the surface, and oblique beams) will be tested to evaluate the accuracy of the PBA dose predictions relative to the predictions of MC simulations. All geometries will be evaluated by the distance-to-agreement and percent dose difference between the MC and PBA datasets. These measures will be subsequently compared to the criteria proposed in the hypothesis ($\leq$ 1 mm distance-to-agreement or $\leq$ 2% dose difference, using a 1% dose threshold). The percentage of points passing these criteria will be used to indicate the agreement between MC and PBA results.

CHAPTER 2. METHODS

2.1 Aim 1: Develop Dose Calculation Algorithm

A pencil beam algorithm (PBA) was developed for calculating dose from a parallel, monoenergetic proton beam in a homogeneous water phantom. The algorithm was designed to account for user-defined beam angles and step irregularities on the target surface. Fermi-Eyges theory (Eyges 1948) was used to transport the proton beam, represented by two Gaussians. Elastic scatter events (including multiple Coulomb scattering (MCS), plural, and single scattering) were accounted for by using an analytical scattering power formula (Gottschalk 2010) to determine the characteristic width of the first Gaussian. The second Gaussian was included to characterize nonelastic nuclear events, and the sigma of the distribution was parameterized using a non-linear least squares fit to narrow field Monte Carlo (MC) dose data. The development of this algorithm is discussed in the sections that follow.

To facilitate the discussion of the desired model, some basic elements of pencil beam theory are presented in section 2.1.1. Since our model used pencil beam theory, all the equations in this section were inherently included in our work. However, the defining features of our model are not presented until section 2.1.2. The dose calculation model in section 2.1.2 elucidates the two-Gaussian model used for proton beam transport, along with the methods used to determine the parameters in both Gaussians.

Data required by the dose calculation model, excluding commissioning data, is specified in section 2.1.3. The implementation of the model into a computer-readable format and the incorporation of input data into the model are discussed in section 2.1.4.

2.1.1 Pencil Beam Theory

The theory described in this section gives a brief overview of basic pencil beam theory in the context of proton dose calculations for the geometry used in the present model (as shown in

Figure 2.1(b)). Dose calculations in the phantom are the focus of this section since our model did not account for any beam elements upstream of the phantom. For a full discussion on pencil beam theory, the reader is encouraged to consult other sources (Hogstrom *et al.* 1981, Petti 1991, Hong *et al.* 1996, Deasy 1998, Schaffner *et al.* 1999, Schaffner 2008, Russell *et al.* 2000, Syzmanowski *et al.* 2002, Ciangaru *et al.* 2005, Pedroni *et al.* 2005).

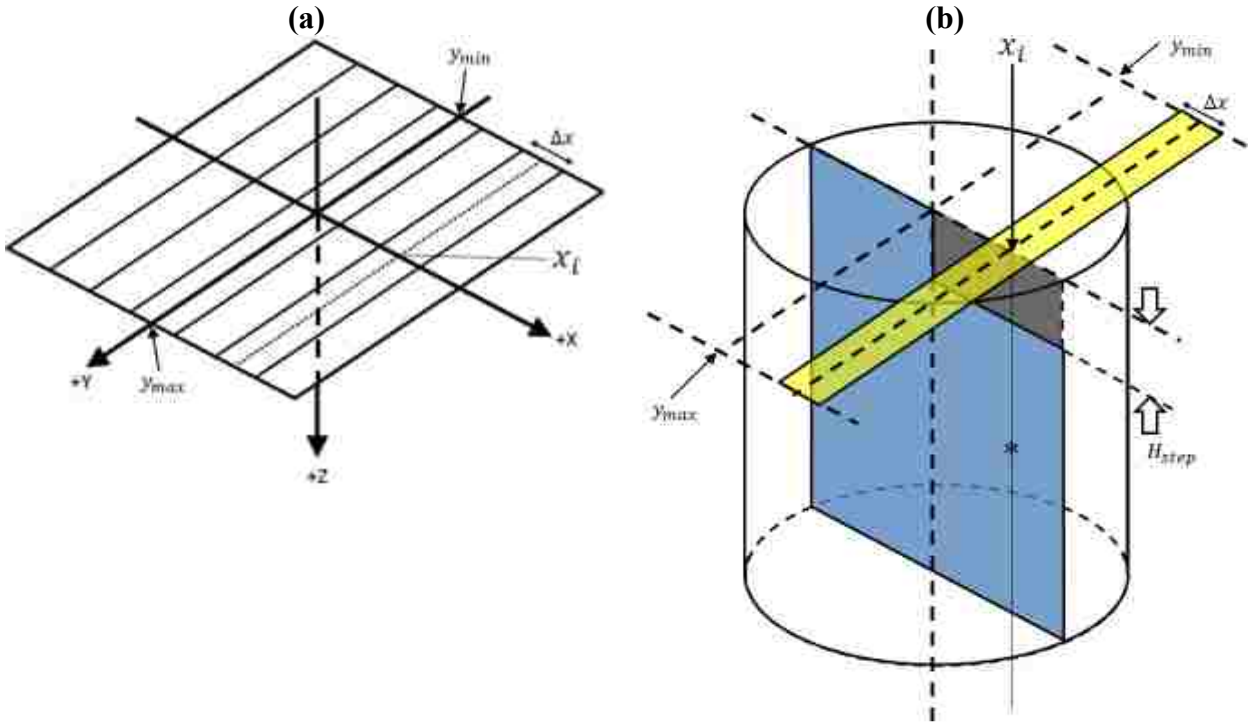

Figure 2.1: The modeling of (a) a broad beam by strip pencil beams is illustrated, along with (b) the three-dimensional geometric assumptions of our dose calculation phantom as illustrated for a step phantom (with a variable step height, H_{step}); all areas shaded in blue are water and those areas in dark grey are vacuum. In (a), a pencil beam strip of width Δx is shown centered at x_i and it extends in the y direction from y_{min} to y_{max}. The same pencil beam strip is shown in (b) (shaded in yellow), and it extends through the phantom with an arbitrary calculation point in the xz plane denoted by an asterisk (*).

The pencil beam method can be used to represent an incident broad beam as a collection of infinitesimally narrow pencil beams; hence, the total dose to an arbitrary point $P(x, y, z)$ from a broad beam is equivalent to integration over pencil beam dose contributions to $P(x, y, z)$. Following the algorithm outlined in Hogstrom *et al.* (1981), the total dose to $P(x, y, z)$ is given by the following formula:

$$D(x,y,z) = \iint_{coll(z)} S(x',y')\, d(x-x',y-y',z)\, dx'\, dy', \tag{2}$$

where $S(x',y')$ is a weighting factor for the pencil beam located at (x',y'), $d(x-x',y-y',z)$ is the dose delivered to $P(x,y,z)$ from the pencil beam located at (x',y'), and $coll(z)$ is used to indicate that the integration is performed over the collimator limits projected to depth z. The pencil beam dose can be further separated into central-axis and off-axis terms:

$$d(x,y,z) = D^{\infty}_{expt}(0,0,z) f(x,y,z), \tag{3}$$

where $x = y = 0$ is the central-axis of the beam and $D^{\infty}_{expt}(0,0,z)$ is the central-axis through experimentally determined dose, corrected to an infinitely broad field (such that side scatter equilibrium is satisfied). The off-axis term can be assumed to be related to the probability density of a point beam as given by Fermi-Eyges theory (Eyges 1948) (see Appendix D):

$$f(x,y,z) = \frac{1}{2\pi\,[\sigma(z)]^2} \exp\left\{-\frac{x^2+y^2}{2[\sigma(z)]^2}\right\}, \tag{4}$$

where $\sigma(z)$ is the root mean square (RMS) width of $f(x,y,z)$. Because Fermi-Eyges theory is used to derive $f(x,y,z)$, the small-angle approximation is valid, which allows $f(x,y,z)$ to be separable in both x and y:

$$f(x,y,z) = f_x(x,z)\, f_y(y,z) \tag{5a}$$

$$f_x(x,z) = \frac{1}{\sqrt{2\pi}\,\sigma(z)} \exp\left[-\frac{x^2}{2[\sigma(z)]^2}\right] \tag{5b}$$

$$f_y(y,z) = \frac{1}{\sqrt{2\pi}\,\sigma(z)} \exp\left[-\frac{y^2}{2[\sigma(z)]^2}\right]. \tag{5c}$$

The central-axis term only depends on the z-coordinate, so the separation of variables in equations (5a-c) allows a separation of variables for the pencil beam dose equation, given by

$$d(x,y,z) = d_x(x,z)\, d_y(y,z). \tag{6}$$

In our model, dose is calculated only in the xz plane; however, our model is derived from the standard dose equations detailed above. Because the central-axis term in equation (3) is corrected to an infinitely broad field, side scatter equilibrium is assured. Under conditions of side scatter equilibrium, the reciprocity relationship (ICRU 1984) can be invoked to relate the dose calculated on the xz plane from a broad beam to the dose from a pencil beam, integrated over $-\infty$ to ∞ along the y-axis. Therefore, our model effectively assumes that our calculation phantom is a right cylinder, infinite in the z-direction with a planar cross section xz (shown as a step phantom in Figure 2.1(b)). An illustration of all the degrees of freedom included in our dose calculation model is provided in Figure 2.2. By the reciprocity relationship, pencil beams must also extend infinitely in the y-direction (Figure 2.1(a), with y_{min} and y_{max} approaching infinity) and in this context they are more appropriately called strip beams.

Rewriting equation (2) using strip beams that are Δx wide, the dose to $P(x, y, z)$ is given by the following relation:

$$D(x, y, z) = \sum_i \int_{x_i - \Delta x/2}^{x_i + \Delta x/2} \int_{y_{min}}^{y_{max}} S(x_i, y)\, d(x - x', y - y', z)\, dx' dy', \tag{7}$$

where i is used to iterate over pencil beam strips. Using the separability relation shown in equation (6) for the pencil beam dose and setting $S(x_i, y) = 1$ for all pencil beams (since our model only accounts for beams with uniform incident fluence) gives the following relation:

$$D(x, y, z) = \left\{ \sum_i \int_{x_i - \frac{\Delta x}{2}}^{x_i + \frac{\Delta x}{2}} d_x(x - x', z)\, dx' \right\} \text{ x } \left\{ \int_{y_{min}}^{y_{max}} d_y(y - y', z)\, dy' \right\}. \tag{8}$$

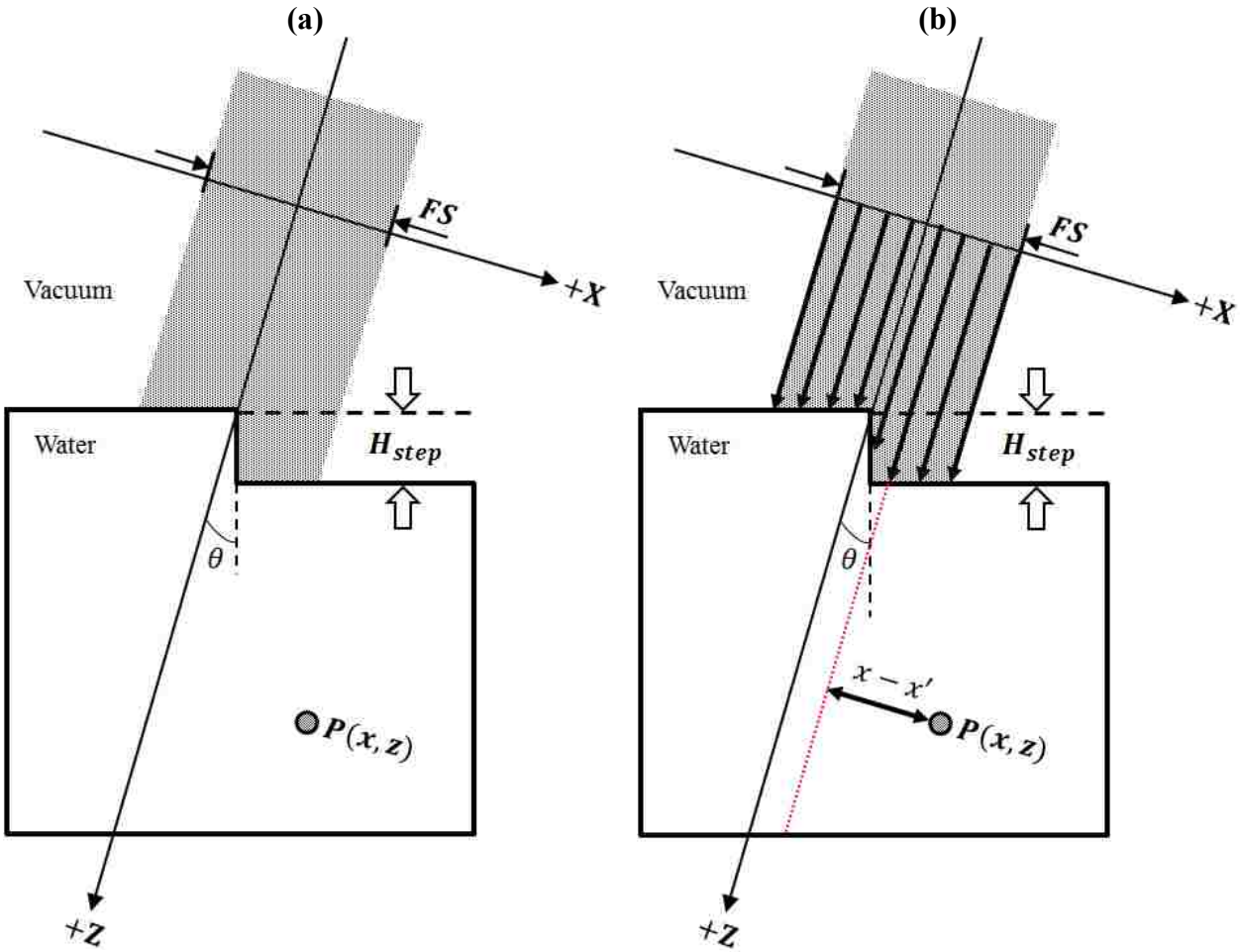

Figure 2.2: (a) The geometry of our dose calculation model. The incident beam is shown in grey shading at an oblique angle. The terms θ, H_{step}, and *FS* refer to the beam rotation angle, height of the step irregularity, and field size (all of which can be varied by the user), respectively. The dose is to be computed at the point *P(x,z)*. (b) The incident beam is segmented into one-dimensional pencil beams (strips), shown as black arrows in the grey shaded area. The central-axis of a pencil beam located at *x'* is shown extending through the phantom by a red dotted line, which is *x-x'* away from *P(x,z)* at depth *z*.

Substituting equation (3) for the pencil beam doses in equation (8) reduces the dose delivered to $P(x, y, z)$ to the following form:

$$D(x,y,z) = D^{\infty}_{expt}(0,0,z)\left\{\sum_i \int_{x_i-\frac{\Delta x}{2}}^{x_i+\frac{\Delta x}{2}} f_x(x-x',z)dx'\right\} \text{ x } \left\{\int_{y_{min}}^{y_{max}} f_y(y-y',z)\,dy'\right\}. \quad (9)$$

The solution to equation (9) was produced by substituting equations (5b) and (5c) into equation (9) and using the standard error function (denoted *erf*) relationship to a Gaussian,

$$\mathrm{erf}(z) = \frac{2}{\sqrt{\pi}} \int_0^z \exp\left(-z'^2\right) dz'. \tag{10}$$

The final solution to equation (9), obtained as described above, is a simple analytical formula for dose computation in terms of differences of error functions, given by

$$\begin{aligned} D(x,y,z) = {} & D_{expt}^{\infty}(0,0,z) \\ & \mathrm{x}\ \frac{1}{2}\left\{\mathrm{erf}\left[\frac{y_{max}-y}{\sqrt{2}\,\sigma(z)}\right] - \mathrm{erf}\left[\frac{y_{min}-y}{\sqrt{2}\,\sigma(z)}\right]\right\} \\ & \mathrm{x}\sum_i \frac{1}{2}\left\{\mathrm{erf}\left[\frac{x_i+\frac{\Delta x}{2}-x}{\sqrt{2}\,\sigma(z)}\right] - \mathrm{erf}\left[\frac{x_i-\frac{\Delta x}{2}-x}{\sqrt{2}\,\sigma(z)}\right]\right\}. \end{aligned} \tag{11}$$

The *erf* function in equation (11) is included as a routine in most standard computer programming languages, including MATLAB and C.

Since pencil beams in our model extend infinitely far out in the y-direction, as required by the reciprocity relationship, equation (11) can be used to calculate dose in the xz plane without regard to the y-dimension by allowing y_{max} and y_{min} in equation (11) to approach infinity. With y_{max} and y_{min} growing infinitely large, the second term in equation (11) approaches unity, ultimately removing the y-dependence from the equation; thus, the dose delivered to $P(x,z)$ (shown in Figure 2.2) for our model can be reduced to

$$\begin{aligned} D(x,z) = {} & \frac{D_{expt}^{\infty}(0,z)}{2} \\ & \mathrm{x}\sum_i \left\{\mathrm{erf}\left[\frac{x_i+\frac{\Delta x}{2}-x}{\sqrt{2}\,\sigma(z)}\right] - \mathrm{erf}\left[\frac{x_i-\frac{\Delta x}{2}-x}{\sqrt{2}\,\sigma(z)}\right]\right\}, \end{aligned} \tag{12}$$

where σ is the RMS width of the off-axis term.

Figure 2.2(a) illustrates all the degrees of freedom for the proposed model to illustrate the general design goal; namely, to calculate dose at an arbitrary point $P(x, z)$ in the xz plane given user-defined incident beam energy, field size, beam rotation angle, and phantom step height. Figure 2.2(b) illustrates how the pencil beam method can be used to achieve this design goal and equation (12) can be used to calculate dose to $P(x, z)$.

Materials encountered by pencil beams in Figure 2.2(b) are dependent on both the *x* and *z* coordinates in the target. However, it has become customary in PBAs to use the central-axis semi-infinite slab approximation (Hogstrom *et al.* 1981). In the central-axis semi-infinite slab approximation, materials encountered by the central-axis of each pencil beam are considered to be laterally homogeneous slabs along depth (Figure 2.3(b)); the use of Fermi-Eyges theory in deriving the off-axis term for pencil beams is therefore allowable since it only rigidly applies to semi-infinite slab geometry (see section D.1 in Appendix D).

The remaining undetermined $\sigma(z)$ in equation (12) is characterized by Fermi-Eyges theory. In the Hogstrom *et al.* (1981) PBA, $\sigma(z)$ was characterized by contributions from air (due to upstream beam elements) and contributions inside of the patient. Because the contribution from air to $\sigma(z)$ caused pencil beams to diverge to large sizes at the patient surface, small effects created by variations in the patient surface were being masked by the size of the pencil beams at the patient surface; Hogstrom *et al.* (1981) developed a unique solution to this problem, where a deconvolution between the contributions from air and the contributions inside the patient was performed. The resulting two-step calculation from this deconvolution greatly improved modeling of pencil beam effects due to the patient surface (Hogstrom *et al.* 1981).

Since our model assumes that all material upstream of the water phantom is vacuum (Figure 2.2), contributions to $\sigma(z)$ from air do not need to be characterized; therefore, a deconvolution does not need to be performed for our model. Applying Fermi-Eyges theory to

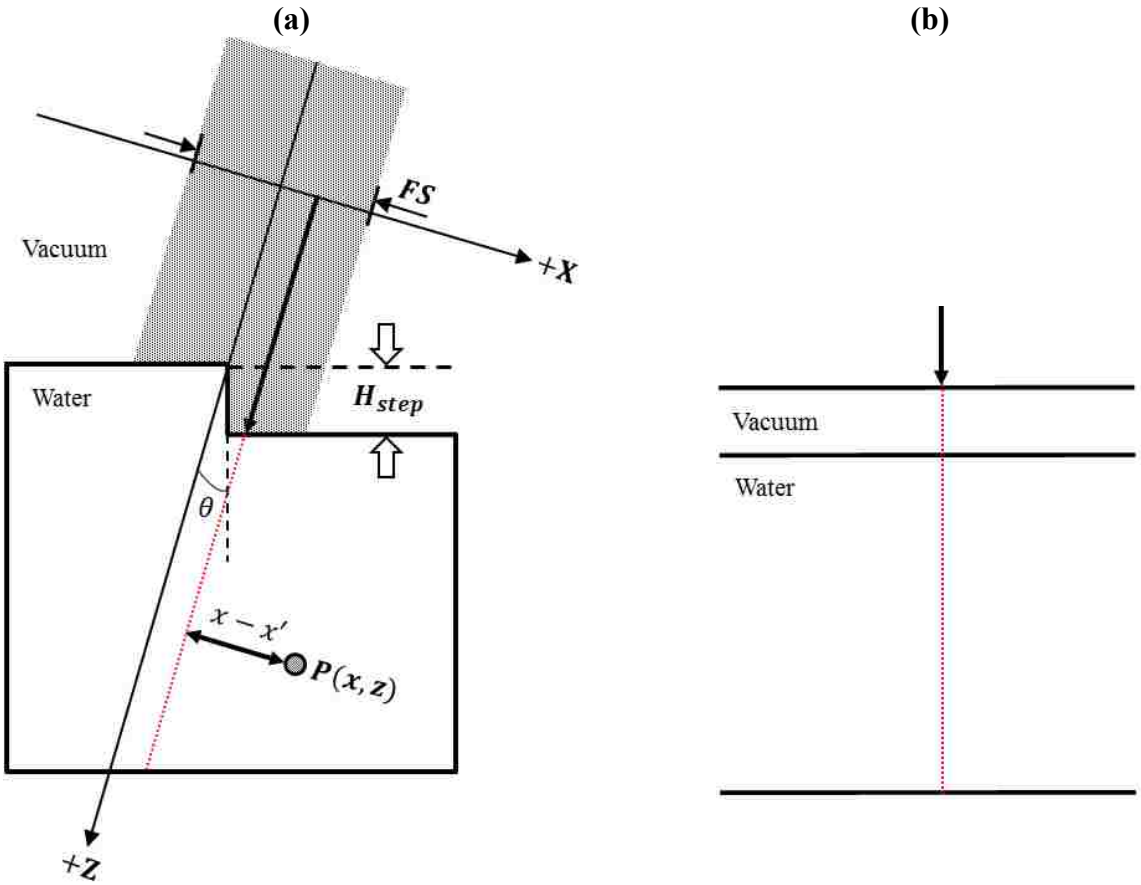

Figure 2.3: The phantom in Figure 2.2 is shown (a) with a single pencil beam located at *x'* with the central-axis of the pencil beam indicated by a red dotted line. (b) The material dependence for the pencil beam in (a) under the central-axis semi-infinite slab approximation is shown.

characterize the $\sigma(z)$ based on interactions in the phantom, we obtain

$$\sigma(z) = \sqrt{a_2(z)}, \tag{13}$$

where a_2 is the second scattering moment in Fermi-Eyges theory; a_2 characterizes increases in beam width due to scatter events inside the patient. All three scattering moments in Fermi-Eyges theory can be calculated using the formula

$$a_j(z) = \frac{1}{2}\int_0^z (z - z')^j \, T(E(z'))\, dz', \qquad j = 1,2,3, \tag{14}$$

where *j* refers to the *j*th moment of the theory, and $T(E(z'))$ is the linear angular scattering power evaluated at energy $E(z')$. There are several scattering power formulas available for

protons (Gottschalk 2010), and the formalism used for the present model is presented in section 2.1.2.

A constant of proportionality could have been included in equation (12), as in Koch *et al.* (2008), and after proper characterization it could have been used for absolute dose calculations. However, since our PBA was used only to determine relative dose, this parameter was unnecessary.

2.1.2 Dose Model

In the present work, pencil beams were modeled by two components, which could be thought of as two pencil beams in the same location: one to account for the effects on the beam width due to elastic "primary" scatter and one due to nonelastic "nuclear halo" events. In this work, we define "primary" scatter as elastic deflections experienced by the original protons in the incident beam (MCS, single scattering, and plural scattering) and the "nuclear halo" as those scatter events experienced by interaction products due to nonelastic nuclear interactions (Pedroni *et al.* 2005).

We calculated total dose using

$$D(x,z) = D_P(x,z) + D_N(x,z), \tag{15}$$

where $D_P(x,z)$ is the dose due to primary protons, and $D_N(x,z)$ is the dose due to nonelastic nuclear interactions. In the two sections that follow, the calculation of the primary and nuclear halo dose components will be discussed.

Four equations will be derived in the following two sections: (1) the primary and nuclear halo component of the total dose (*i.e.*, the $D_P(x,z)$ and the $D_N(x,z)$ in equation (15)); and (2) the primary and nuclear halo component of dose due to a single pencil beam. The latter of these requirements are needed to characterize free parameters in the nuclear halo pencil beam model.

Parameters describing the primary pencil beam model are determined by incorporating an analytical scattering power formula.

2.1.2.1 Primary Dose Model

The probability density of a primary point beam in our model was characterized by a Gaussian and Fermi-Eyges theory (Eyges 1948) was used to transport the pencil beam through the phantom. Thus, the form of equation (5b) was used to produce

$$f_p(x,z) = \frac{1}{\sqrt{2\pi}\,\sigma_P(z)} \exp\left[\frac{-x^2}{2\,\sigma_P^2(z)}\right], \tag{16}$$

where $\sigma_P(z)$ is the RMS width of the probability density of the primary point beam. The process in section 2.1.1 for determining total dose to $P(x,z)$ on the xz plane (equation (12)) was followed to derive the primary component of the total dose from equation (16), giving

$$D_P(x,z) = \frac{D_{expt}^{\infty}(0,z)}{2}\left(1 - W_N(z)\right) \\ \text{x} \sum_i \left\{ \text{erf}\left[\frac{x_i + \frac{\Delta x}{2} - x}{\sqrt{2}\,\sigma_P(z)}\right] - \text{erf}\left[\frac{x_i - \frac{\Delta x}{2} - x}{\sqrt{2}\,\sigma_P(z)}\right] \right\}, \tag{17}$$

where $W_N(z)$ is a weighting factor that is a free parameter of the model used to indicate the fraction of $D_{expt}^{\infty}(0,z)$ due to nonelastic nuclear events; hence, the $(1 - W_N(z))$ indicates the fraction of $D_{expt}^{\infty}(0,z)$ due to primary scatter events.

The remaining undetermined parameter $\sigma_P(z)$ in equation (17) was (all other parameters, except for $W_N(z)$, were determined from input data, which will be described in section 2.1.4) calculated using Fermi-Eyges theory, as shown in equations (13) and (14). To determine the linear angular scattering power required for Fermi-Eyges theory (equation (14)), the differential Moliere formula (Gottschalk 2010) was used. This scattering power formalism was chosen

because it applies to any material, including mixtures and compounds, and it accounts for increases in beam width due to MCS, single scattering, and plural scattering (Gottschalk 2010). The differential Moliere scattering power is defined as

$$T_{dM}(E(z)) = f_{dM}(pv, (pv)_0)\left(\frac{E_s}{pv}\right)^2 \frac{1}{X_s}, \tag{18}$$

where $(pv)_0$ is the initial momentum-velocity term, pv is the momentum-velocity term at depth z, f_{dM} is a correction factor, E_s is a constant value (15 MeV), and X_s is the scattering length (Gottschalk 2010). The momentum-velocity terms have the standard kinematic relation to the proton beam energy (see equation (56) in Appendix D.2). Figure 2.4 shows a plot of this scattering power versus energy for three different materials. Note that for energies near the incident beam energy (300 MeV was used as the incident energy in these plots) there is a small buildup effect. This effect shows that the differential Moliere calculation incorporates a single scattering correction (Gottschalk 2010).

Without f_{dM} in equation (18), the scattering power would only account for increases in beam width due to MCS (Gottschalk 2010). Thus, f_{dM} allowed the primary dose model to account for higher-order scatter events (single and plural scattering) in addition to MCS. This correction factor was calculated (following Gottschalk) using

$$\begin{aligned} f_{dM} = {} & 0.5244 + 0.1975\ \log_{10}(1 - (pv/(pv)_o)^2) \\ & + 0.232\ \log_{10}(pv) \\ & - 0.0098\ \log_{10}(pv)\log_{10}(1 - (pv/(pv)_o)^2). \end{aligned} \tag{19}$$

To evaluate the energy-dependence in equations (18) and (19), the proton energy was calculated at each depth z_j using the continuous slowing down approximation (CSDA), giving the energy at depth z_j as

$$E(Z_j) = E(Z_{j-1}) - \left\{\frac{-dE}{dz}\left[E(Z_{j-1})\right]\right\}\Delta Z, \tag{20}$$

where the term in braces is the linear stopping power, and $E(Z_{j-1})$ is the proton energy before the integration step $\Delta Z = Z_j - Z_{j-1}$. The material-dependence of the differential Moliere scattering power was incorporated in a term referred to as the scattering length, which was calculated (following Gottschalk) by

$$\frac{1}{\rho X_s} = \alpha\, N_A\, r_e^2\, \frac{Z^2}{A}\left(2\, \log\left(33219\, (AZ)^{-1/3}\right) - 1\right), \tag{21}$$

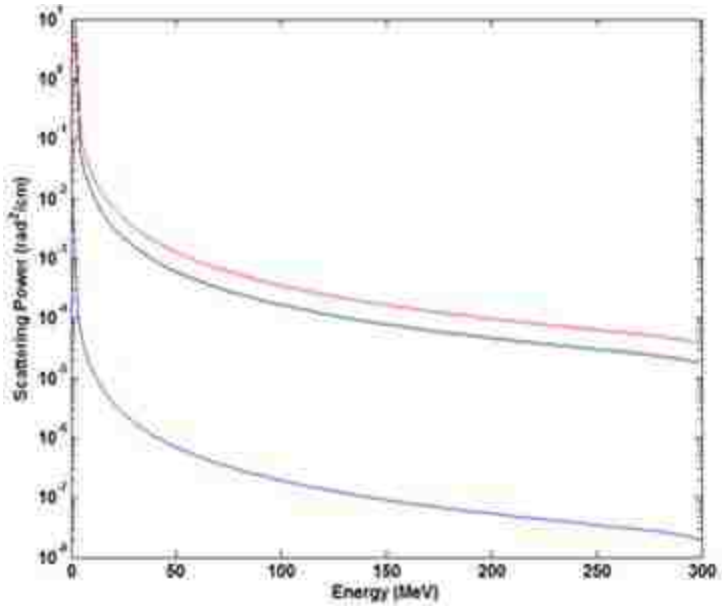

Figure 2.4: Scattering power vs. energy for three materials: water (black), compact bone (red), and air (blue).

where N_A is Avogadro's number, r_e is the classical electron radius, α is the fine structure constant (1/137), and $\rho, Z,$ and A refer to the mass density, atomic number and atomic mass of a particular element, respectively (Gottschalk 2010). In compounds and mixtures, the scattering length equation obeys a Bragg rule,

$$\frac{1}{\rho X_s} = \sum_i w_i \left(\frac{1}{\rho X_s}\right)_i, \tag{22}$$

where w_i refers to the fraction by mass of the *i*th element in the compound or mixture (Gottschalk 2010). Equations (21) and (22) were evaluated for water in our model.

2.1.2.2 Nuclear Halo Dose Model

As discussed in section 1.1.3, the reduction of primary fluence by nonelastic nuclear events induces short-range interaction products that determine the width of the "nuclear halo" (Pedroni *et al.* 2005, Soukup *et al.* 2005); therefore, the nuclear halo fluence is dependent on the primary fluence. In our model, we accounted for this effect by first assuming that the probability density for a point beam to undergo a nonelastic nuclear interaction was given by

$$p_{NUC}(x,z) = \frac{1}{\sqrt{2\pi}\,\sigma_{NUC}(z)} \exp\left[\frac{-x^2}{2\,\sigma_{NUC}^2(z)}\right], \tag{23}$$

where $\sigma_{NUC}(z)$ describes the RMS width of this distribution. The convolution of $p_{NUC}(x,z)$ and $f_p(x,z)$ produced the final result for the nuclear halo fluence in equation (24d), using Fourier analysis as detailed in equations (24a-c).

$$f_N(x,z) = f_P(x,z) \otimes p_{Nuc}(x,z) \tag{24a}$$

$$\mathcal{F}\{f_N(x,z)\} = \mathcal{F}\{f_P(x,z)\}\,\mathcal{F}\{p_{NUC}(x,z)\} \tag{24b}$$

$$f_N(x,z) = \mathcal{F}^{-1}\{\exp[-2\pi^2 k^2(\sigma_P^2(z) + \sigma_{NUC}^2(z))]\} \tag{24c}$$

$$f_N(x,z) = \frac{1}{\sqrt{2\pi}\,\sigma_N(z)} \exp\left[\frac{-x^2}{2\,\sigma_N^2(z)}\right], \tag{24d}$$

where

$$\sigma_N(z) = \sqrt{\sigma_P^2(z) + \sigma_{NUC}^2(z)}. \tag{25}$$

The nuclear halo component of the total dose was found by using the procedure in section 2.1.1, giving

$$D_N(x,z) = \frac{D^{\infty}_{expt}(0,z)}{2} W_N(z) \\ \text{x} \sum_i \left\{ \text{erf}\left[\frac{x_i + \frac{\Delta x}{2} - x}{\sqrt{2\,[\sigma_P^2(z) + \sigma_{NUC}^2(z)]}} \right] - \text{erf}\left[\frac{x_i - \frac{\Delta x}{2} - x}{\sqrt{2\,[\sigma_P^2(z) + \sigma_{NUC}^2(z)]}} \right] \right\}. \quad (26)$$

Total dose was determined by substituting equations (17) and (26) into equation (15). The remaining undetermined parameters in the total dose equation include $W_N(z)$ and $\sigma_{NUC}(z)$. No standard theory has been proposed to account for these values, so we fit our total dose to input data. However, equations (17) and (26) require a summation over pencil beams, which could introduce time-consuming and unnecessary complexities in the fitting procedure. Instead, we fit the total dose due to a single pencil beam with MC data using a field size narrow enough to be considered equal to the width of a pencil beam (*i.e.,* $FS = \Delta x$). The nuclear halo component of the dose due to a single pencil beam centered at $x_i = 0$ was determined from equation (26) as

$$D_N^{PB}(x,z) = \frac{D^{\infty}_{expt}(0,z)}{2}\, W_N(z) \\ \text{x} \left\{ \text{erf}\left[\frac{x + \frac{\Delta x}{2}}{\sqrt{2\,[\sigma_P^2(z) + \sigma_{NUC}^2(z)]}} \right] - \text{erf}\left[\frac{x - \frac{\Delta x}{2}}{\sqrt{2\,[\sigma_P^2(z) + \sigma_{NUC}^2(z)]}} \right] \right\}. \quad (27)$$

The primary component of the dose due to a single pencil beam centered at $x_i = 0$ was determined from equation (17) as

$$D_P^{PB}(x,z) = \frac{D^{\infty}_{expt}(0,z)}{2}(1 - W_N(z)) \left\{ \text{erf}\left[\frac{x + \frac{\Delta x}{2}}{\sqrt{2}\,\sigma_P(z)} \right] - \text{erf}\left[\frac{x - \frac{\Delta x}{2}}{\sqrt{2}\,\sigma_P(z)} \right] \right\}. \quad (28)$$

Thus, the total dose due to a single pencil beam is given by equations (15), (27) and (28):

$$D_{PB}(x,z) = D_P^{PB}(x,z) + D_N^{PB}(x,z). \tag{29}$$

The fitting procedure was accomplished by using the numerical Levenberg-Marquardt method (Madsen 2004) to fit equation (29) with input narrow field dose data. As mentioned previously, the input dose data was required to have a field size equivalent to the pencil beam width ($FS = \Delta x$) and was required to be determined in water. The fitting procedure was accomplished by finding the parameters $W_N(z)$ and $\sigma_{NUC}(z)$ that minimize the objective function

$$\sum_{k=k_{min}}^{k_{max}} \left\{D_{PB}(x_k, z_j) - D_{expt}^{PB}(x_k, z_j)\right\}^2, \qquad for\ z_j = (j - 0.5)\Delta z,$$
$$\Delta z = 1mm\ (0.25mm\ near\ Bragg\ peak), \tag{30}$$
$$j = 1,2,3,\dots,N-2,N-1,N$$

where $D_{expt}^{PB}(x,z)$ refers to the input narrow field dose data (experimentally determined), k_{min} is the pixel index of the minimum *x*-coordinate in the input data, k_{max} is the pixel index of the maximum *x*-coordinate in the input data, and N is the number of pixels in the *z*-direction in the input narrow field data.

The *lsqnonlin* MATLAB routine was used to implement the Levenberg-Marquardt fit of the model function (equation (29)) to the experimentally determined data. The initial guesses for the *lsqnonlin* routine were set to unity for all depths. At some depths, the model would not converge to a local minimum but still produced results that matched well. In practice, it was found necessary to manually manipulate the fit data by small amounts in areas that would not converge (figures showing the actual fit data are in Chapter 3).

2.1.3 Model Input Data

2.1.3.1 User Input

In the initialization of the PBA, several parameters were requested from the user to determine the setup of the dose calculation, including: (1) the nominal beam energy at the water surface (only energies of 50, 100, 150, 200, and 250 MeV were allowed); (2) the field size on the water surface (only field sizes of 4x4 cm^2 or 10x10 cm^2 were allowed); (3) the beam rotation angle (only angles 0^o and 45^o were allowed), defined as the angle formed between the beam axis and the positive *z*-axis (see Figure 2.2); (4) the height of the step irregularity on the phantom surface (only step heights of 0, 1, and 4 cm were allowed, and were only used for 0^o beam rotation); (5) the pencil beam width; and (6) the simulation step size, defined as the sampling increment in depth.

2.1.3.2 Materials and Elements

A material and element database was created, along with custom material editing and material property extraction routines in MATLAB. For each material that was desired to be included in the PBA, a corresponding PSTAR (Berger *et al.* 2005) stopping power and range versus energy table was required. In addition, all desired materials required material definition tables and element definitions. The material definition table was implemented in the form of an input text file, with the following properties specified for each material: (1) material name; (2) material density; (3) number of elements in material; (4) elemental composition of material (*e.g.,* H2O); (5) atomic number of each element in material; (6) atomic mass of each element in material; and (7) density of each element in material. The material database was designed to match the material parameters specified in the PSTAR material composition database (Berger *et al.* 2005).

Individual element parameters were also required, and placed in a separate input text file (so that, for instance, the atomic number of hydrogen could be quickly located rather than searching through the material database). This element input text file contained: (1) the element symbol; (1) the atomic number; (2) the atomic mass; and (3) the standard density.

The stopping power as a function of energy was accounted for by using the PSTAR (Berger *et al.* 2005) database. A separate PSTAR table was included for each material defined in the PBA material database. These tables were interpolated, using the *cubic spline* method in MATLAB, to a resolution of 0.5 MeV steps with a minimum energy of 0.5 MeV and a maximum energy of 300 MeV, which covers the energy range of interest. The format of the PSTAR text files included three columns: (1) energy, (2) stopping power, and (3) CSDA range. Figure 2.5 shows the stopping power versus energy for three different materials, extracted from the PSTAR text files.

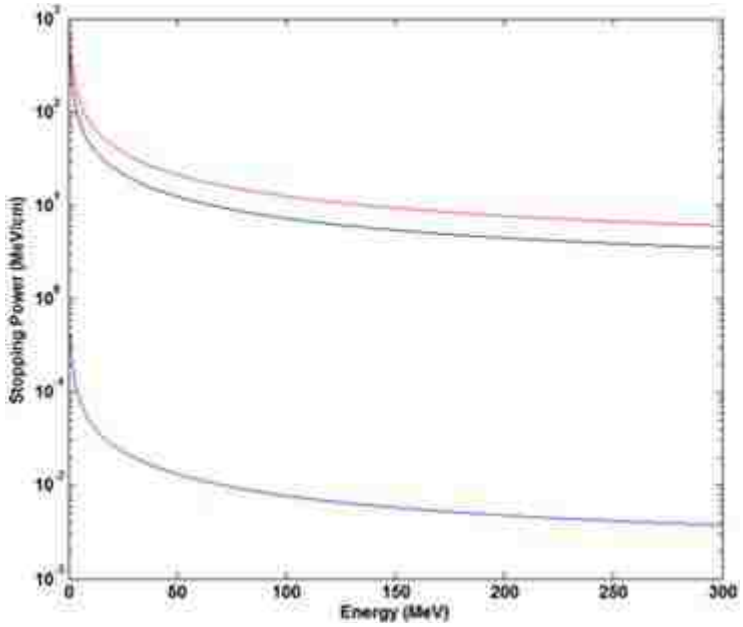

Figure 2.5: Stopping power vs. energy for three materials: water (black), compact bone (red), and air (blue).

2.1.4 Algorithm Design

The dose calculation model described in section 2.1.2 was coded in MATLAB version R2011a (7.12.0.635) and was optimized for speed using the C language editor in Microsoft Visual Studio 2010. The final version of the code was compiled using GCC 4 on Macintosh OS X and Linux operating systems. The GNU scientific library (GSL) was implemented into the C version of the code to provide equivalents for some matrix operations present in the original MATLAB code. Flowcharts showing the overall design of the algorithm are provided in Appendix A.

Dose calculations were performed in the frame of the beam (*e.g.,* the geometry shown in Figure 2.6(a) represents the geometry in Figure 2.2 converted to the frame of the beam). The dose calculation points in the beam frame, hereafter referred to as the dose grid, were spaced apart laterally (Δx in Figure 2.6(a)) by the pencil beam width and in depth (Δz in Figure 2.6(a)) by the simulation step size. The lateral dose grid coordinate limits were set to the field size with a 2 cm margin on either side of the field. The coordinates along the *z*-axis began at $^{\Delta Z}/_{2}$ and ended 2 cm beyond the proton range in water (calculated using $R = 2.2x10^{-3}E_0^{1.77}$, where E_o was the incident proton energy at the phantom surface). Coordinates of the dose grid were required to be multiples of $^{\Delta X}/_{2}$ in the *x*-direction and $^{\Delta Z}/_{2}$ in the *z*-direction. These constraints ensured that our calculation points were grid-centered. The phantom was designed as a closed contour on the dose grid and was modified according to user input parameters (an example step phantom at an oblique angle is shown in Figure 2.6(a)). The dose was calculated using the dose grid in the beam frame (Figure 2.6(a)), and the final dose distribution was transformed back to the phantom frame using a rotation matrix after the dose calculation ended (Figure 2.6(b)).

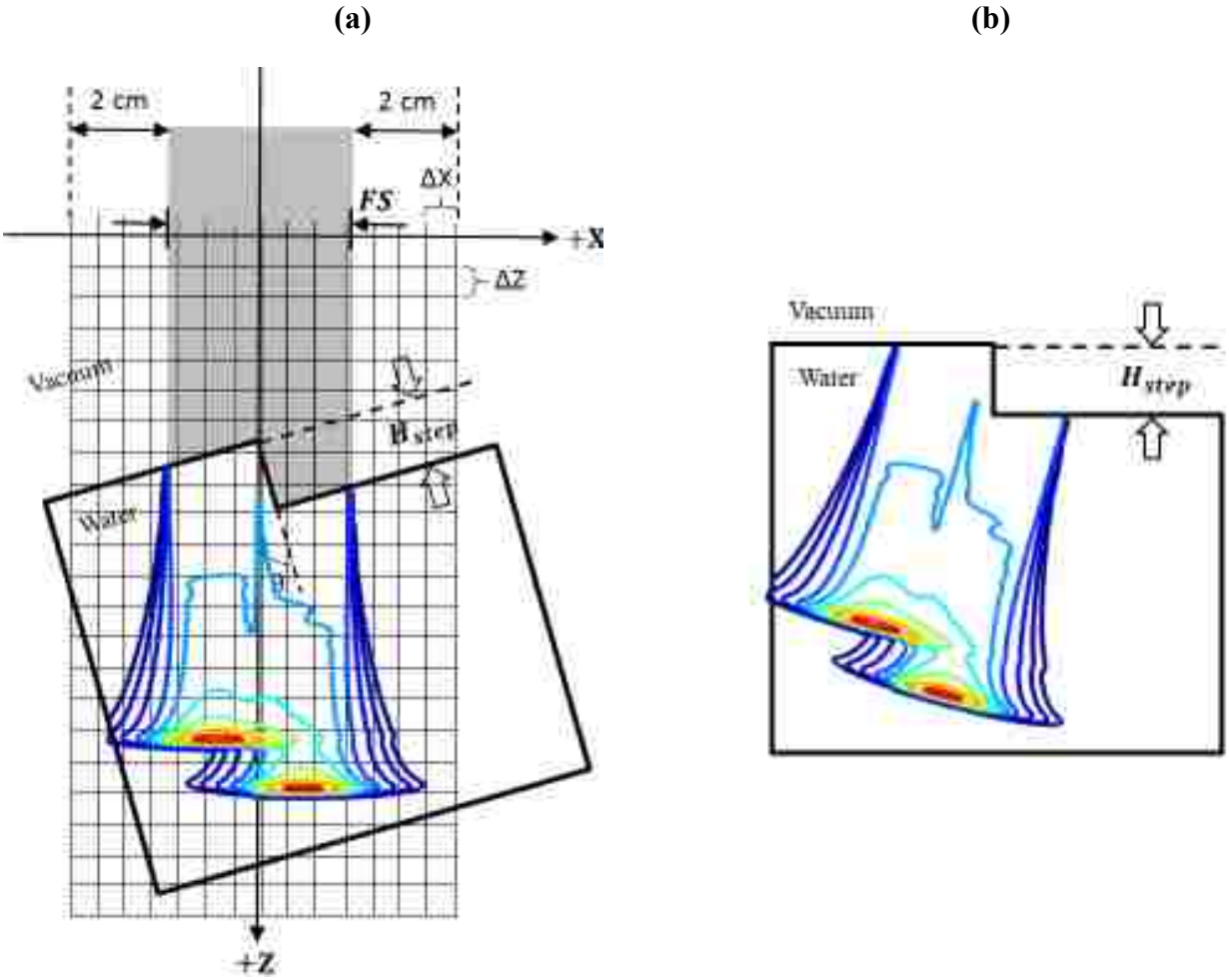

Figure 2.6: Geometry for the ray-trace and dose calculation procedure, illustrated for the phantom shown in Figure 2.2. See text for detailed description. (a) The ray-trace and dose calculation are performed in the beam frame, and (b) a coordinate rotation is applied to transform the dose calculation back to the phantom frame.

However, before the dose calculation was executed, the primary sigma and the effective depth (to be defined in this section) were determined for each pencil beam. These values were determined using a ray-trace along the central-axis of each pencil beam from the minimum z-coordinate to the maximum z-coordinate in the dose grid. In this section, the symbols i and j are used to indicate the pixels encountered in the ray-trace, referring to dose grid coordinates along the x-axis and z-axis, respectively; in this notation, it is implicit that pixels along the x-axis (from left to right) were numbered $i = 1,2,3, \ldots, N_X - 2, N_X - 1, N_X$, and pixels along the z-axis (from

top to bottom) were numbered $j = 1,2,3, \ldots, N_Z - 2, N_Z - 1, N_Z$, where N_X indicates the number of pixels in the *x*-direction and N_Z is the number of pixels in the *z*-direction.

As rays traversed the dose grid, the material composition of the patient was determined by whether or not the ray was within the contour at each pixel (*i.e.*, ray points within the contour were assigned to water while points outside of the contour were assigned to vacuum). A routine was coded in MATLAB to determine whether or not points were within the contour by counting the number of times each ray crossed a line segment forming the phantom contour. For points along each ray where the number of intersections were odd, those points were designated as inside the contour. For an even number of intersections, those points were considered to be outside of the contour. Because the central-axis semi-infinite slab approximation was used for pencil beams (Hogstrom *et al.* 1981), the step size of the dose grid directly set the sampling resolution of the materials in the phantom for each pencil beam (see Figure 2.3).

The calculation of the primary beam sigma $\sigma_P(z)$ required the integration in equation (14), which was calculated in our algorithm using a recursion relation (Hogstrom 1987):

$$(\sigma_P^2)_{i,j} = a_2^{i,j} \tag{31}$$

where

$$a_2^{i,j} = a_2^{i,j-1} + 2\Delta z\, a_1^{i,j-1} + (\Delta z)^2 a_0^{i,j-1} + \frac{(\Delta z)^3}{6}\, T_{dM}\left(E_{i,j}\right) \tag{32a}$$

$$a_1^{i,j} = a_1^{i,j-1} + \Delta z\, a_0^{i,j-1} + \frac{(\Delta z)^2}{4}\, T_{dM}\left(E_{i,j}\right) \tag{32b}$$

$$a_0^{i,j} = a_0^{i,j-1} + \frac{\Delta z}{2}\, T_{dM}\left(E_{i,j}\right), \tag{32c}$$

$a_2^{i,1} = a_1^{i,1} = a_0^{i,1} = 0$, and $\Delta z = z_j - z_{j-1}$.

The proton energy was determined using stopping power data provided by the PSTAR data tables (Berger *et al.* 2005). Thus, the proton energy at depth z_j was given by the continuous slowing down approximation (CSDA) as

$$E_{i,j} = E_{i,j-1} - \left[\frac{-dE}{dz}\left(E_{i,j-1}\right)\right]_{mat_{i,j}} \Delta z, \tag{33}$$

where $\left[\frac{-dE}{dz}\left(E_{i,j-1}\right)\right]_{mat_{i,j}}$ is the stopping power determined from PSTAR lookup tables for the energy $E_{i,j-1}$ and for material $mat_{i,j}$. We required the initial energy $E_{i,1}$ to be equal to the user-input incident beam energy E_o; setting the constraints $E_{i,0} = E_o$ and $\left[\frac{-dE}{dz}\left(E_{i,0}\right)\right] = 0$ in equation (33) satisfy this condition.

Since our model was designed for calculating dose in homogeneous water phantoms, it was desirable to calculate the depth accumulated in only those pixels assigned to water. In inhomogeneous phantoms, the effective depth (Hogstrom *et al.* 1981) is typically used to calculate the water equivalent depth (*i.e.*, the depth that would be required in a water phantom to give the same energy found at depth in the inhomogeneous phantom). However, because our model only uses vacuum and water, the effective depth calculation in our phantoms gives the same result as the cumulative depth in water (there are no energy losses in vacuum because the stopping power in vacuum is zero). We calculated the effective depth in the following manner,

$$Z_{eff}^{i,j} = Z_{eff}^{i,j-1} + \left\{\frac{\left[\frac{-dE}{dz}\left(E_{i,j-1}\right)\right]_{mat_{i,j}}}{\left[\frac{-dE}{dz}\left(E_{i,j-1}\right)\right]_{Water}}\right\} \Delta z, \tag{34}$$

where the term in braces is the stopping power ratio in material $mat_{i,j}$ encountered in the ray-trace to water, and we required that $Z_{eff}^{i,0} = 0$. The effective depth was used to select the appropriate depth in an input central-axis depth dose curve in water (*i.e.*, all equations using

$D_{expt}^{\infty}(0,z)$ were replaced by $D_{expt}^{\infty}\left(0,Z_{eff}^{i,j}\right)$. The stopping power ratio in $Z_{eff}^{i,j}$ was evaluated as an energy-dependent calculation (*i.e.,* to calculate the effective depth at pixel *(i, j)*, the stopping power ratio was determined for the energy at pixel *(i, j)*).

To decrease computation time, only those points within $4\sigma_N$ (recall that σ_N includes contributions from the primary and the nuclear halo RMS width) of the pencil beam axis were computed. Often, a smaller pencil beam modeling width is used to decrease simulation times (*e.g.,* $3\sigma_N$ would account for about 99.75% of the pencil beam distribution), but since our model produced simulation times less than 15 seconds for most configurations using $4\sigma_N$ (the longest simulation time was 40 seconds), this was not considered to have a significant impact on the simulation speed.

Since 4-sigma of a Gaussian distribution amounts to accounting for about 99.9999% of the Gaussian, it was necessary to normalize each pencil beam by multiplying it by 1.0001. However, the primary pencil beam was also modeled out to $4\sigma_N$ (which was much greater than $4\sigma_P$), so more than 99.9999% of the primary Gaussian was modeled. The normalization factor for the primary Gaussian was therefore dependent on both σ_{NUC} and σ_P. The derivation of this normalization factor is provided in Appendix B.

The lowest energy in the PSTAR input stopping power data files was 0.5 MeV, which was taken to be the cutoff energy for the present PBA. For energies below 0.5 MeV in the ray-trace, the scattering power evaluated at 0.5 MeV was used. For the calculation of the primary beam sigma in the ray-trace, any depth that exceeded that of the primary proton range was assigned the beam sigma calculated at the proton range. Finally, a maximum allowable energy was needed for evaluating equation (19), because for $pv = (pv)_0$, the logarithmic terms cause

f_{dM} to diverge. We found that setting $E_{max} = 0.95\ E_o$, where E_o refers to the incident energy, was sufficient to ensure convergence of the differential Moliere calculation.

2.2 Aim 2: Configure and Commission Algorithm Using Monte Carlo Simulations

2.2.1 Commissioning Data

The dose calculation model was commissioned using simulated dose distributions from a MC model of a simplified proton therapy beamline. This process has been demonstrated before by Newhauser *et al.* (2007b) and Koch *et al.* (2005). Monte Carlo N-Particle eXtended (MCNPX) version 2.7a was used to produce the required input distributions for the PBA. From this data, the central-axis percent depth dose (PDD) was extracted and this provided the required $D_{expt}^{\infty}(0,z)$ used in sections 2.1.1 and 2.1.2. These simulations were produced for five energies (50, 100, 150, 200, and 250 MeV), and two field sizes (4x4 cm^2 and 10x10 cm^2). The central-axis MC data is shown for 4x4 cm^2 and 10x10 cm^2 fields in Figure 2.7.

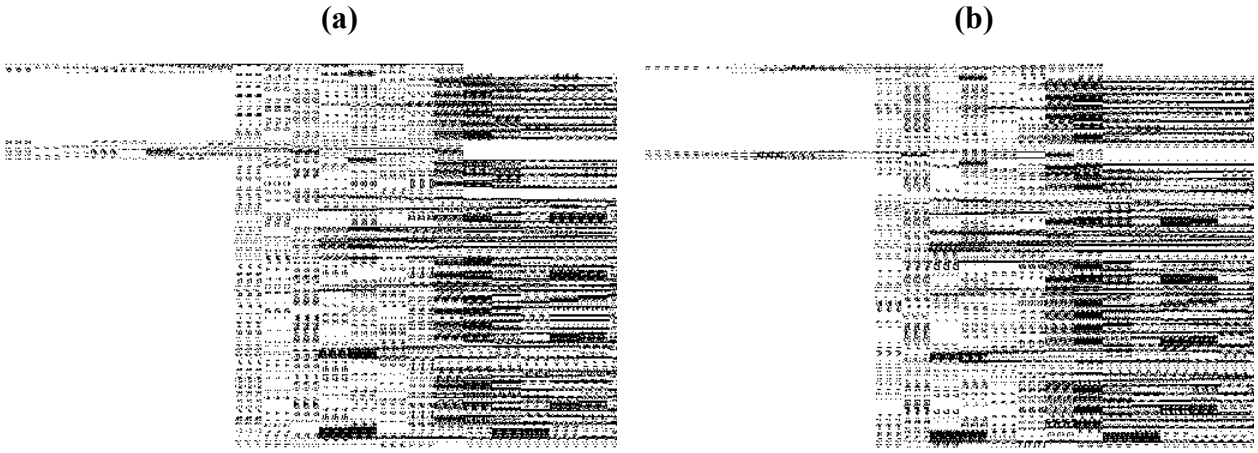

Figure 2.7: Monte Carlo central-axis data for (a) 4x4 cm^2 fields and (b) 10x10 cm^2 fields at energies of 50, 100, 150, 200, and 250 MeV. The decreased peak values in (b) compared to the values in (a) are due to the data being normalized to the tally volume and the increased tally size along the *x*-axis for 10x10 cm^2 simulations (-15 to 15 cm) relative to 4x4 cm^2 simulations (-6 to 6 cm). Since all simulations used a *y*-tally from -5 to 5 cm, the ratio of peak heights in (b) to (a) is given by the ratio of the tally width (*x*-direction) in (b) to the tally width (*x*-direction) in (a) (*i.e.,* 12/30 = 0.4).

2.2.2 Configuration Procedure

Proton dose distributions were simulated using a flat water phantom with a monoenergetic beam directed perpendicular to the surface of the phantom for five energies (50, 100, 150, 200, and 250 MeV) and two field sizes (4x4, and 10x10 cm^2). A type 3 mesh tally (energy deposited per particle, per volume) was used to score the particles in the simulations. The pixel size was 1 mm in width and was initially 1 mm in depth, changing to 0.25 mm near the Bragg peak. The physics card in these simulations was set to the default options, and only protons were tracked.

Since only xz plane data was required for commissioning our model, the reciprocity relationship (ICRU 1984) was used by setting a large tally in the *y*-direction. This design effectively captured more particles and improved statistics. The large tally technique is listed in the MCNPX manual (MCNPX 2005) as one of the standard variance reduction methods. In order to achieve statistical uncertainties better than 1% at the 1% of dose maximum level, Table 2.1 shows the number of histories needed for all incident beam energies in flat and oblique simulations; simulations using step irregularities required twice the number of histories shown in Table 2.1 to achieve the same level of statistical uncertainty.

The output files that were produced by the MC simulations had data organized into four columns: (1) the *x*-coordinates of each point in the MC dose matrix, (2) the *z*-coordinates of each point in the MC dose matrix, (3) the energy deposited in the voxel surrounding each point in the matrix, and (4) the uncertainty in the deposited energy at each point. A script was written in MATLAB to read in this data and convert the *x*-coordinates to a vector that contained unique *x*-values in ascending order (and the same was performed for the *z*-coordinates). The same script converted the column corresponding to the deposited energy into a matrix with each element in the new matrix corresponding to the energy deposited in that pixel. Since it was known that the

central column (or the average of the two central columns for distributions with an even number of columns) of the deposited energy matrix would contain the dosimetric center of the dose matrix, the input central-axis curve was assigned to be the central column through this matrix (or the average of the central two columns).

Table 2.1: Number of histories used in commissioning data for all incident beam energies.

Incident Beam Energy (MeV)	Number of Histories (x10^6)
50	100
100	150
150	200
200	250
250	500

It is imperative to require that the central-axis depth dose data satisfies side scatter equilibrium. This requirement arises from the fact that the model in section 2.1.2 directly determined particle fluence and relied on an external determination of energy loss ($D^{\infty}_{expt}(0,z)$) to convert fluence to dose. If the input depth dose data does not satisfy side scatter equilibrium, then scatter (already accounted for using particle fluence) becomes a measurable effect. Thus, we avoided modeling particle scatter twice by requiring the central-axis depth dose data satisfy side scatter equilibrium.

The central-axis depth dose data was extracted from flat phantom MC simulations for field sizes of 4x4 cm^2 and 10x10 cm^2; however, the required input data for the dose calculation model, $D^{\infty}_{expt}(0,z)$, needed to be determined from an infinitely broad field. Hogstrom *et al.* (1981) developed an analytical method to convert beams of any field size to an infinitely broad beam. However, these corrections are based on the amount of scatter that has occurred. Since

our dose model implements dose components from primary and nuclear halo events, we used two analytical corrections (one for the primary dose, another for the nuclear halo dose). Thus, the primary dose equations (equations (17) and (28)) in section 2.1 with $(1 - W_N(z))D^{\infty}_{expt}(0,z)$ should be substituted in the following manner,

$$(1 - W_N(z))\, D^{\infty}_{expt}(0,z) = (1 - W_N(z))\frac{D^{FS}_{MC}(0,z)}{\mathrm{erf}\left[\dfrac{FS}{2\sqrt{2}\,\sigma_P^W}\right]}, \qquad (35)$$

where $D^{FS}_{MC}(0,z)$ refers to the MC central-axis depth dose commissioning data, and σ_P^W refers to the primary beam sigma in a homogeneous water phantom (which is required since the MC data was calculated in a homogeneous phantom). Nuclear halo dose equations (equations (26) and (27)) in section 2.1 with $W_N(z)D^{\infty}_{expt}(0,z)$ should be substituted in the following manner,

$$W_N(z)\, D^{\infty}_{expt}(0,z) = W_N(z)\frac{D^{FS}_{MC}(0,z)}{\mathrm{erf}\left[\dfrac{FS}{2\sqrt{2[(\sigma_P^W)^2 + \sigma_{NUC}^2]}}\right]}. \qquad (36)$$

To provide the input dose data $D^{PB}_{expt}(x,z)$ in equation (30), narrow field MC dose distributions (1x1 mm^2 field size) were generated with MCNPX using a constant pixel size of 0.1 mm in the lateral direction and an initial pixel size of 1 mm in depth, changing to 0.25 mm near the proton range. Also, the lateral extent of the grid ranged from -5 to 5 cm so that the off-axis distribution due to nuclear halo events could be characterized over large distances. Pencil beam dose distributions were produced for five energies (50, 100, 150, 200, and 250 MeV).

2.3 Aim 3: Evaluate Dose Calculation Accuracy of Algorithm in Homogeneous Media

2.3.1 Evaluation Geometries

To evaluate the accuracy of the PBA, we compared PBA results with MC simulations in three geometries relevant to patient calculations (shown in Table 2.2). To gauge the ability of the PBA dose calculation to account for small and large field sizes, beams with field sizes of 4x4

cm^2 and 10x10 cm^2 were calculated for energies of 50, 100, 150, 200, and 250 MeV in a flat water phantom. The ability of the PBA to accurately determine dose in phantoms with irregular surfaces was evaluated using a phantom with a variable step height; step heights of 1 and 4 cm were tested. Finally, to understand the effects of beam obliquity, a rotated beam at 45 degrees was simulated by the PBA as well.

Table 2.2: Geometries used in evaluation of dose calculation accuracy.

Geometry	Description	Values	Purpose
Flat Phantom	Normally incident beam on flat phantom.	N/A	To test PBAs ability to predict dose for small/large field sizes.
Stepped Phantom	The surface on one half of the phantom is deeper than the other half.	1, 4 cm	To test PBAs ability to account for varying surface contours.
Oblique Phantom	Beam is delivered to a flat phantom at an oblique angle.	45 degrees	To test PBAs ability to predict dose from an oblique beam.

For all three of these geometries, dose calculations were produced by the PBA using a resolution of 1 mm by 1 mm in the dose calculation grid and pencil beams that were 1 mm wide (except for the 50 MeV simulations, which used a resolution of 0.25 mm by 0.25 mm in the dose calculation grid and pencil beams that were 0.25 mm wide – the 0.25 mm resolution was need in the 50 MeV case to reproduce the Bragg peak).

Because the MC data was taken at a much finer resolution that the PBA data (the step size reaches 0.25 mm near the Bragg peak in MC data), it was necessary to resample the MC distribution to be the same size and same resolution as the PBA dose grid. This resampling was performed by using the two-dimensional interpolation routine *interp2* provided by MATLAB.

2.3.2 Calculation of DTA and Percent Dose Difference

The distance-to-agreement (DTA) routine that was written for this project was based on an existing DTA program written by Mancuso (2011). This routine required the calculated PBA dose matrix, the MC dose matrix, the size of each pixel (required to be constant in the *x*-direction and the *z*-direction for both the MC and the PBA dose matrices), and the search radius as input parameters. Both the PBA and the MC dose matrices were required to have the same size and the same resolution. For MC dose matrices that did not satisfy this requirement, resizing and interpolation was performed. The PBA dose matrix was normalized to the maximum dose in a PBA-calculated flat phantom and the MC dose matrix was normalized to the maximum dose in a MC-calculated flat phantom. Most relative dose calculation methods use central-axis maximum normalization, but we chose to normalize our data to the maximum dose in a flat phantom because our commissioning data was only provided for flat phantom simulations.

The DTA routine iterated over all points in the MC matrix, and for each point *P* in the MC matrix, the same point *P* in the PBA dose matrix was located (Figure 2.8(a, and b)). A search area was formed by a rectangle in the PBA matrix whose edges were within a 1 cm search radius from *P* (Figure 2.8(b)). Given this search area, the *contourc* function in MATLAB was used to contour within the area for the dose value D (Figure 2.8(a)) in the MC matrix (Figure 2.8(c)). Once the coordinates of this contour were found, the DTA was calculated as the smallest distance between *P* and the contour as follows: (1) the closest point on the contour to *P* was found (the blue point in Figure 2.8(d)); (2) two adjacent points (*A* and *C* in Figure 2.8(e)) on either side of the closest point (*B* in Figure 2.8(e)) were chosen to form two line segments; (3) the line segment $\overline{AB}$ was compared to *P* by testing $\overrightarrow{(A-B)}\odot\overrightarrow{(P-A)}$ and $\overrightarrow{(B-A)}\odot\overrightarrow{(P-B)}$ (Figure 2.8(f)) and the line segment $\overline{BC}$ was compared to *P* by testing $\overrightarrow{(B-C)}\odot\overrightarrow{(P-B)}$ and

$\overrightarrow{(C-B)} \odot \overrightarrow{(P-C)}$, where $\odot$ indicates the operation of the dot product (Figure 2.8(g)); (4) if both dot products listed in step 3 for a given line segment are greater than or equal to zero, *P* is considered to be outside of the line segment and the DTA is calculated as the distance between the closest point and *P* (Figure 2.8(f)); otherwise, *P* is considered inside the line segment and the DTA is given by the perpendicular distance from the line segment to *P* (Figure 2.8(h)) using the outer product (equation (37)); (5) the smallest distance of all DTAs calculated in step 4 was used as the final DTA. For multiple contours at the dose value D, the smallest DTA from all contours was taken to be the final DTA.

Denoting an arbitrary line segment that *P* is considered to be inside of by $\overline{BC}$ (as shown in Figure 2.8(g)), the distance to agreement was calculated using

$$DTA = \frac{\overrightarrow{(C-B)}^{\perp} \odot \overrightarrow{(P-C)}}{\left\| \overrightarrow{(C-B)}^{\perp} \right\|}, \tag{37}$$

where $\overrightarrow{(C-B)}$ is a vector used to indicate the line segment $\overline{BC}$, $\overrightarrow{(P-C)}$ is the vector from *P* to *C*, $\overrightarrow{(C-B)}^{\perp}$ is the perpendicular vector to the line segment $\overline{BC}$, and $\left\| \overrightarrow{(C-B)}^{\perp} \right\|$ is the magnitude of vector $\overrightarrow{(C-B)}^{\perp}$.

Percent dose difference was calculated by taking the difference in the MC and the PBA results and dividing by the reference maximum in a flat phantom. The composite analysis used to evaluate the agreement between pencil beam and MC predictions was DTA $\leq$ 1mm or percent dose difference $\leq$ 2% of maximum dose. The metric used to indicate the agreement between the two distributions in the composite analysis was the percentage of points that satisfy these criteria. To avoid erroneous indications of passing pixel percentages, a dose threshold of 1% of the maximum dose was used.

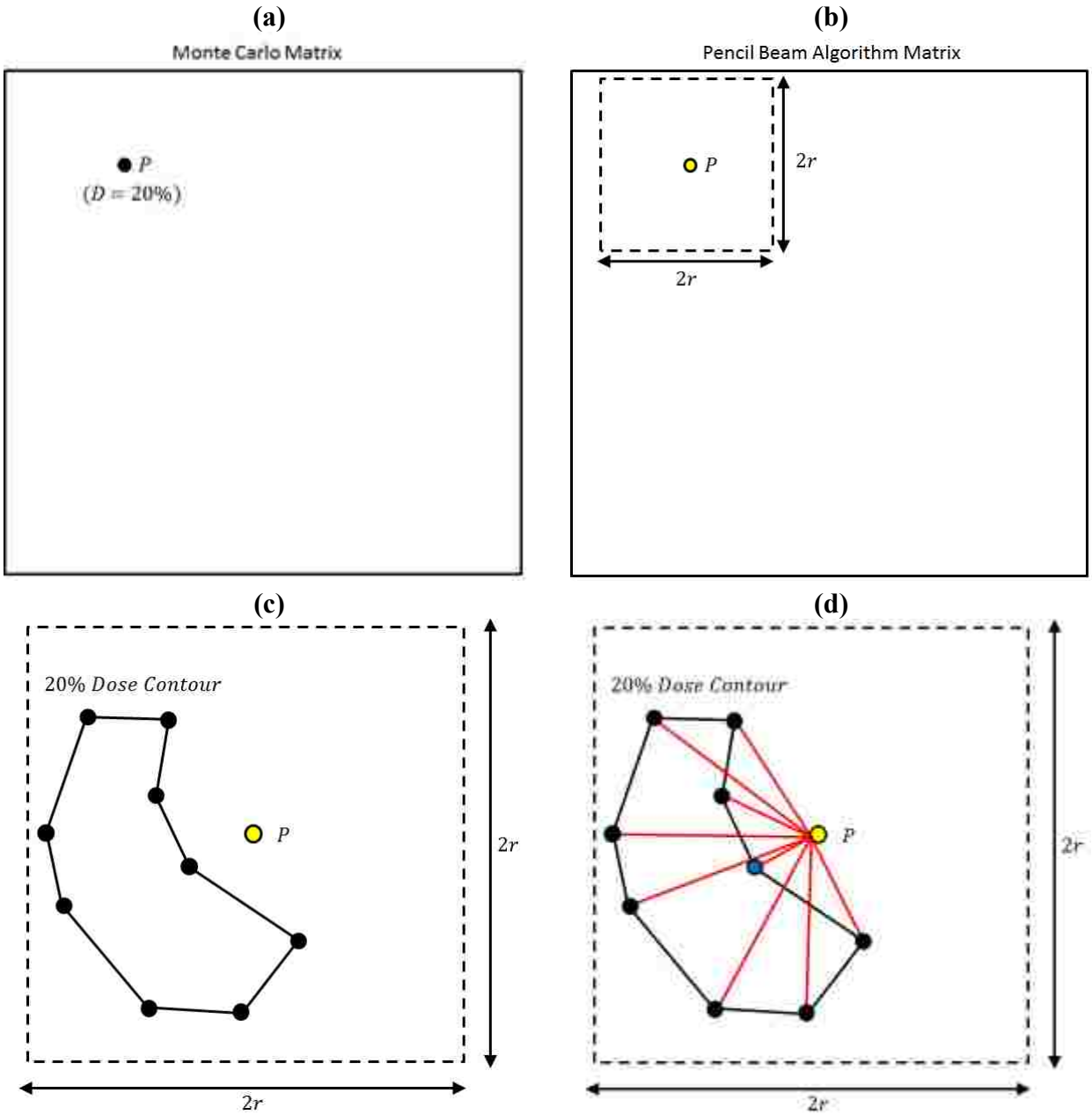

Figure 2.8: Step-by-step illustration of DTA calculation: (a) The MC dose matrix with a point *P* indicated with a relative dose value of 20%. (b) The same point is located in the PBA dose matrix and all points within the search radius *r* form a square of size *(2r)x(2r)*. (c) The search area is shown closeup, along with the 20% contour. The small dots indicate the coordinates that make up the closed contour. (d) The distance from each contour coordinate to the point *P* are shown in red, with the closest point shown in blue. (e) Two adjacent points (green and purple) to the closest point are shown. (f) To calculate DTA, first the line segment $\overline{AB}$ is considered, and it is clear that *P* is outside of $\overline{AB}$; thus, the DTA for this segment is the distance between *P* and *B*. (g) The line segment $\overline{BC}$ is considered. Since *P* is inside the line segment, the DTA is calculated as the perpendicular distance from $\overline{BC}$ to *P* by (h) finding the perpendicular cross-product between $\overline{BC}$ and *P* and normalizing that result by the magnitude of $\overline{BC}^{\perp}$(equation (37)).

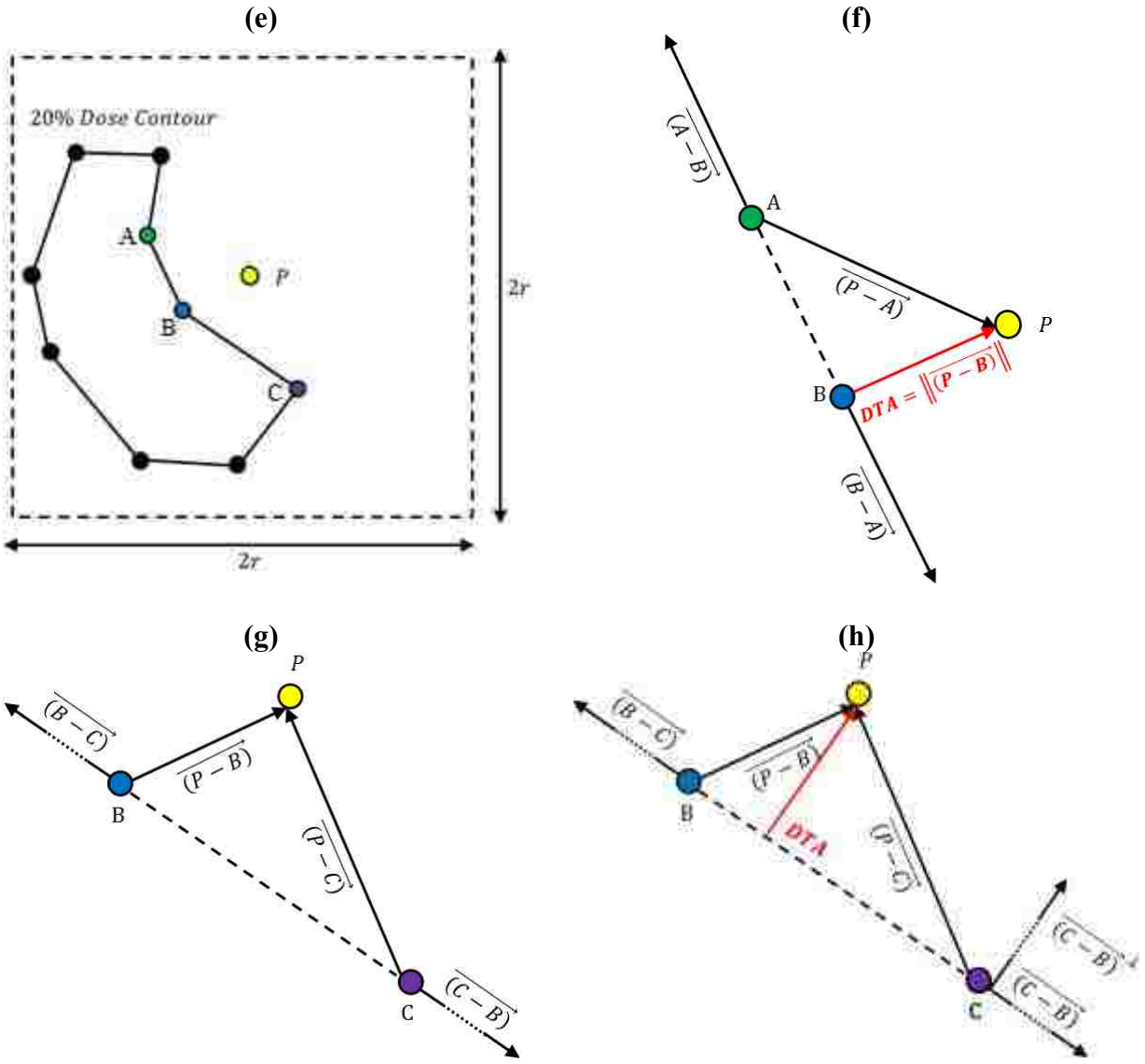

Figure 2.8 (continued)

CHAPTER 3. RESULTS

3.1 Nuclear Halo Parameterization Results

The Levenberg-Marquardt (LM) fits to the Monte Carlo (MC) pencil beam (1x1 mm^2 field size) data are compared to the MC data in Figure 3.1 below. This figure shows that the LM fit performed much better at deeper depths, where the MC data is more appropriately described by two Gaussians.

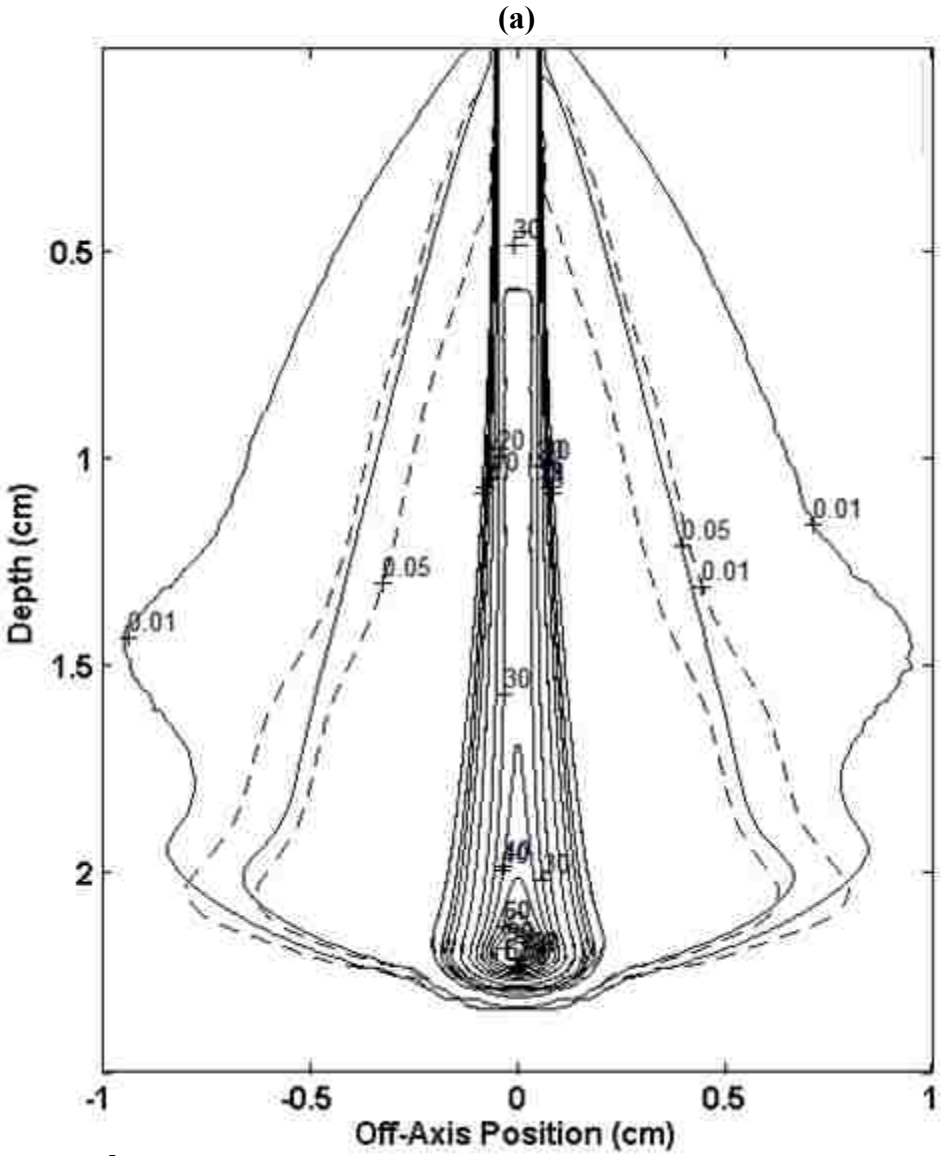

Figure 3.1: 1x1 mm^2 Monte Carlo data (solid) compared with nonlinear least squares Levenberg-Marquardt fit to the Monte Carlo data (dashed) with incident energies of (a) 50 MeV, (b) 100 MeV, (c) 150 MeV, (d) 200 MeV, and (e) 250 MeV. Isodose values are 100, 90, 70, 60, 50, 40, 30, 20, 10, 5, 3, 2, 0.05, and 0.01%.

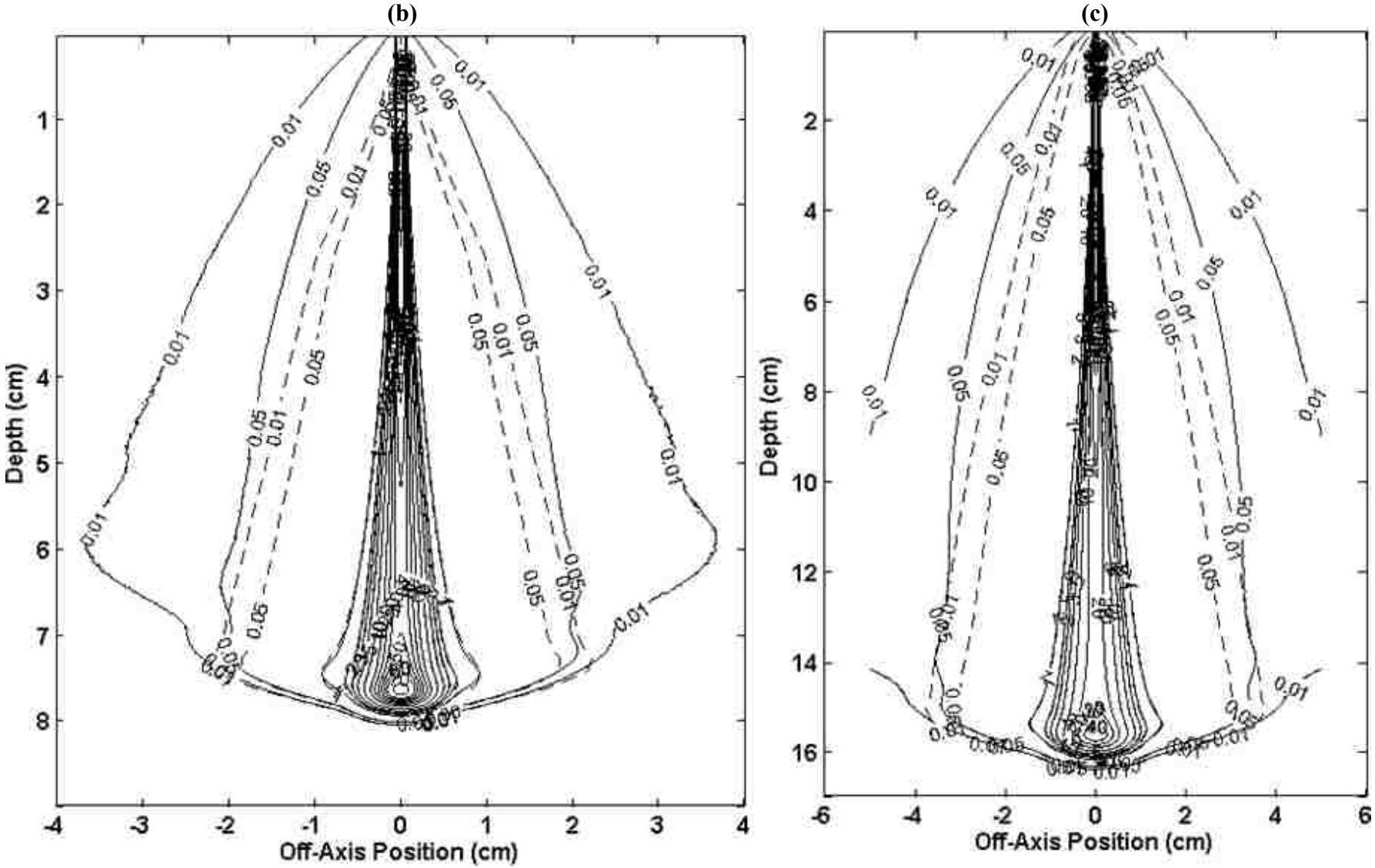

Figure 3.1 (continued)

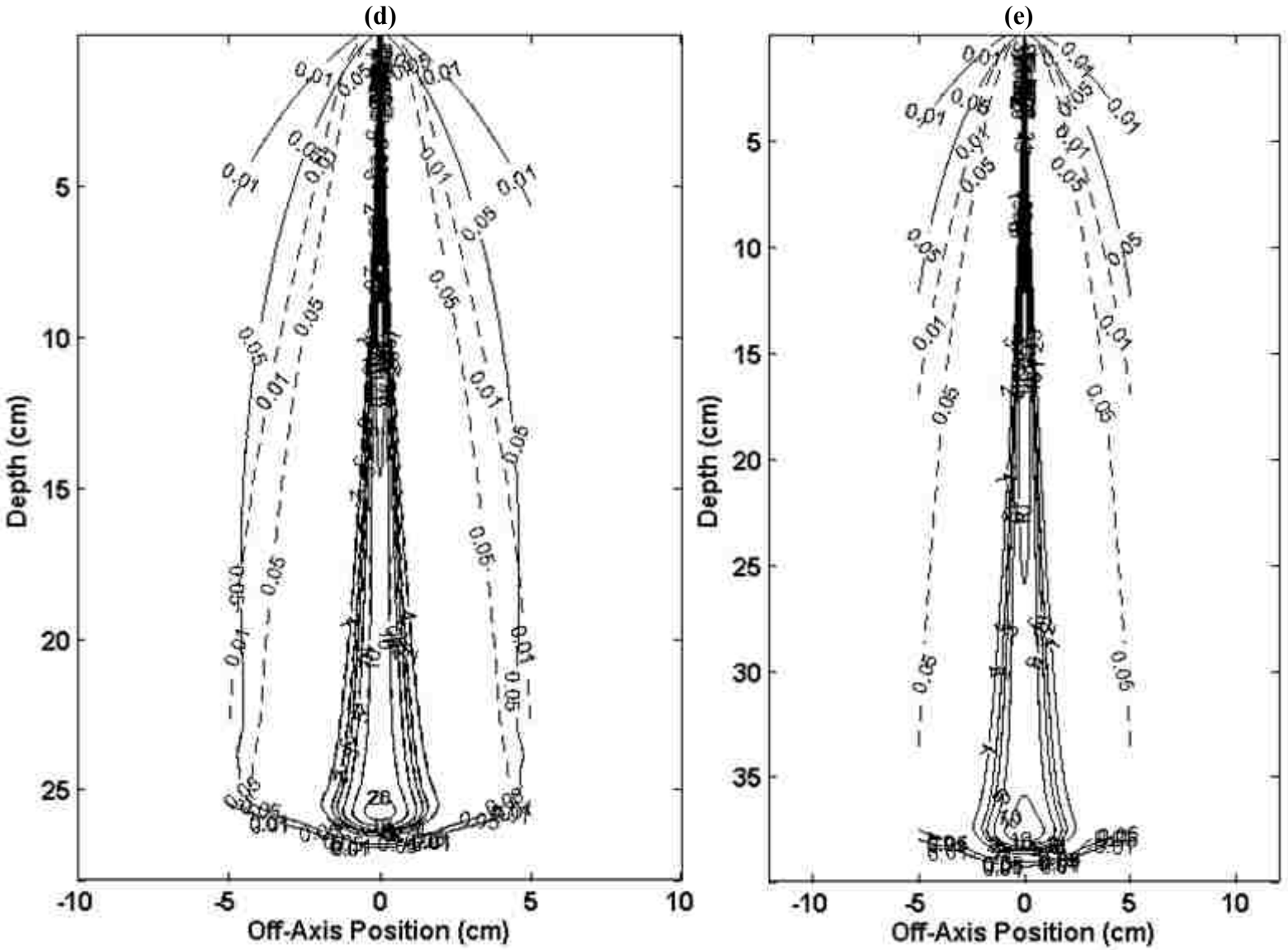

Figure 3.1 (continued)

The nuclear weighting factor and the nuclear sigma extracted from the LM fits are shown in Figure 3.2. Central-axis profiles through the MC and LM data are shown in Figure 3.3. Representative lateral profiles for a typical fit are shown in Figure 3.4 (remaining profiles in Appendix C). Figure 3.4 shows better agreement between the LM fit and MC data at deeper depths. Despite poor fitting at shallow depths, the nuclear halo model is an improvement over calculations limited to primary scatter and was considered sufficient for the current PBA.

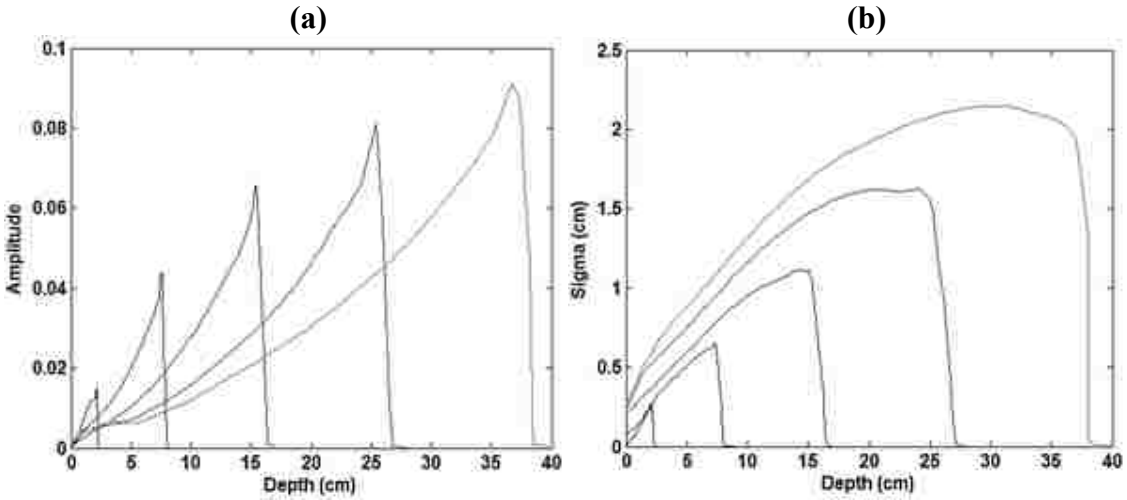

Figure 3.2: Parameters extracted from Levenberg-Marquardt fit to Monte Carlo data with 1x1 mm^2 field size. For energies of 50, 100, 150, 200, and 250 MeV, plots are shown of (a) nuclear amplitude vs. depth, and (b) nuclear sigma vs. depth.

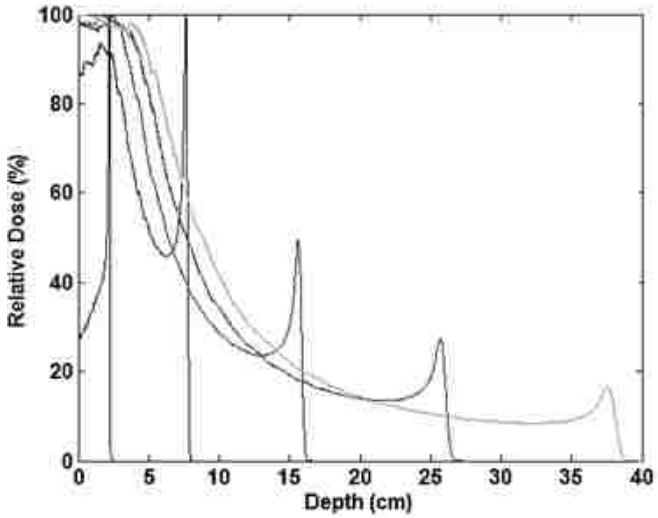

Figure 3.3: Central-axis data of Monte Carlo (MC) simulations (solid) and Levenberg-Marquardt (LM) fit (dashed). Differences between the MC and LM data cannot be seen in the figure as all are < 0.1 cm.

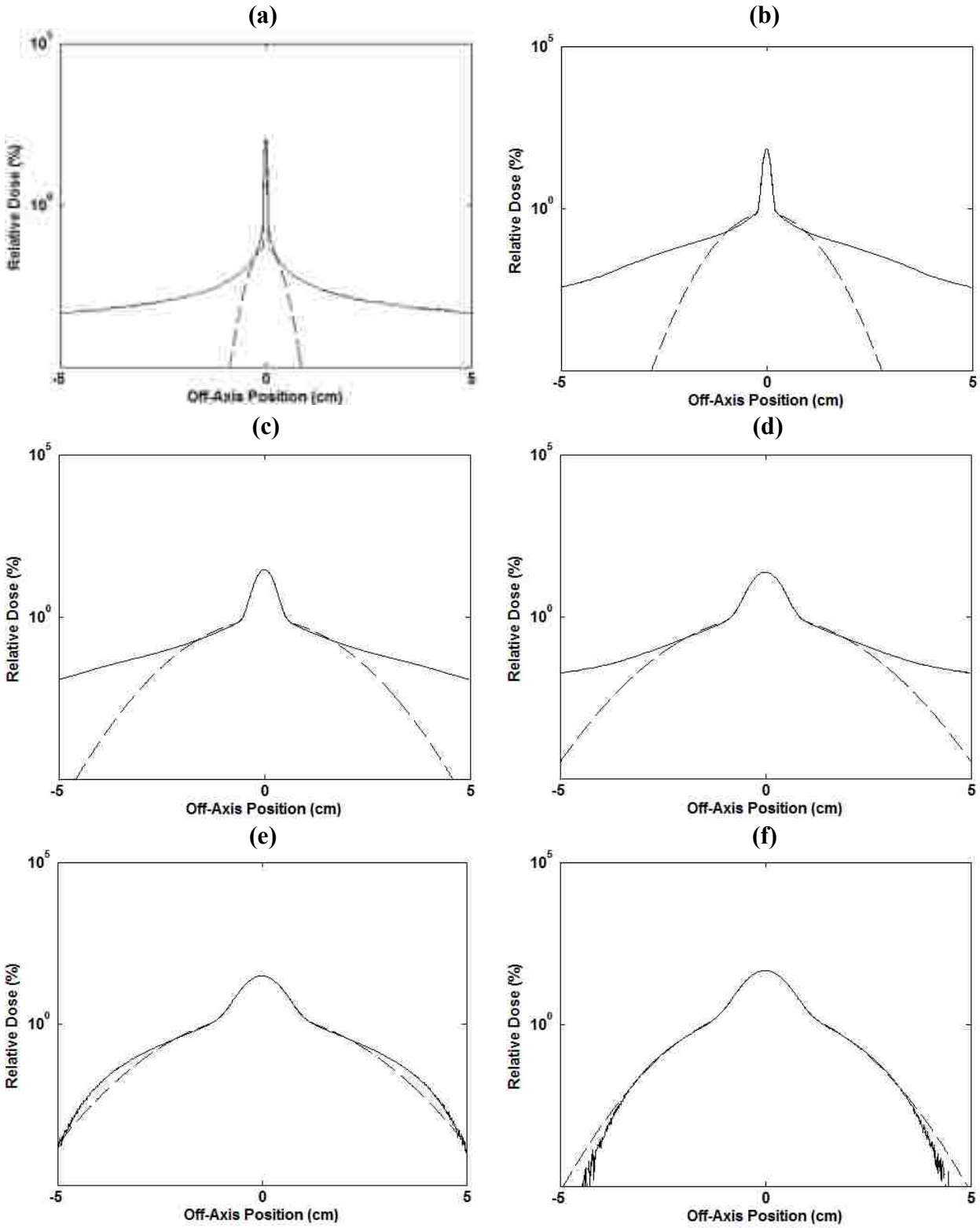

Figure 3.4: Representative lateral profiles through 150 MeV Monte Carlo data (solid) and the Levenberg-Marquardt fit to Monte Carlo data (dashed) at depths of (a) 0 cm, (b) 5 cm, (c) 10 cm, (d) 13 cm, (e) 15 cm, and (f) 15.5 cm.

3.2 Dose Calculation Results

In the following sections, isodose comparisons, lateral profiles, and central-axis profiles of the flat, step, and oblique phantom simulations are presented for MC and PBA data. Both 4x4 cm^2 and 10x10 cm^2 field data are shown at incident energies of 50, 100, 150, 200, and 250 MeV.

In Figure 3.5, isodose comparisons of the PBA and MC data are shown for beams of all energies with a 4x4 cm^2 field size, perpendicularly incident on a flat water phantom. Figure 3.6 shows the PBA and MC comparisons for this same set of energies with a 10x10 cm^2 field on a flat water phantom. Water phantoms with a 1 cm step for all five energies are shown in Figures 3.9 (4x4 cm^2 field) and 3.10 (10x10 cm^2 field). The step height is increased to 4 cm in Figures 3.11 (4x4 cm^2 field) and 3.12 (10x10 cm^2 field). Finally, results for a water phantom with a surface tilted 45 degrees relative to the direction of the beam are shown in Figures 3.17 (4x4 cm^2 field) and 3.18 (10x10 cm^2 field). In general, agreement was excellent for all distributions tested, with greater than 99% of points passing the composite criteria (DTA $\leq$ 1mm or percent dose difference $\leq$ 2%). All geometries passed DTA $\leq$ 1mm or percent dose difference $\leq$ 3% with 100% pass rate. In the following figures, areas in red indicate points that exceeded agreement criteria. Detailed discussions of all geometries are now provided.

3.2.1 Flat Phantom

The results for the 4x4 cm^2 flat phantom comparisons between the PBA and MC distributions showed excellent agreement (Figure 3.5). Most of these comparisons yielded 100% of points passing our composite criteria (DTA $\leq$ 1mm or dose difference $\leq$ 2%). The 150 MeV data (Figure 3.5(c)) shows small areas of failure (red pixels near 3% isodose around 15.3 cm depth); however, because the pass rate was greater than 99.95% and all pass rates were rounded to 1 decimal point, this simulation was considered to have a 100% pass rate.

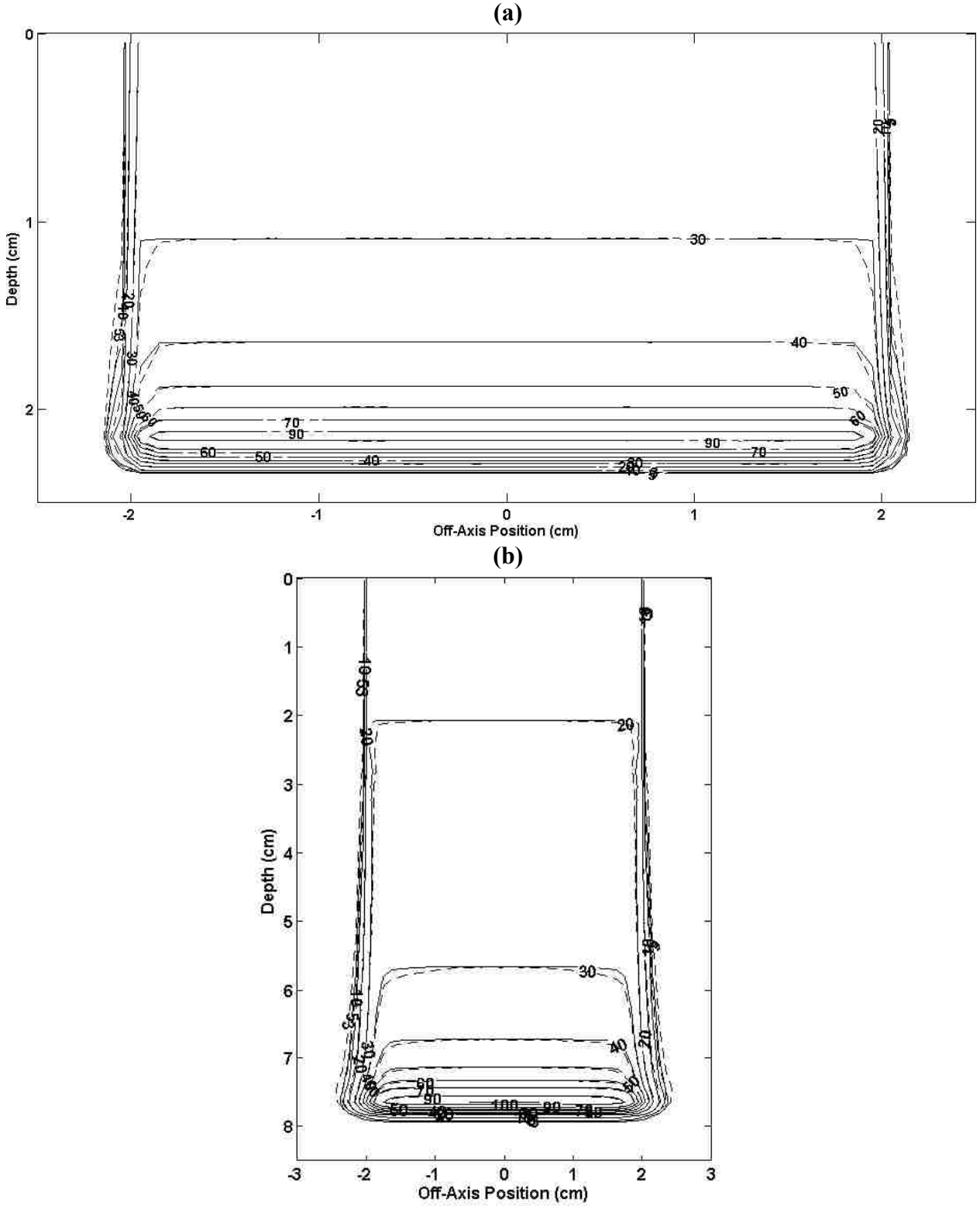

Figure 3.5: Comparisons of isodose lines from the pencil beam algorithm (solid) and Monte Carlo (dashed) calculations for a 4x4 cm^2 field, flat water phantom at incident energies of (a) 50 MeV, (b) 100 MeV, (c) 150 MeV, (d) 200 MeV, and (e) 250 MeV. Isodose values are 100, 90, 70, 60, 50, 40, 30, 20, 10, 5, and 3%. Red areas in the figure, if present, indicate points that did not satisfy DTA $\leq$ 1mm or percent dose difference $\leq$ 2%.

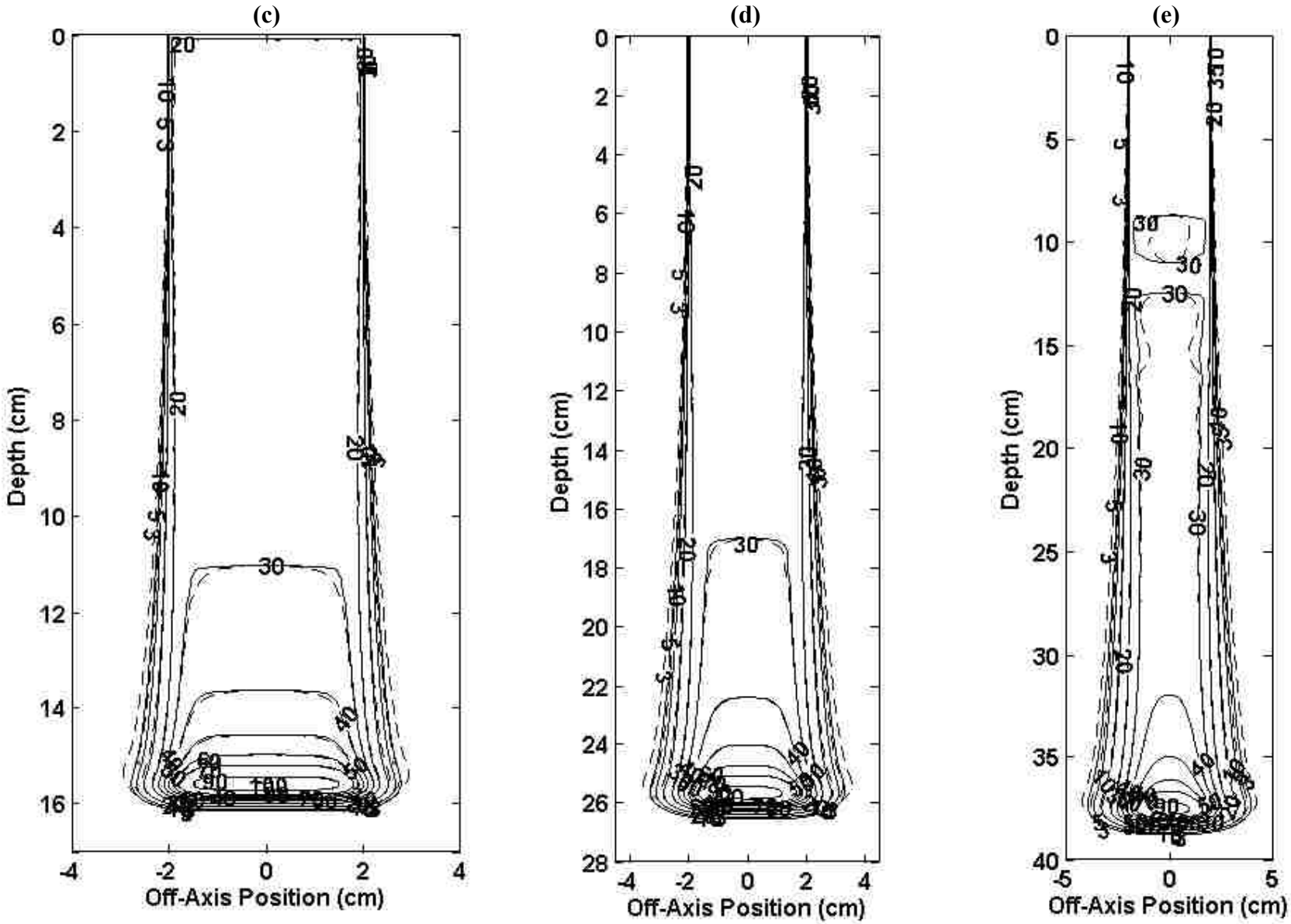

Figure 3.5 (continued)

The 10x10 cm^2 flat phantom results also showed excellent agreement (Figure 3.6). Most comparisons yielded 100% of points passing our composite criteria (DTA ≤ 1mm or dose difference ≤ 2%). The 250 MeV comparison was the only one in the flat phantom simulations that gave less than 100% of passing points (pass rate was 99.9%); failures occurred in the low dose region (~3% isodose line in the lateral penumbra) over a depth range of 11 to 16 cm. These failures were attributed to the modeling limitations of the Gaussians used in our scatter models.

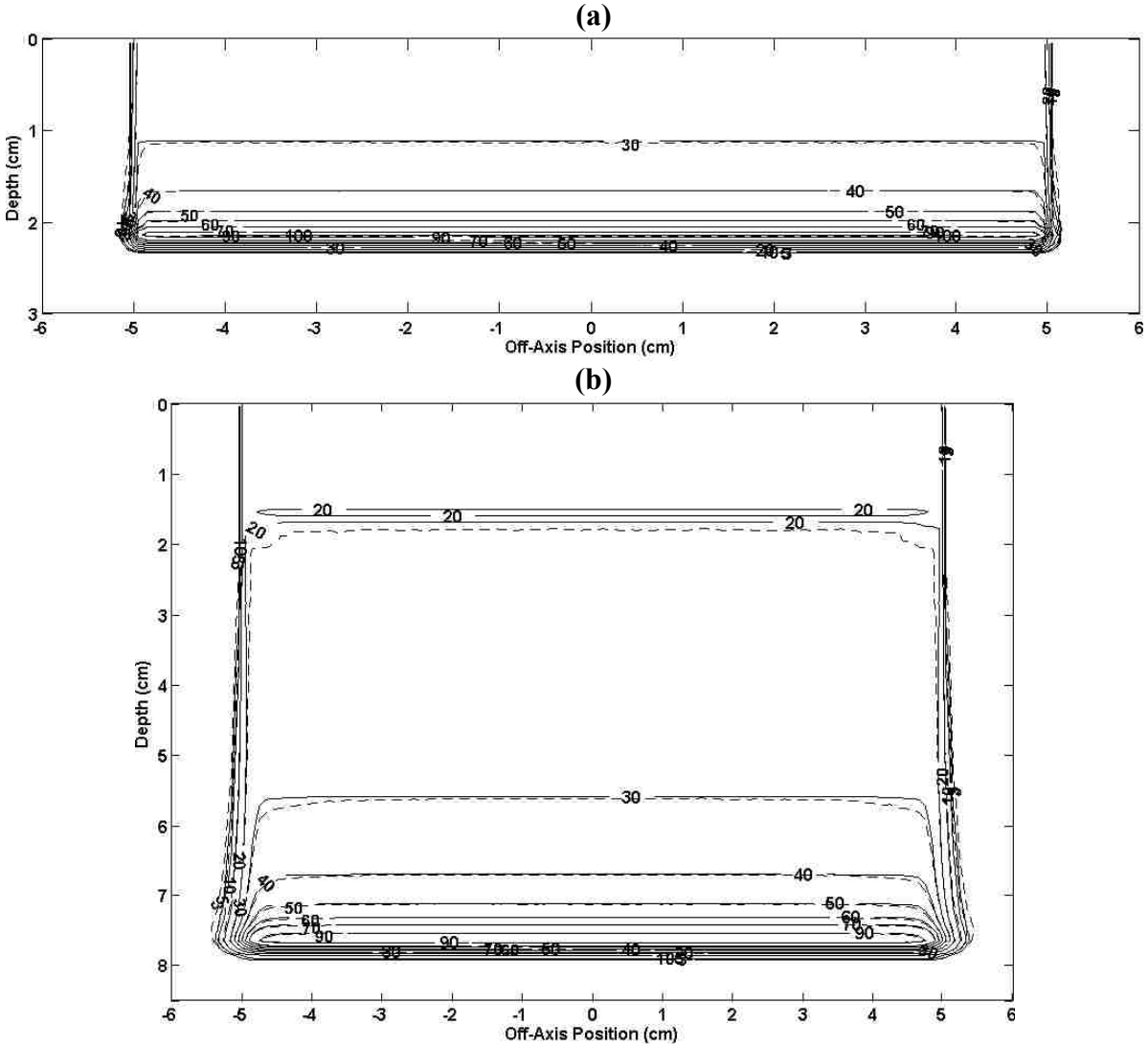

Figure 3.6: Comparisons of isodose lines from the pencil beam algorithm (solid) and Monte Carlo (dashed) calculations for a 10x10 cm^2 field, flat water phantom at incident energies of (a) 50 MeV, (b) 100 MeV, (c) 150 MeV, (d) 200 MeV, and (e) 250 MeV. Isodose values are 100, 90, 70, 60, 50, 40, 30, 20, 10, 5, and 3%. Red areas in the figure, if present, indicate points that did not satisfy DTA ≤ 1mm or percent dose difference ≤ 2%.

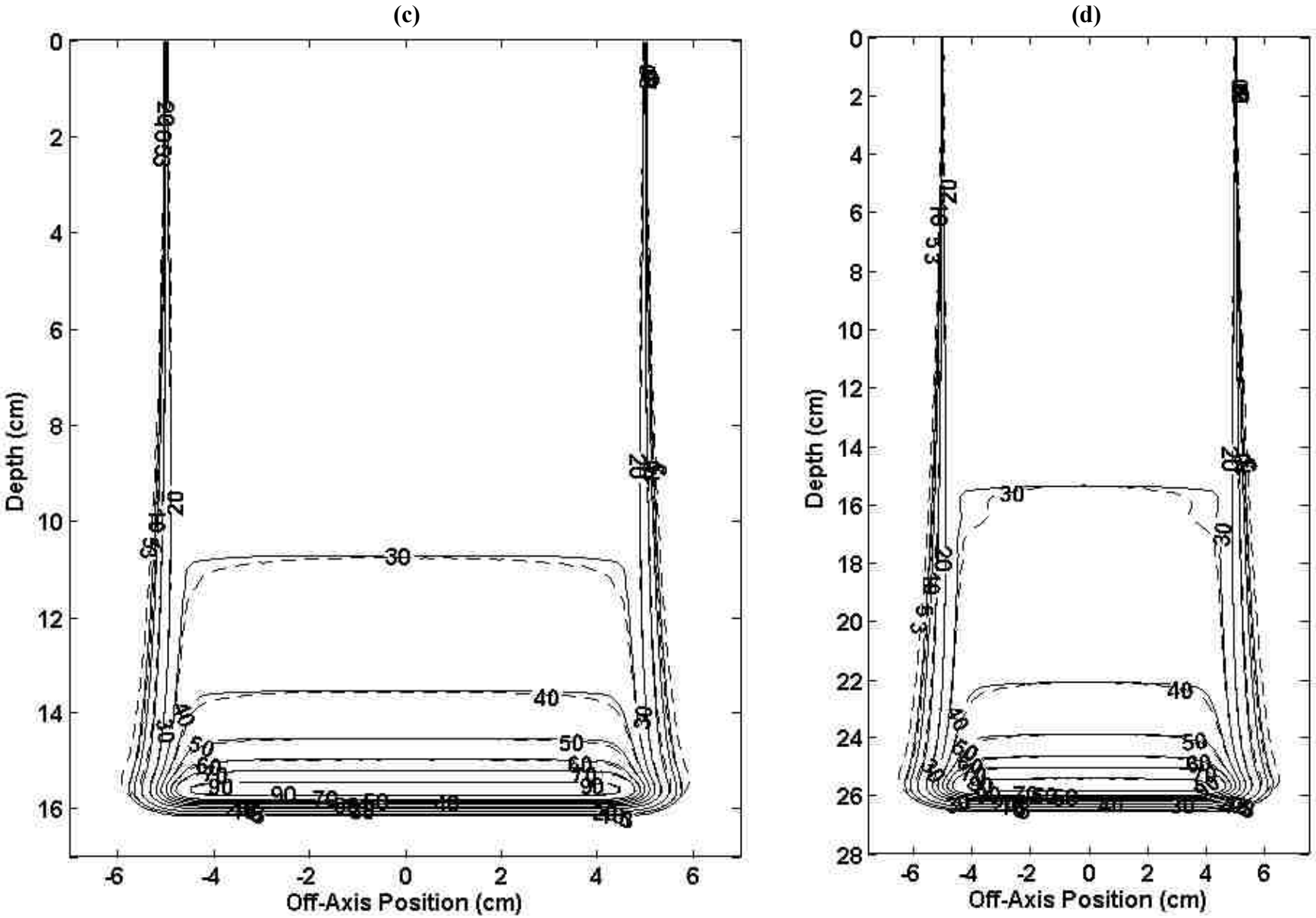

Figure 3.6 (continued)

(e)

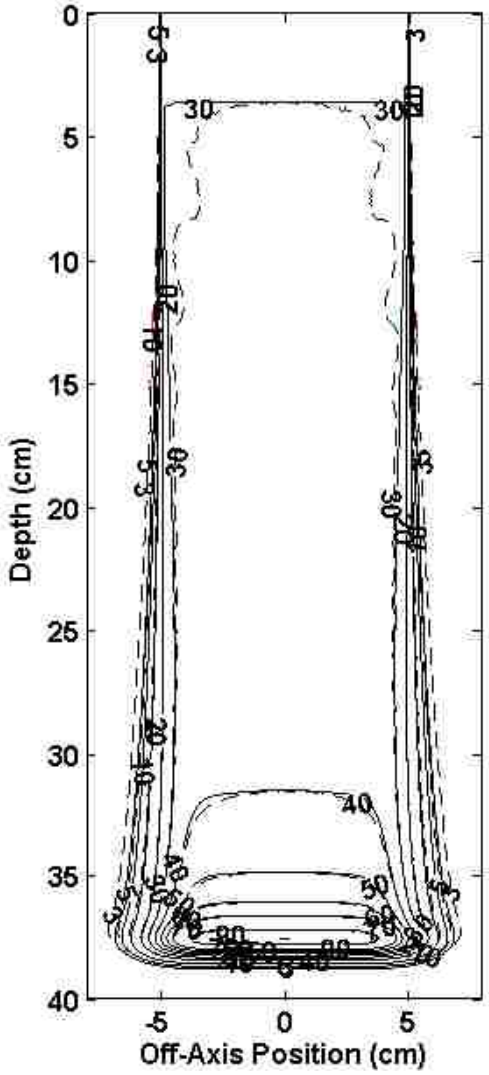

Figure 3.6 (continued)

As discussed in section 1.1.3, Gaussians falloff too rapidly to model the true behavior of large-angle scattering at large distances. Also, the two-Gaussian fit used in our model is too narrow to account for all secondary products from nonelastic nuclear events (see section 3.1). However, most PBAs implement Gaussian-derived pencil beams and the failures seen in this section are well known. To further examine these failures, lateral profiles at the depth of maximum dose and at 80% of the maximum dose depth are taken at energies of 100 and 200 MeV in Figure 3.7. Lateral profiles for the remaining energies (50, 150, and 250 MeV) are shown in Appendix C.

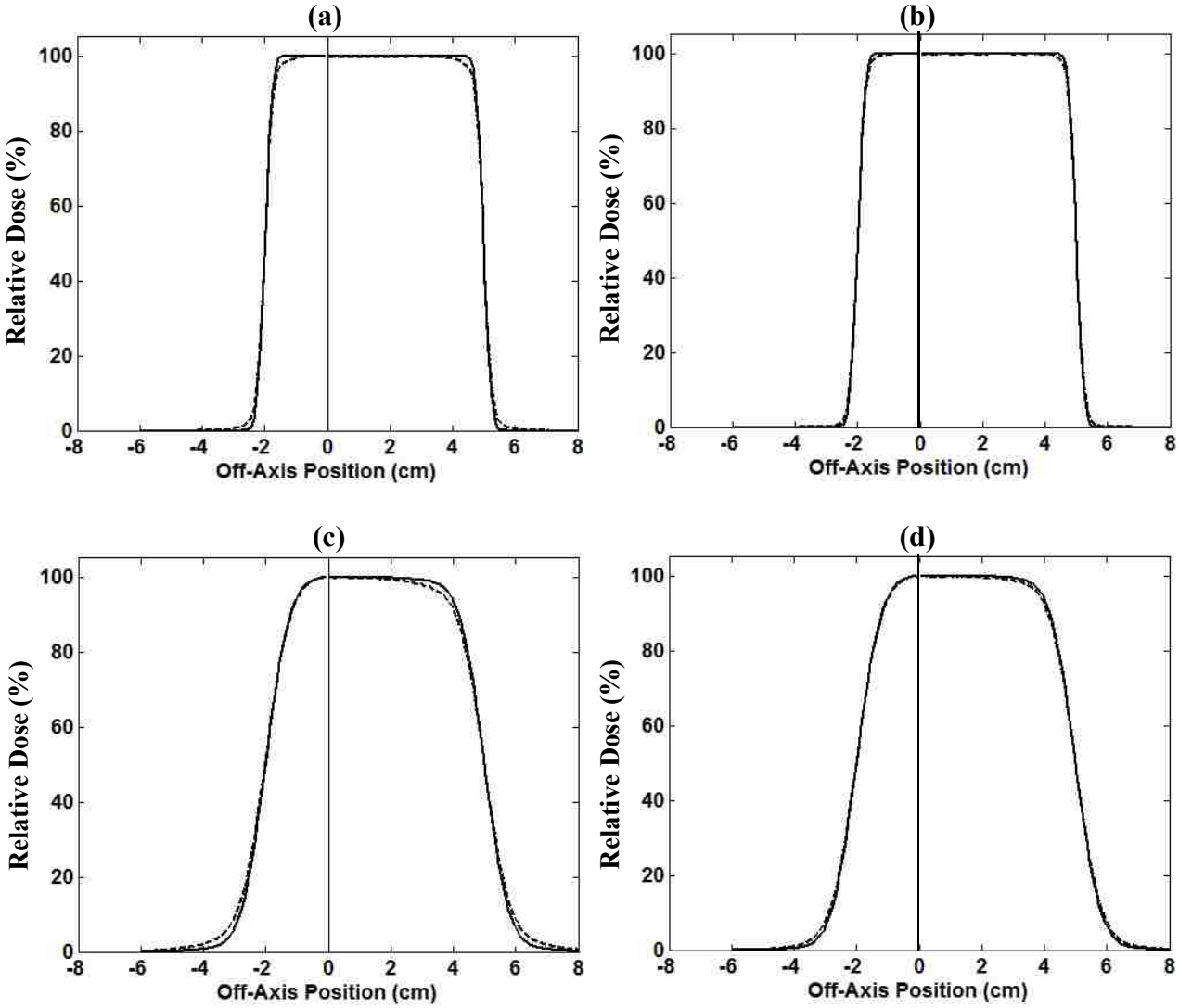

Figure 3.7: Lateral profiles through flat phantom simulations from the pencil beam algorithm (solid) and Monte Carlo data (dashed). All profiles were symmetric about the central-axis; the thin vertical line in (a)-(d) indicates that the profiles shown on the left half of the line are taken through 4x4 cm^2 simulations and the profiles on the right half of the line are taken through 10x10 cm^2 simulations. Profiles are shown for incident energy of 100 MeV at depths of: (a) 80% of the maximum dose, and (b) maximum dose, and for incident energy of 200 MeV at depths of: (c) 80% of the maximum dose, and (d) maximum dose.

In Figure 3.7, the departure of our model from the MC data is evident in that our 20%-80% penumbra is not as broad as the 20%-80% penumbra in the MC data. This effect can be seen to increase with increasing energy and field size, and with decreasing proximal depth to the Bragg peak; these relationships explain why the 250 MeV, 10x10 cm^2 simulation has the worst pass rate of the flat phantom simulations. Despite the limitations imposed by the Gaussians used

in our model, excellent agreement was achieved for both 4x4 cm^2 and 10x10 cm^2 flat phantoms both laterally and in depth; therefore, the PBA accurately accounts for field size dependence in calculating dose.

Central-axis profiles are shown for the flat phantoms at 100 and 200 MeV in Figure 3.8. Central-axis profiles for the remaining energies (50, 150, and 250 MeV) are in Appendix C.

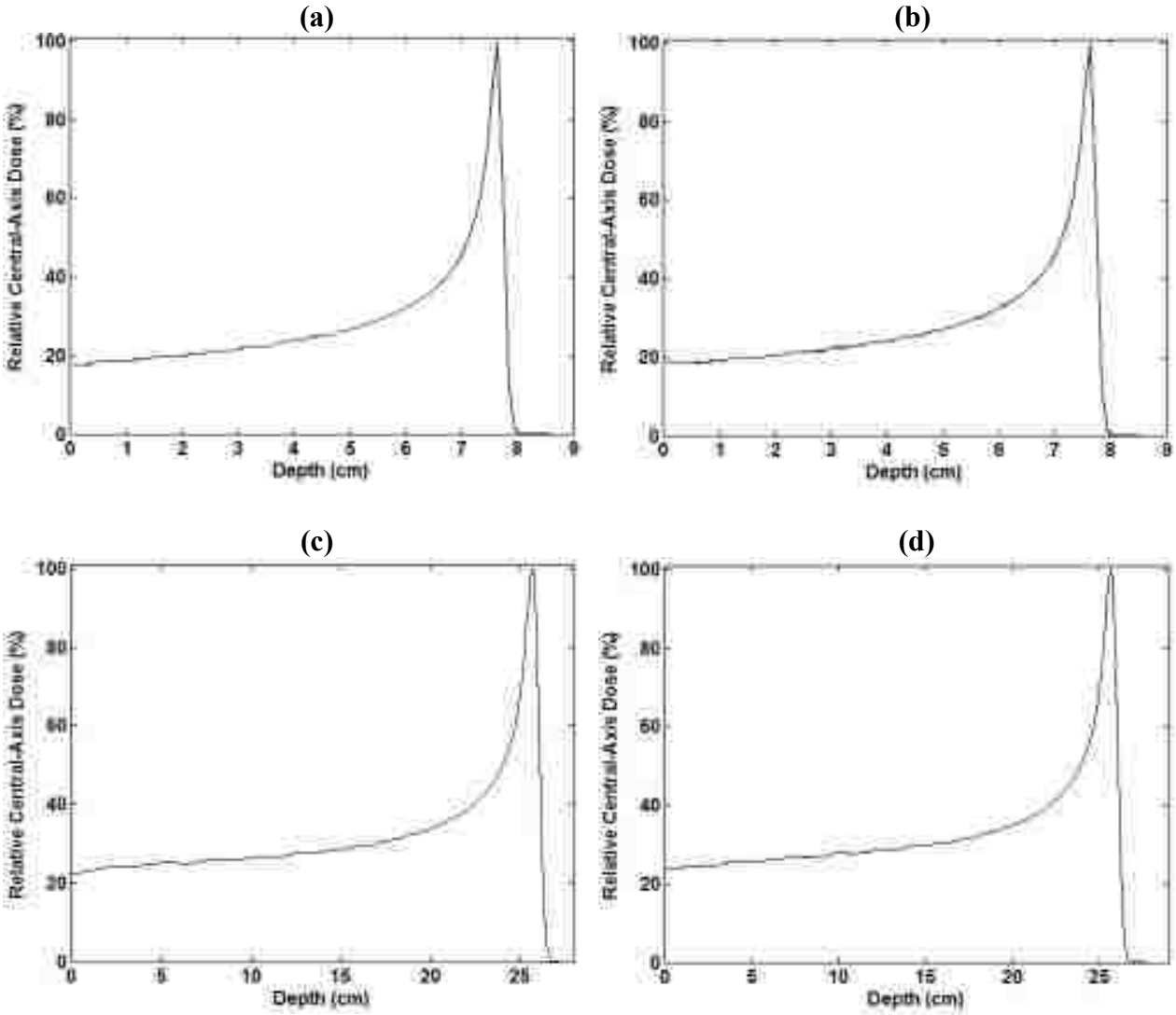

Figure 3.8: Central-axis profiles through flat phantom simulations from the pencil beam algorithm (solid) and Monte Carlo data (dashed). Profiles are shown for (a) 100 MeV, 4x4 cm^2, (b) 100 MeV, 10x10 cm^2, (c) 200 MeV, 4x4 cm^2, and (d) 200 MeV, 10x10 cm^2 simulations. Differences between Monte Carlo and pencil beam algorithm data cannot be seen as all are $\leq$ 0.1cm.

3.2.2 Step Phantoms

The results of the composite analysis on water phantoms with a 1 cm step discontinuity also showed excellent agreement. As in the flat phantom analyses, nearly 100% of all points tested in these phantoms passed our composite criteria (DTA ≤ 1mm or Dose Difference ≤ 2%). The two areas that failed our criteria were: (1) in the low-dose penumbra areas (~3% isodose level) near the end of range (as for the flat surface phantom), and (2) at the surface of the phantom on the "stepped" side (*i.e.,* the positive side of the central-axis, where the source-to-surface distance (SSD) is largest). These failures are evident in both 4x4 cm^2 (Figure 3.9) and 10x10 cm^2 (Figure 3.10) simulations.

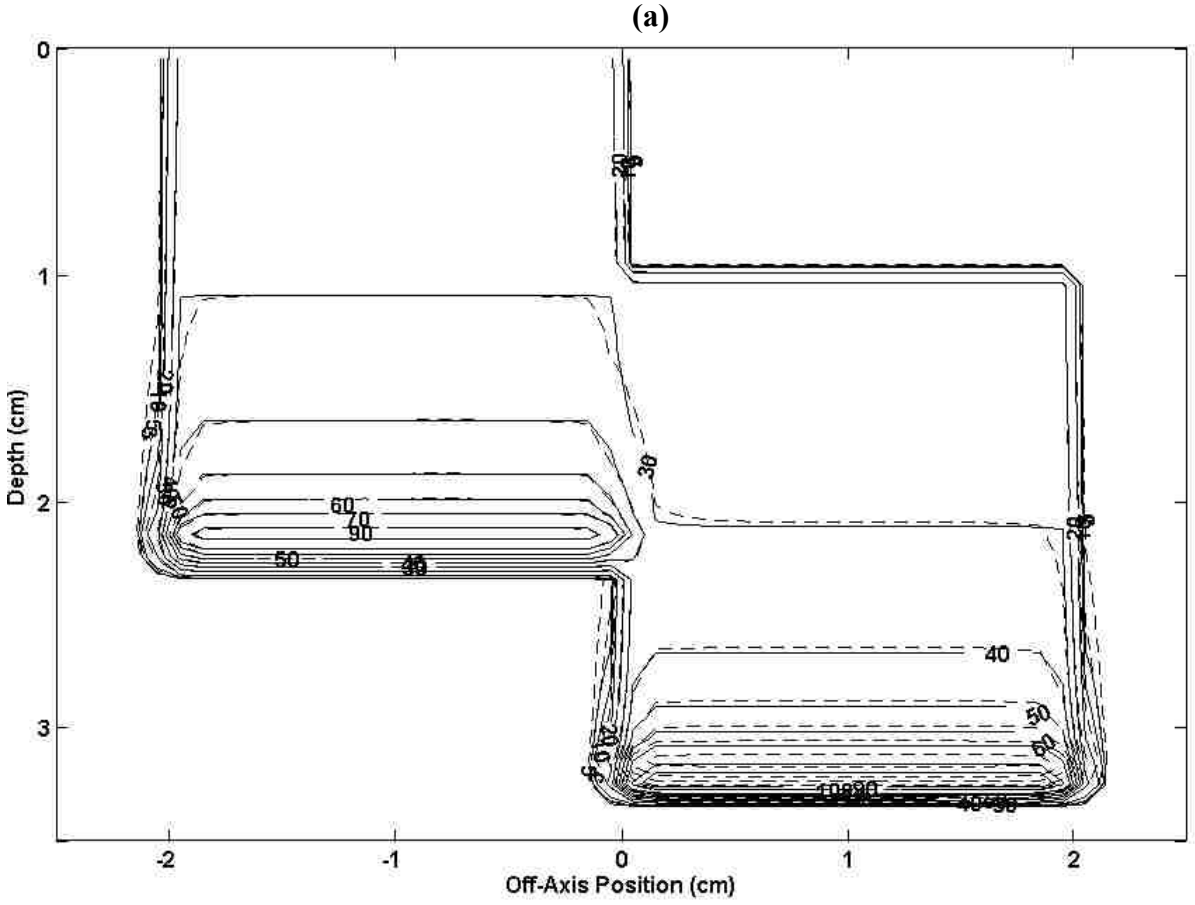

Figure 3.9: Comparisons of isodose lines from the pencil beam algorithm (solid) and Monte Carlo (dashed) calculations for a 4x4 cm^2 field, water phantom with a 1 cm step discontinuity at incident energies of (a) 50 MeV, (b) 100 MeV, (c) 150 MeV, (d) 200 MeV, and (e) 250 MeV. Isodose values are 100, 90, 70, 60, 50, 40, 30, 20, 10, 5, and 3%. Red areas in the figure, if present, indicate points that did not satisfy DTA ≤ 1mm or percent dose difference ≤ 2%.

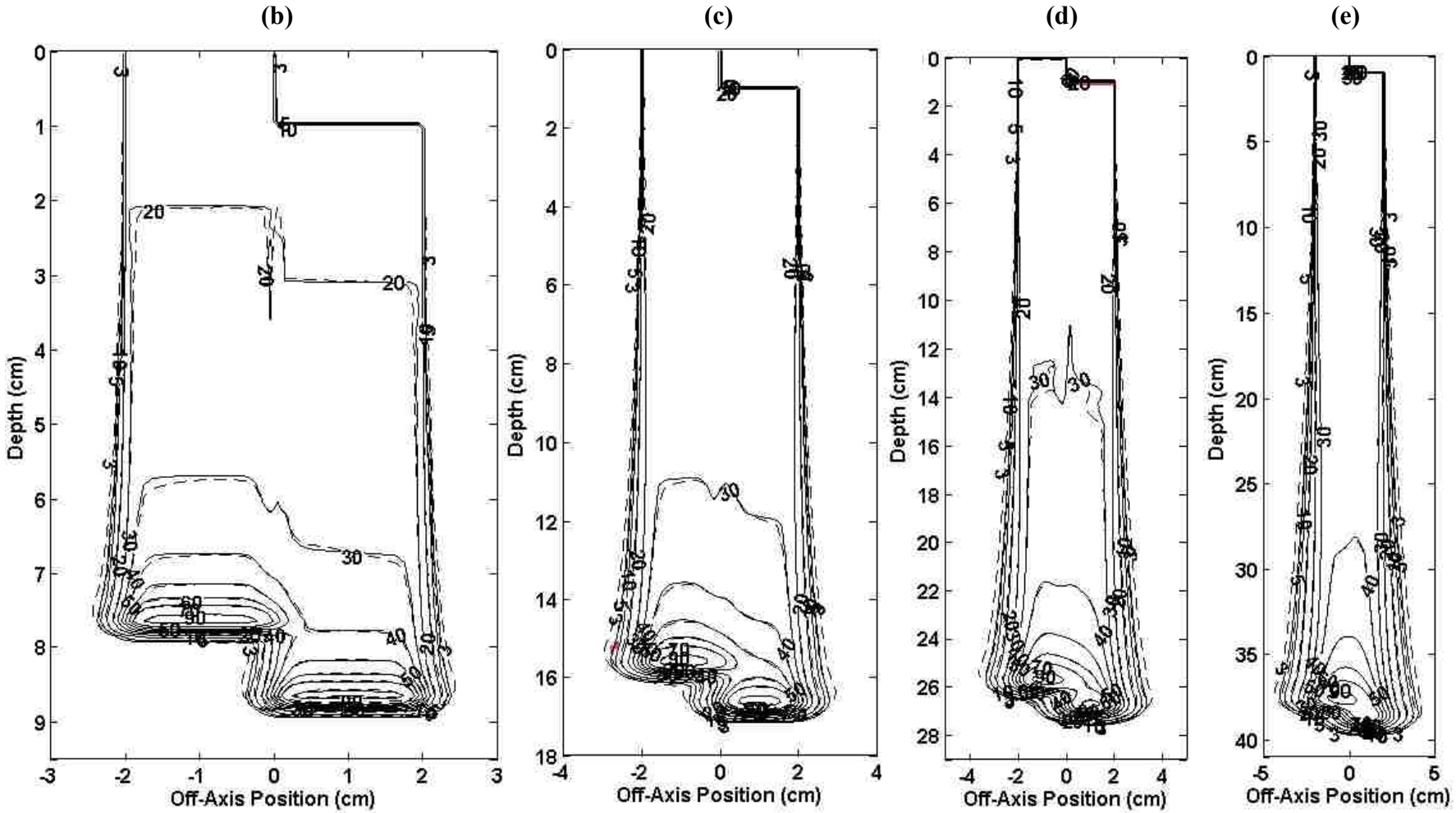

Figure 3.9 (continued)

The step heights tested in this work (1 and 4 cm) are beyond what is typically encountered in clinical situations and the sharp transition along the step is also not usually seen in clinical situations. Thus, the results from these evaluations represent conservatively high estimates of what accuracy might be clinically achievable. The high percentage of passing points (and corresponding small volume failing) for all step evaluations suggests that the PBA accurately accounts for surface irregularities.

Figure 3.10 shows the 10x10 cm^2 results for the simulations with a 1 cm step along the surface of a water phantom. Results were similar to the 4x4 cm^2 simulations and failures occurred in essentially the same areas. It is interesting to note that failures for the 250 MeV simulations (Figure 3.10(e)) occur in the same areas discussed for the 250 MeV, 10x10 cm^2 flat phantom simulations; however, the failure in Figure 3.10(e) is oriented towards the positive side of the central-axis because of the central-axis semi-infinite slab approximation used in the PBA.

When the step height of the phantom was increased to 4 cm, the percentage of passing points decreased slightly, from nearly 100% for the 1 cm step results to values ranging from 99.2% to 100% for the 4 cm step results (although most 4 cm step results had values of 99.8%, 99.9% or 100%). The same failures described for the 1 cm step phantom were observed for these simulations, with additional failures directly under (*e.g.,* Figure 3.11(b) and 3.12(b)) or adjacent to the step transition (*e.g.,* Figure 3.11(a) and 3.12(a)). These additional failures were observed because scatter contributions from the flat side of the phantom to the stepped side of the phantom were not adequately modeled by the PBA, believed a direct result of the central-axis approximation applied to pencil beams.

The lowest pass rate for the step phantoms occurred for the 50 MeV, 10x10 cm^2 results (99.2% pass rate). It is clear from Figures 3.11(a) and 3.12(a) (these have been enlarged to

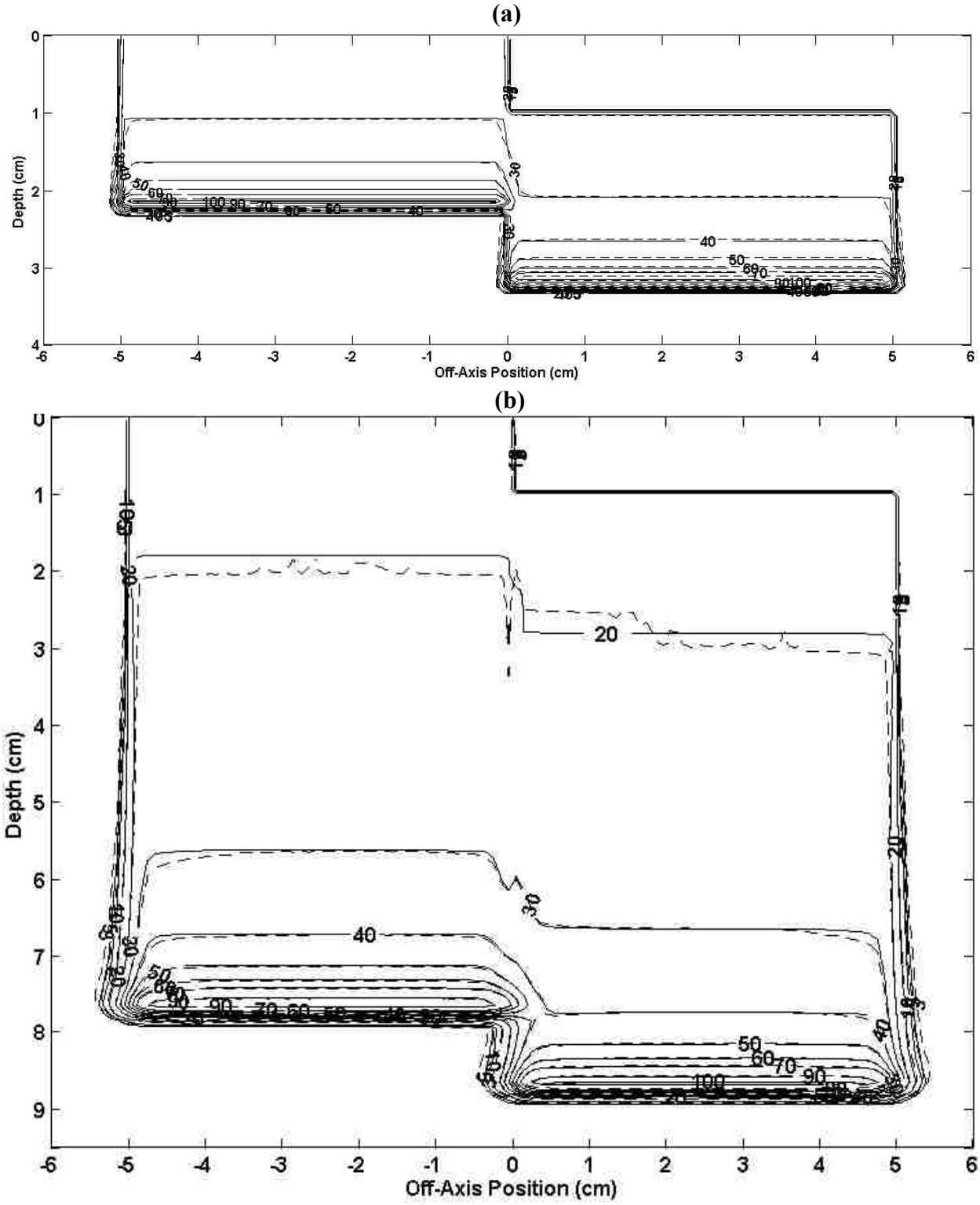

Figure 3.10: Comparisons of isodose lines from the pencil beam algorithm (solid) and Monte Carlo (dashed) calculations for a 10x10 cm^2 field, water phantom with a 1 cm step discontinuity at incident energies of (a) 50 MeV, (b) 100 MeV, (c) 150 MeV, (d) 200 MeV, and (e) 250 MeV. Isodose values are 100, 90, 70, 60, 50, 40, 30, 20, 10, 5, and 3%. Red areas in the figure, if present, indicate points that did not satisfy DTA $\leq$ 1mm or percent dose difference $\leq$ 2%.

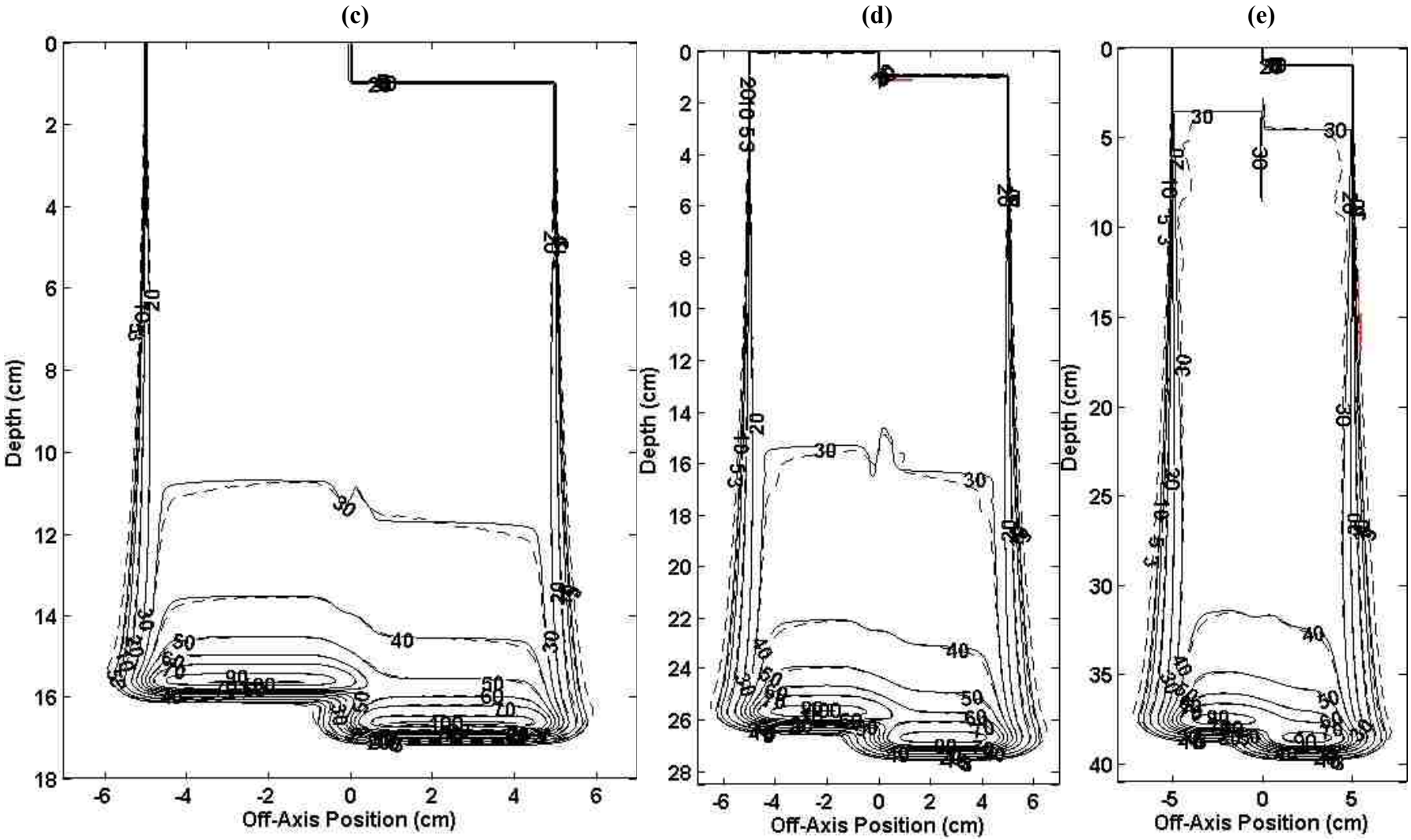

Figure 3.10 (continued)

emphasize failures) that scatter contributions predicted by MC are underestimated by the PBA due to the central-axis approximation of pencil beams (red area near x = 0.2 cm). Further, because a 50 MeV beam has such a short range (~2.2 cm in water), the number of pixels within the 1% isodose line (recall our 1% dose threshold) are fewer than for other energies; thus, even a small number of failing pixels will be amplified by the small number of total pixels.

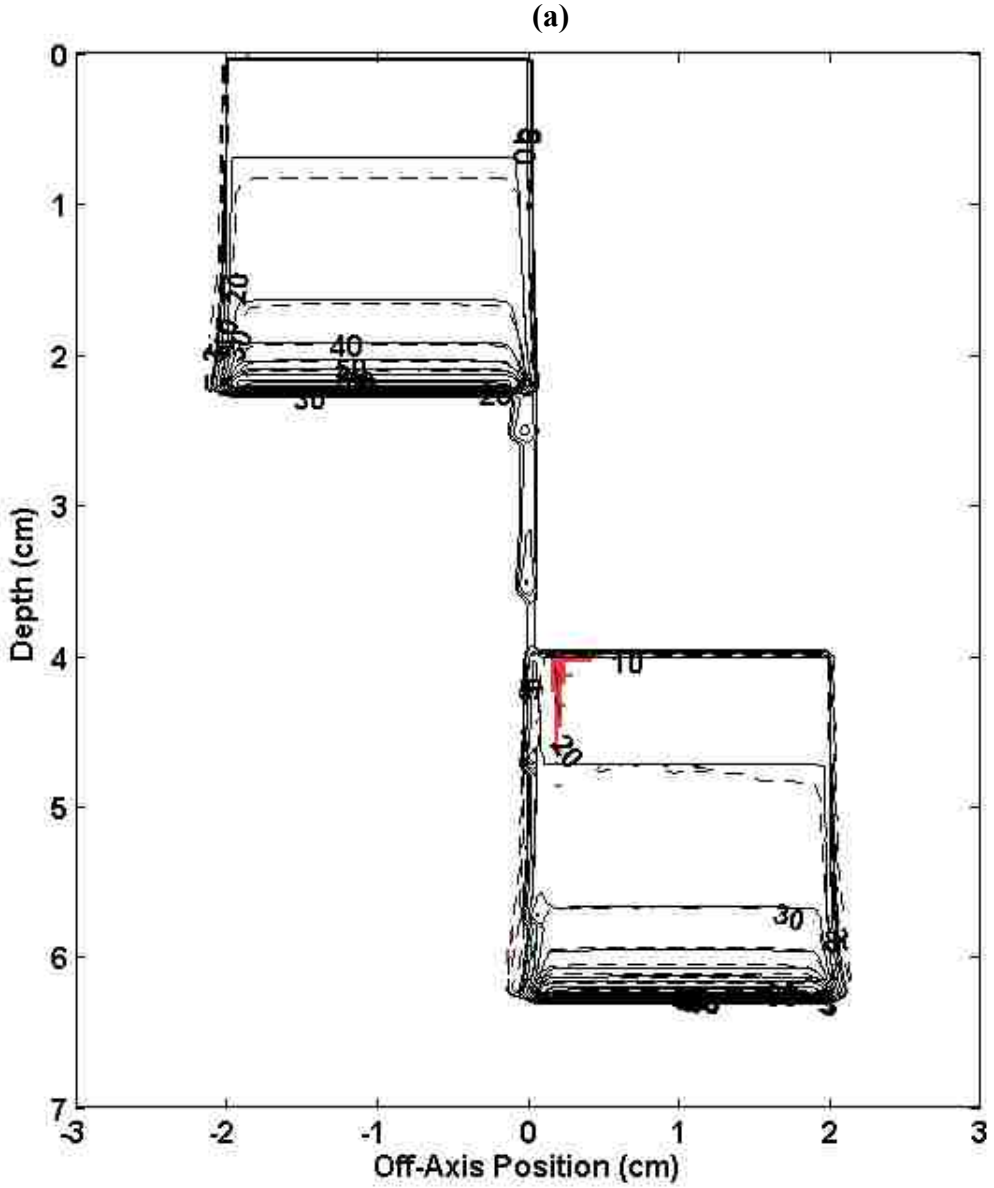

Figure 3.11: Comparisons of isodose lines from the pencil beam algorithm (solid) and Monte Carlo (dashed) calculations for a 4x4 cm^2 field, water phantom with a 4 cm step discontinuity at incident energies of (a) 50 MeV, (b) 100 MeV, (c) 150 MeV, (d) 200 MeV, and (e) 250 MeV. Isodose values are 100, 90, 70, 60, 50, 40, 30, 20, 10, 5, and 3%. Red areas in the figure, if present, indicate points that did not satisfy DTA $\leq$ 1mm or percent dose difference $\leq$ 2%.

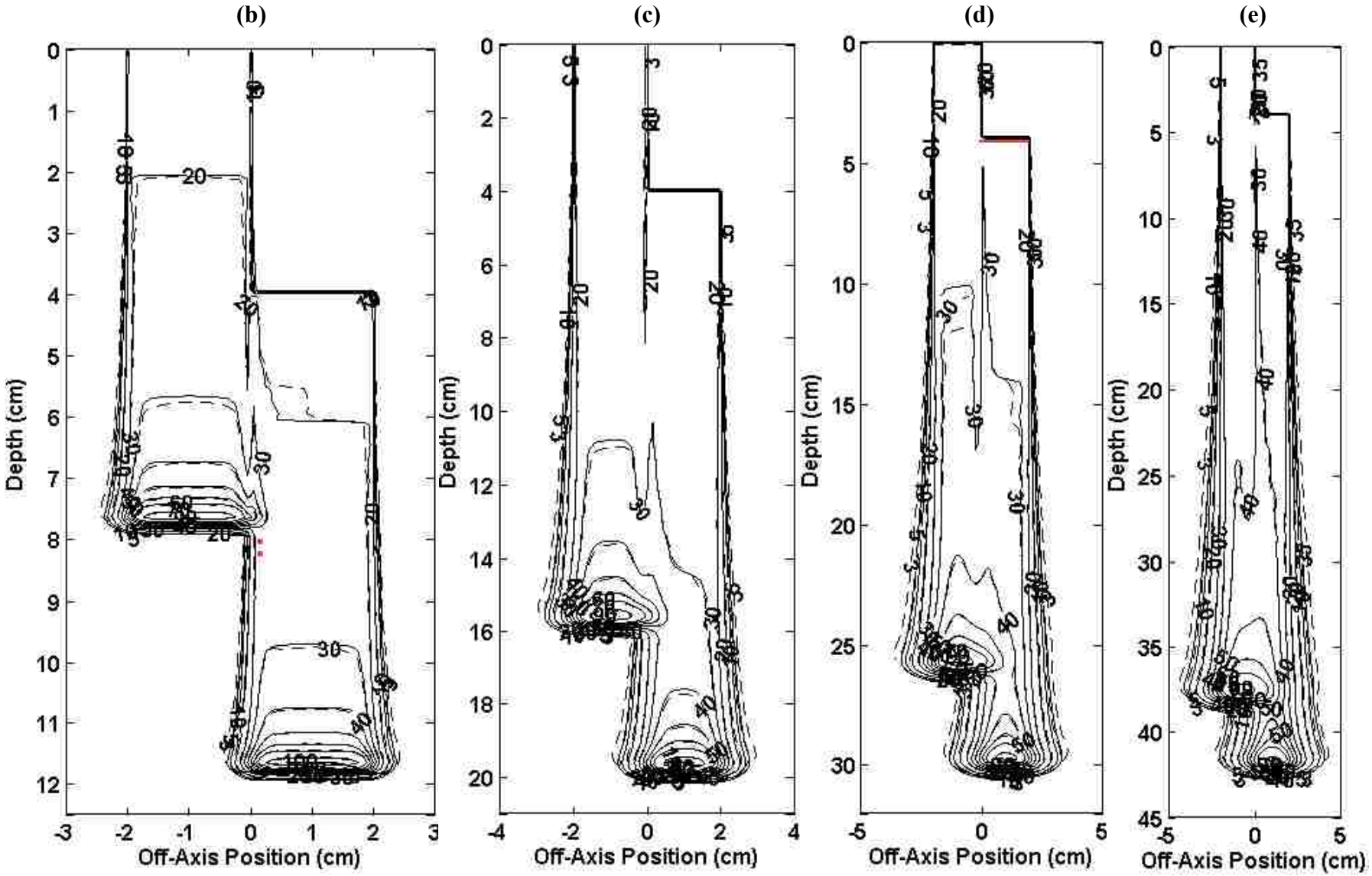

Figure 3.11 (continued)

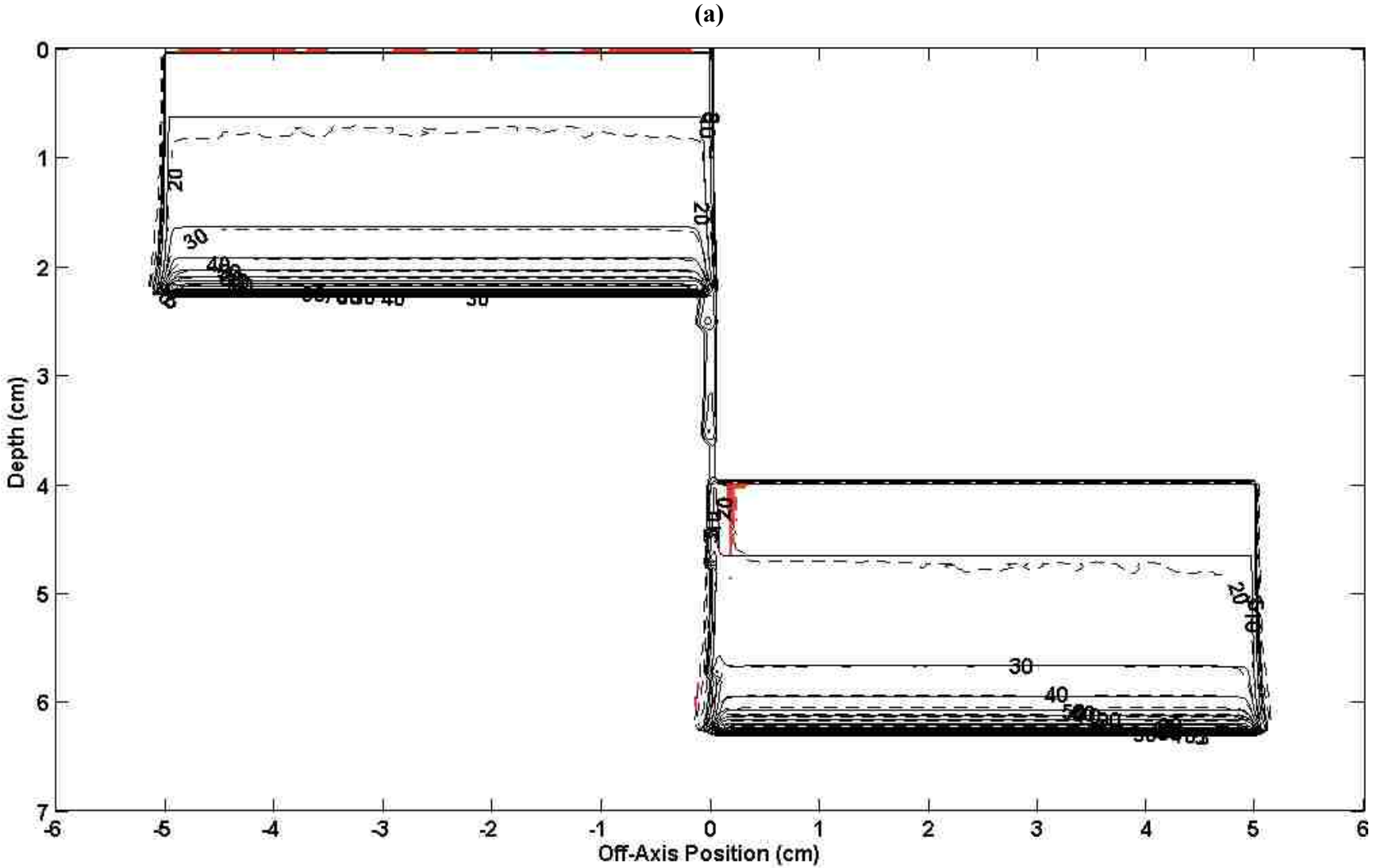

Figure 3.12: Comparisons of isodose lines from the pencil beam algorithm (solid) and Monte Carlo (dashed) calculations for a 10x10 cm^2 field, water phantom with a 4 cm step discontinuity at incident energies of (a) 50 MeV, (b) 100 MeV, (c) 150 MeV, (d) 200 MeV, and (e) 250 MeV. Isodose values are 100, 90, 70, 60, 50, 40, 30, 20, 10, 5, and 3%. Red areas in the figure, if present, indicate points that did not satisfy DTA $\leq$ 1mm or percent dose difference $\leq$ 2%.

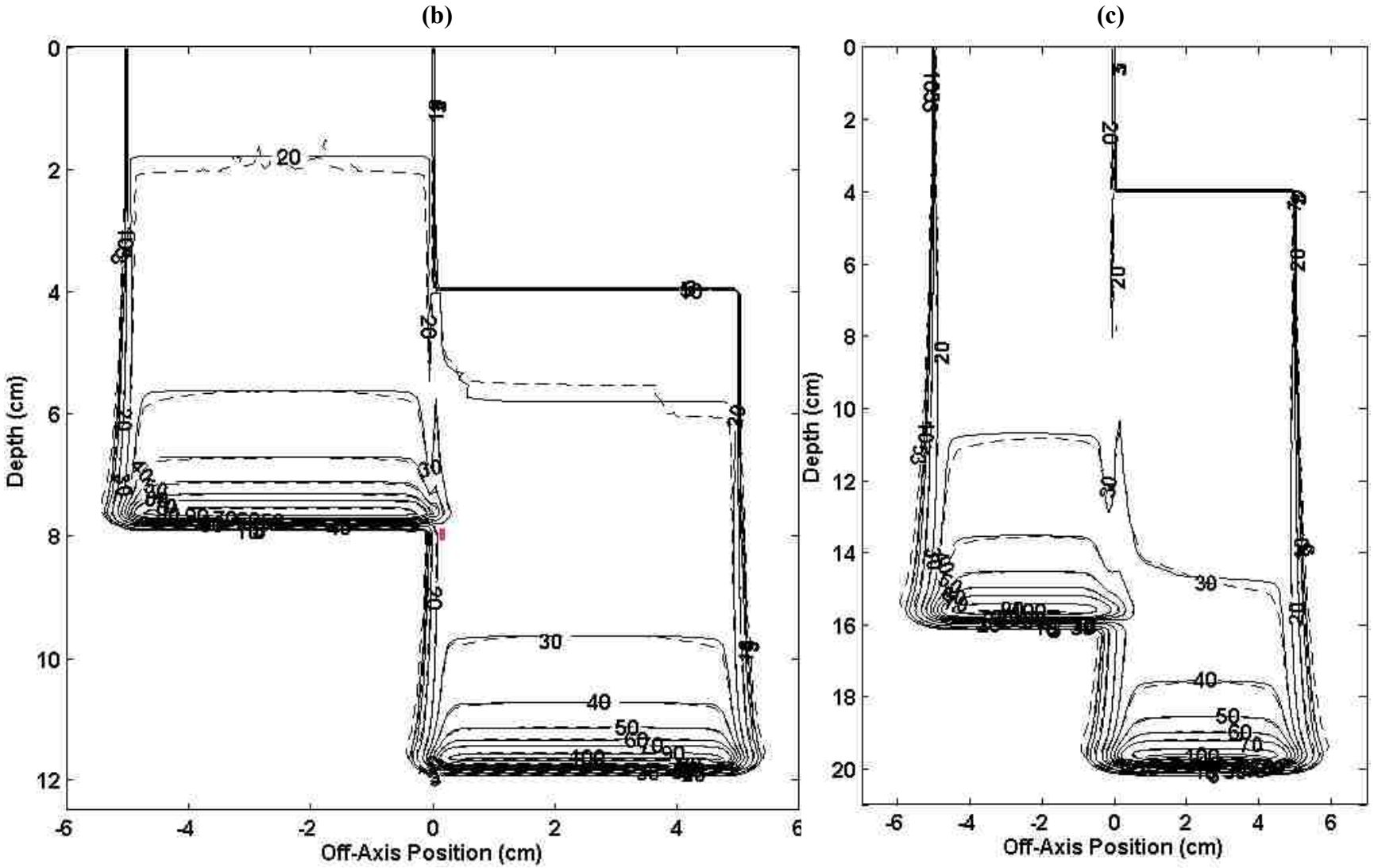

Figure 3.12 (continued)

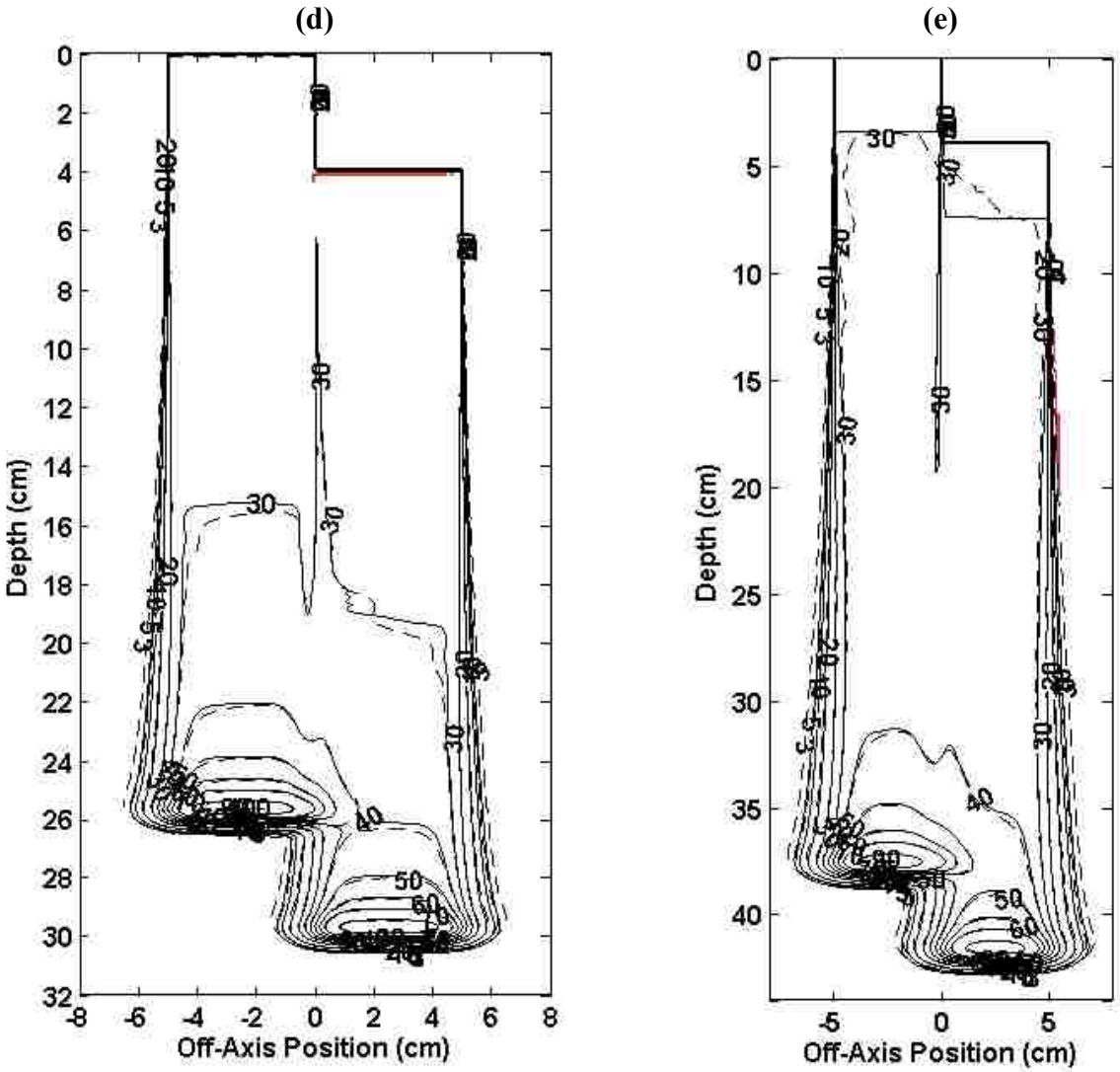

Figure 3.12 (continued)

Lateral profiles through step phantom data at 4.2 cm and 7.2 cm depth were compared for 100 MeV and 200 MeV beams. These depths were chosen because they correspond to 3.2 cm below phantoms with 1 cm and 4 cm step heights, and the 4.2 cm depth is directly below a 4 cm step height. These lateral profile comparisons were performed for both 4x4 cm^2 and 10x10 cm^2 fields.

The 100 MeV data is shown for 4x4 cm^2 fields in Figure 3.13 and for 10x10 cm^2 fields in Figure 3.14 while the 200 MeV data is shown for 4x4 cm^2 fields in Figure 3.15 and for 10x10 cm^2 fields in Figure 3.16. In all four of these figures, the lateral profiles were normalized to the

MC maximum in the lateral profile. Interface dose effects (*i.e.*, the hot and cold spots evident near the central-axis) were predicted well by all of these comparisons – except for the profiles taken at 4.2 cm depth for the 200 MeV, 4 cm step profile (from Figures 3.11(d) and 3.12(d), it is evident that these profiles were taken through areas that did not pass our DTA ≤ 1mm or dose difference ≤ 2% criteria.

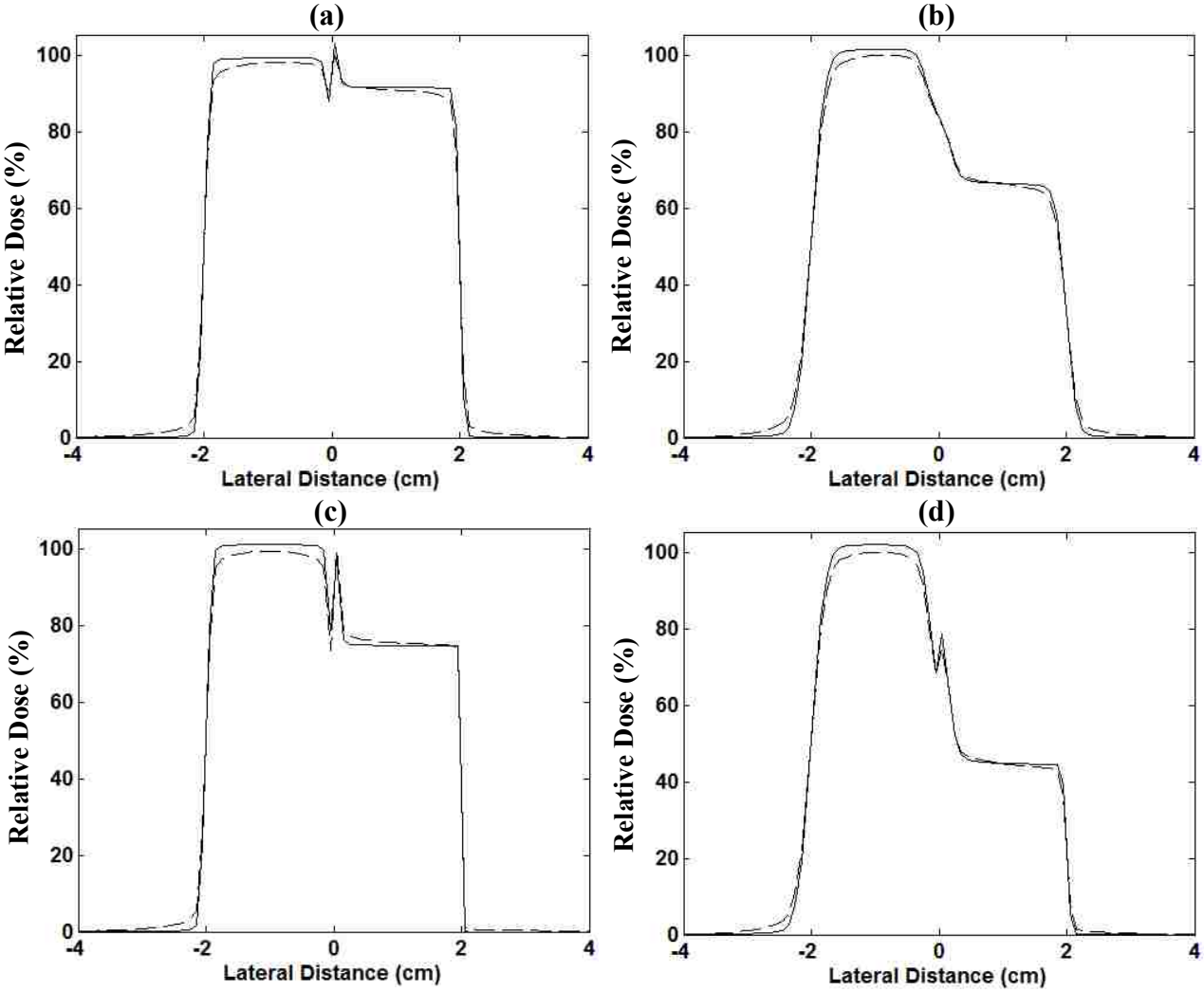

Figure 3.13: Lateral profiles for a 100 MeV beam with a 4x4 cm^2 field size at depths of 4.2 cm (a,c) and 7.2 cm (b,d). In (a) and (b), the step height was 1 cm, and in (c) and (d), the step height was 4 cm.

It can be seen in these profiles that interface effects were modeled appropriately with increasing depth from the step irregularity. The PBA and MC data agreed well for depths of 4.2 and 7.2 cm. In general, this agreement worsened with 4 cm step height comparisons relative to

those with 1 cm height; however, for both the 1 cm and the 4 cm step height comparisons, the agreement improved with increasing depth from the step irregularity. All of these effects are consistent with the limitations imposed by the central-axis approximation of pencil beams.

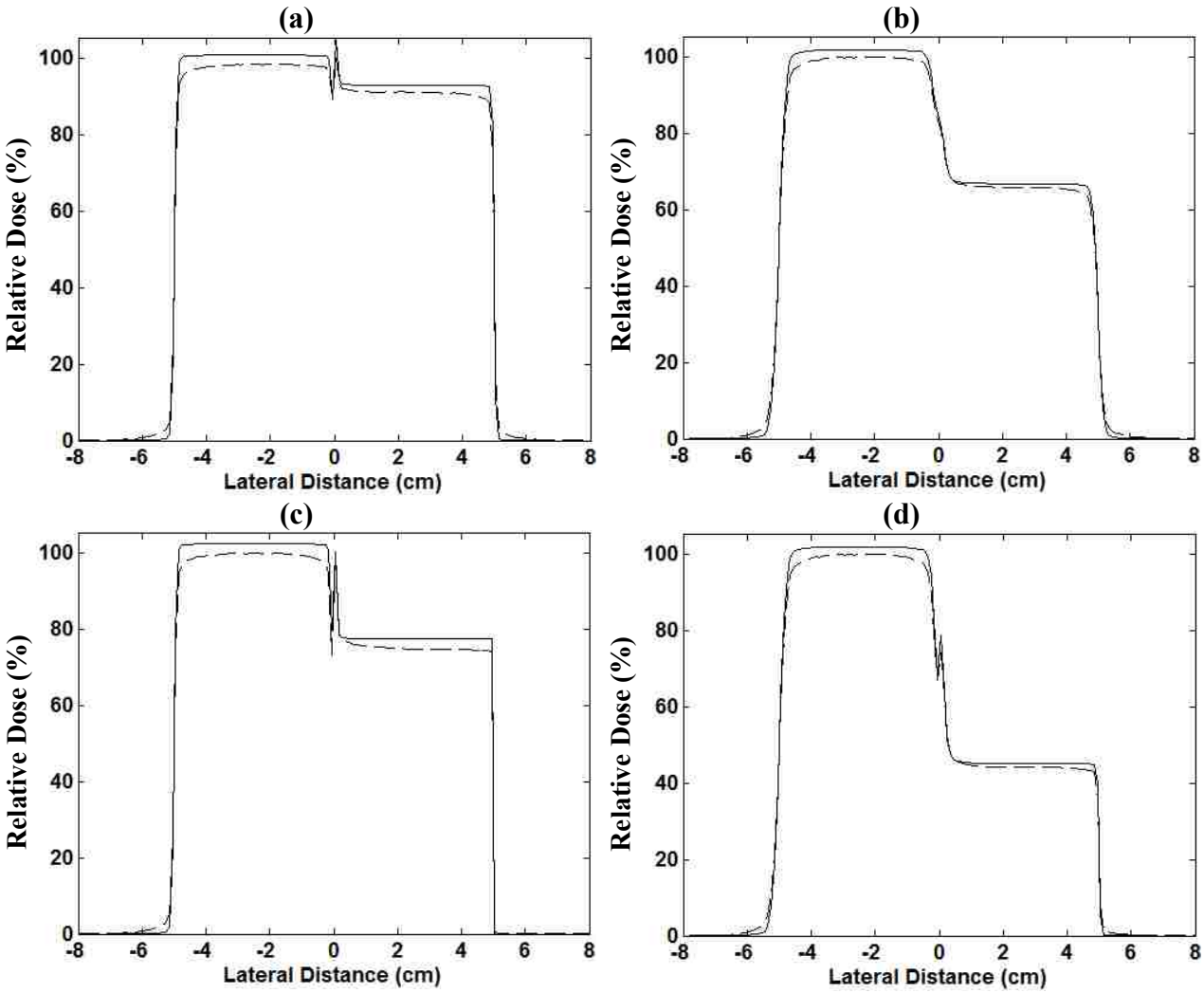

Figure 3.14: Lateral profiles for a 100 MeV beam with a 10x10 cm^2 field size at depths of 4.2 cm (a,c) and 7.2 cm (b,d). In (a) and (b), the step height was 1 cm, and in (c) and (d), the step height was 4 cm.

Comparing Figure 3.13 to Figure 3.14 and Figure 3.15 to Figure 3.16, it is evident that there is little field size dependence on the effects seen in these lateral profiles. It is apparent from many of these profiles that hot and cold spots of dose are created in the center of the field (at the vacuum-water interface). The central-axis approximation applied to pencil beams immediately in the vicinity of this interface is the major cause of these perturbations, so it is not

surprising that an increase in field size (with a corresponding increase in pencil beams) has little influence on interface effects.

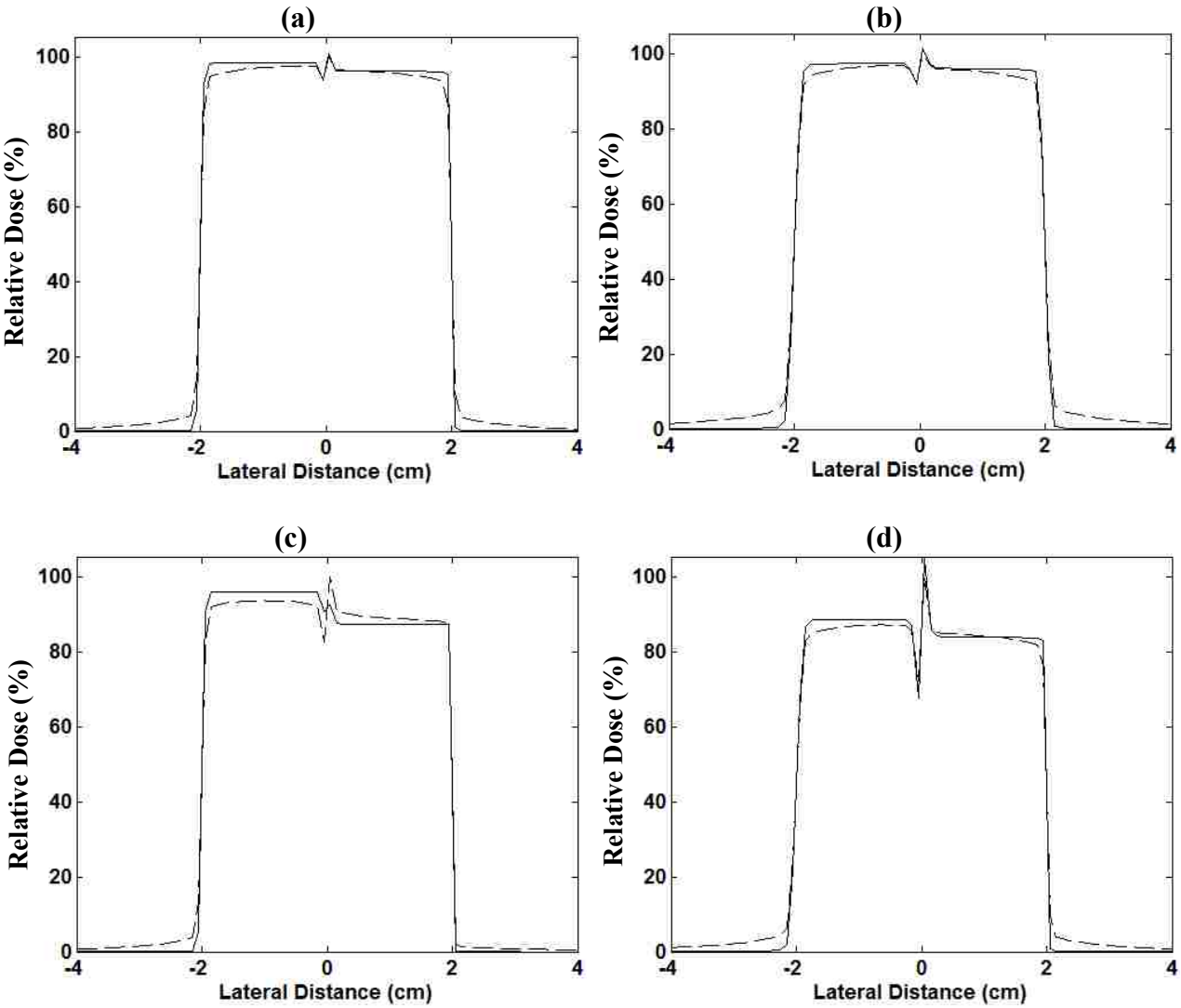

Figure 3.15: Lateral profiles for a 200 MeV beam with a 4x4 cm^2 field size at depths of 4.2 cm (a,c) and 7.2 cm (b,d). In (a) and (b), the step height was 1 cm, and in (c) and (d), the step height was 4 cm.

3.2.3 Oblique Phantom

For the comparisons using phantoms with oblique surfaces tilted relative to the beam (45 degrees), agreement was again very good. The 50 MeV, 4x4 cm^2 field size simulation showed the lowest percentage of passing points with a 99% pass rate (Figure 3.17(a)). Upon closer inspection, it can be seen that these failures only occur on the first row of pixels, an artifact of

finite pencil beam width. Also, the lower pass rate for this simulation can again be attributed to the distribution having fewer pixels than the other distributions. In a larger phantom, there would be more pixels and a failing top row of pixels would not markedly influence the total percentage of passing points. The 4x4 cm^2 data is shown in Figure 3.17.

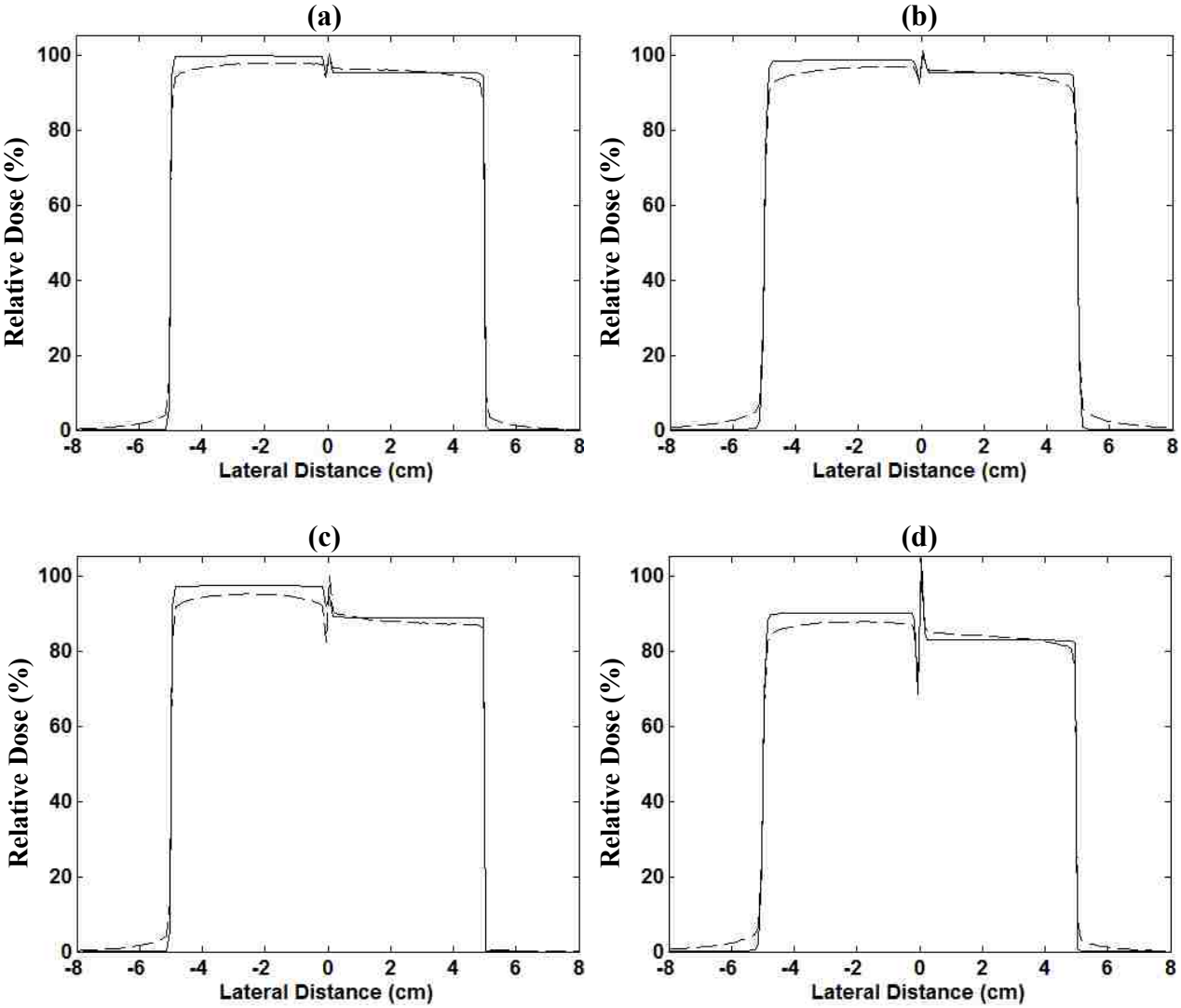

Figure 3.16: Lateral profiles for a 200 MeV beam with a 10x10 cm^2 field size at depths of 4.2 cm (a,c) and 7.2 cm (b,d). In (a) and (b), the step height was 1 cm, and in (c) and (d), the step height was 4 cm.

The failures that are seen in the high energy simulations occur in low dose regions beyond the penumbra, or in the high dose region near the Bragg peak. For the latter of these failures, there is a tendency for them to occur on the negative side of the central-axis (largest

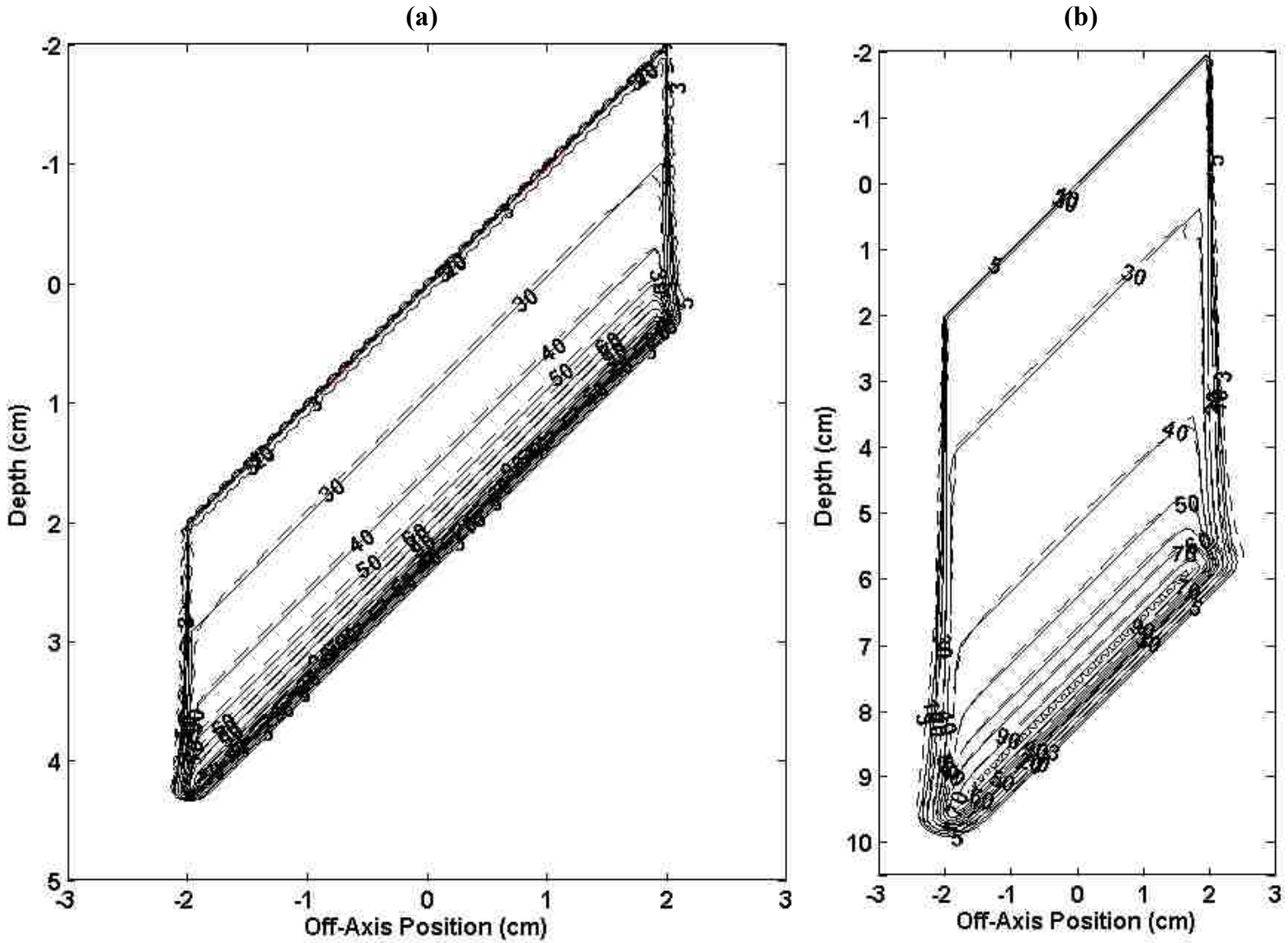

Figure 3.17: Comparisons of isodose lines from the pencil beam algorithm (solid) and Monte Carlo (dashed) calculations for a 4x4 cm^2 field, water phantom with a surface tilted 45 degrees to the direction of the beam for incident energies of (a) 50 MeV, (b) 100 MeV, (c) 150 MeV, (d) 200 MeV, and (e) 250 MeV. Isodose values are 100, 90, 70, 60, 50, 40, 30, 20, 10, 5, and 3%. Red areas in the figure, if present, indicate points that did not satisfy DTA $\leq$ 1mm or percent dose difference $\leq$ 2%

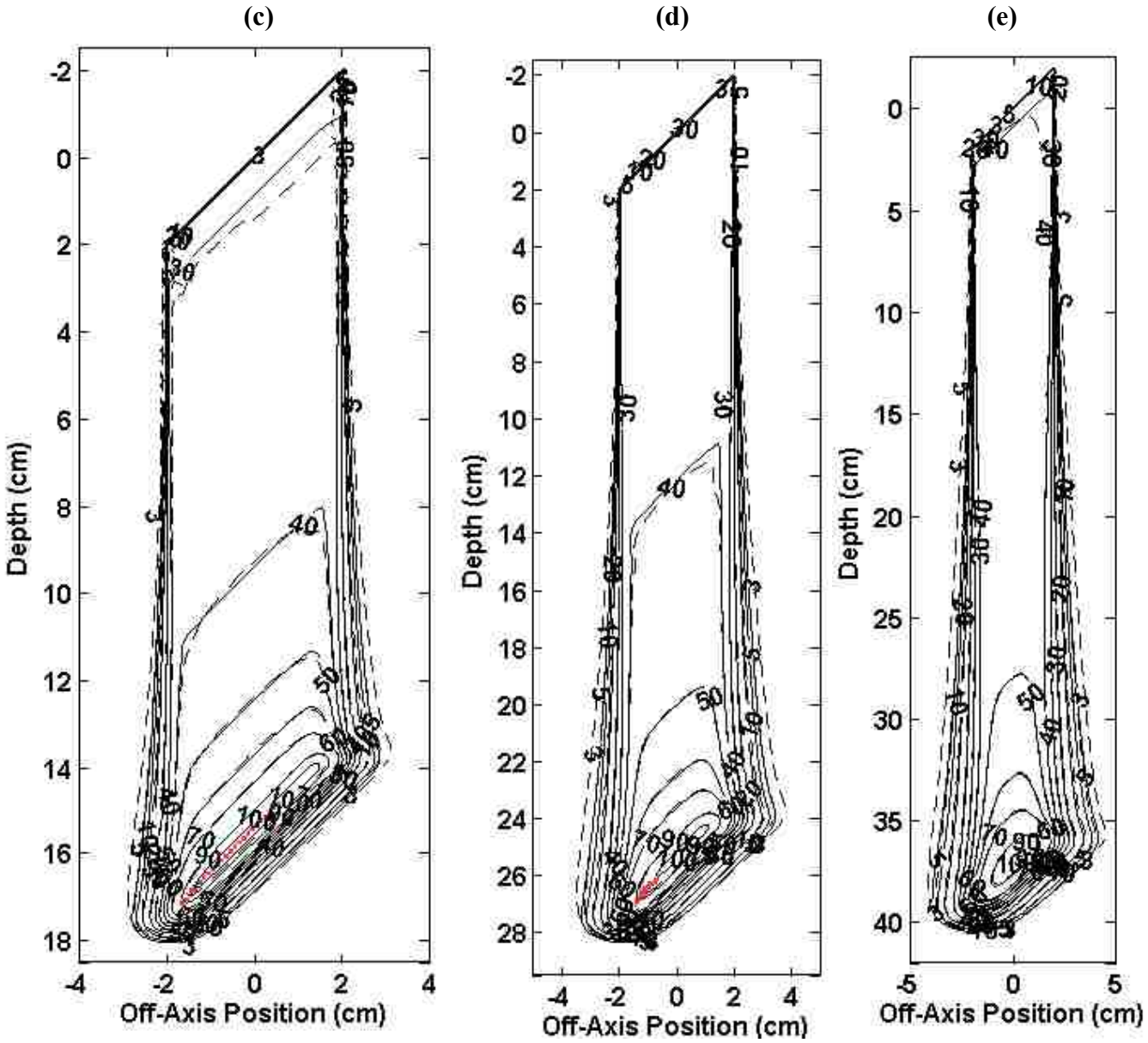

Figure 3.17 (continued)

source-to-surface distance (SSD)). These failures increase with increasing field size, and are most noticeable in the 10x10 cm^2 simulations (Figure 3.18). This effect is due to the loss of side-scatter equilibrium, which will be explained in further detail in the following paragraph.

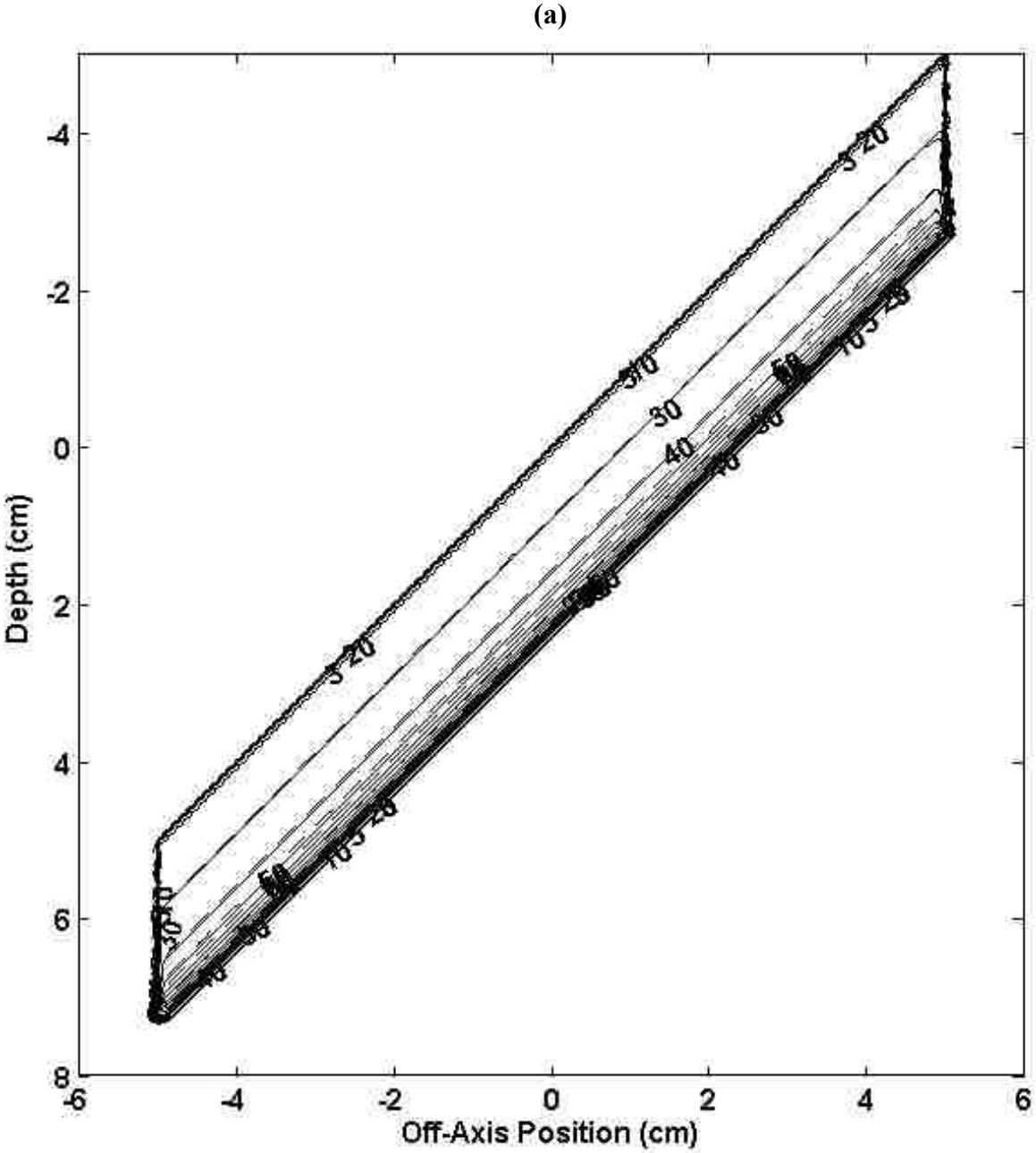

Figure 3.18: Comparisons of isodose lines from the pencil beam algorithm (solid) and Monte Carlo (dashed) calculations for a 10x10 cm^2 field, water phantom with a surface tilted 45 degrees to the direction of the beam for incident energies of (a) 50 MeV, (b) 100 MeV, (c) 150 MeV, (d) 200 MeV, and (e) 250 MeV. Isodose values are 100, 90, 70, 60, 50, 40, 30, 20, 10, 5, and 3%. Red areas in the figure, if present, indicate points that did not satisfy DTA $\leq$ 1mm or percent dose difference $\leq$ 2%.

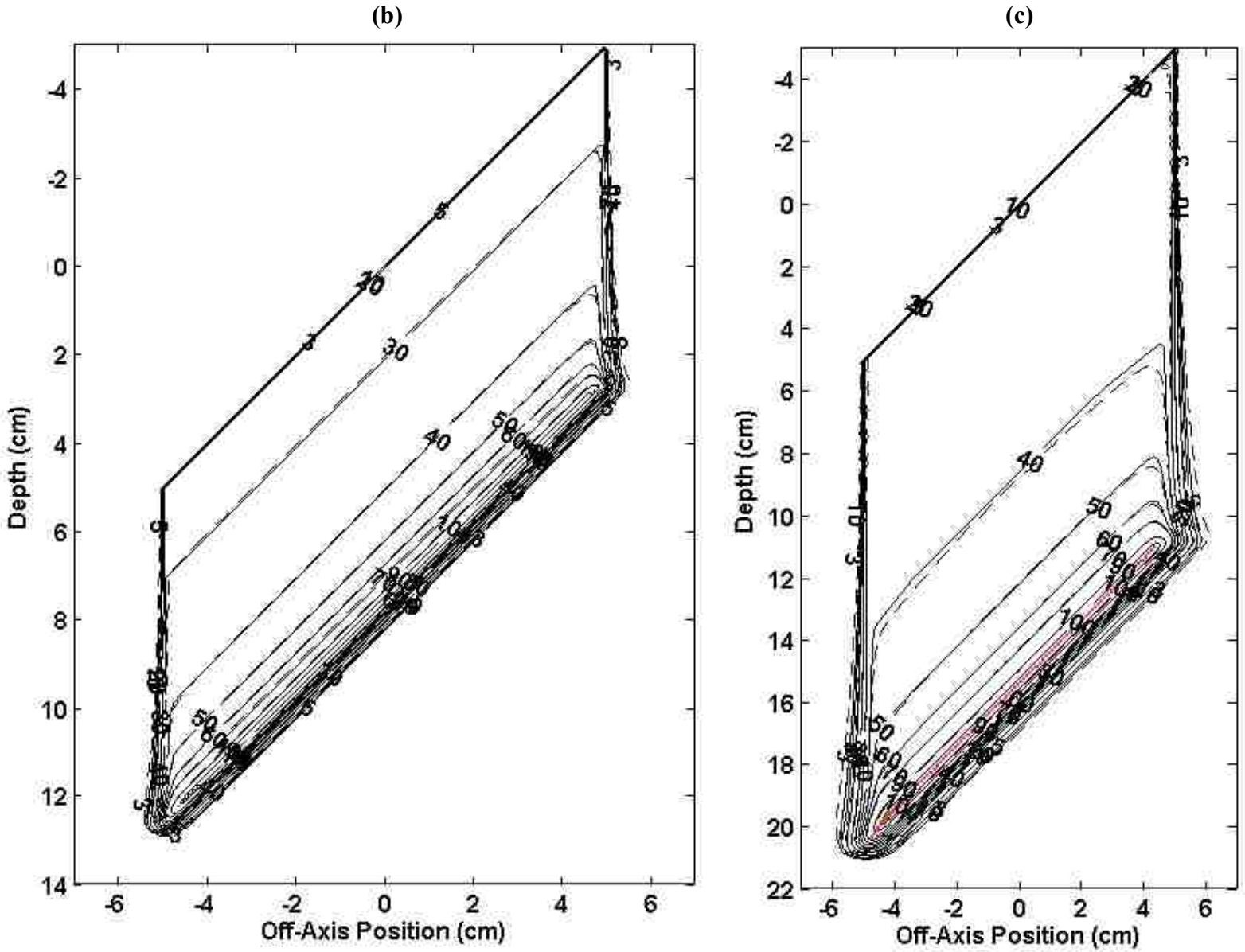

Figure 3.18 (continued)

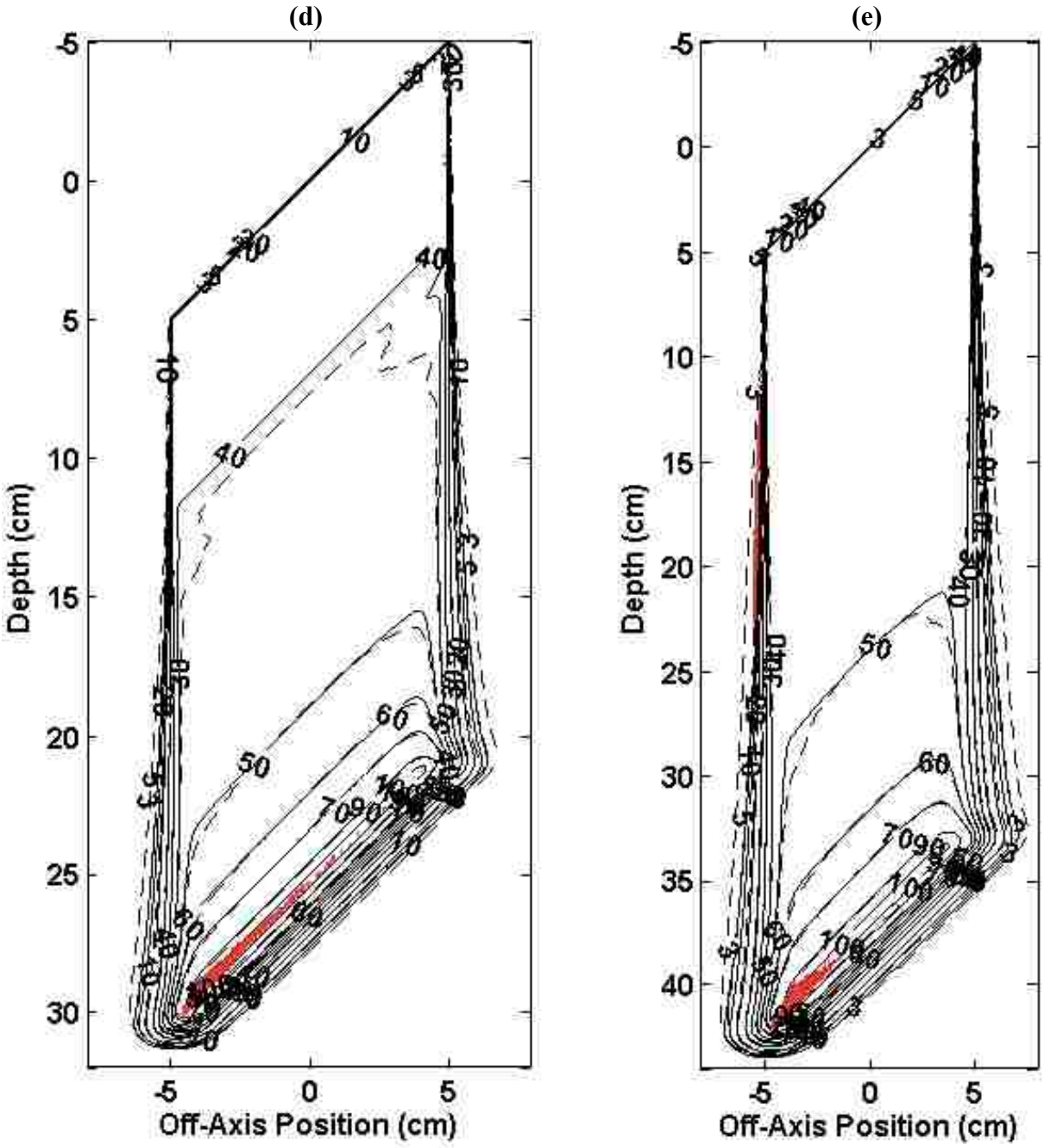

Figure 3.18 (continued)

In oblique geometry, lateral scatter for adjacent pencil beams begins at slightly different depths because the phantom surface is tilted relative to the beam (recall that material above the phantom is vacuum); the differing phantom entrance depths cause adjacent pencil beams to have slightly displaced Bragg peaks. Because narrow pristine Bragg peaks are used for depth dose curves in our model (see Figure 2.7) and because Bragg peaks from adjacent pencil beams are

displaced, lateral scatter out of the central-axis from one pencil beam is not replaced by lateral scatter in from an adjacent pencil beam; these factors cause loss of side scatter equilibrium.

Lateral profiles at the Bragg peak and central-axis depth dose comparisons between PBA and MC data were examined for 100 and 200 MeV beams with field sizes of 4x4 cm^2 and 10x10 cm^2 to study the limitations imposed by the loss of side scatter equilibrium in our oblique simulations. The central-axis profiles are shown in Figure 3.19.

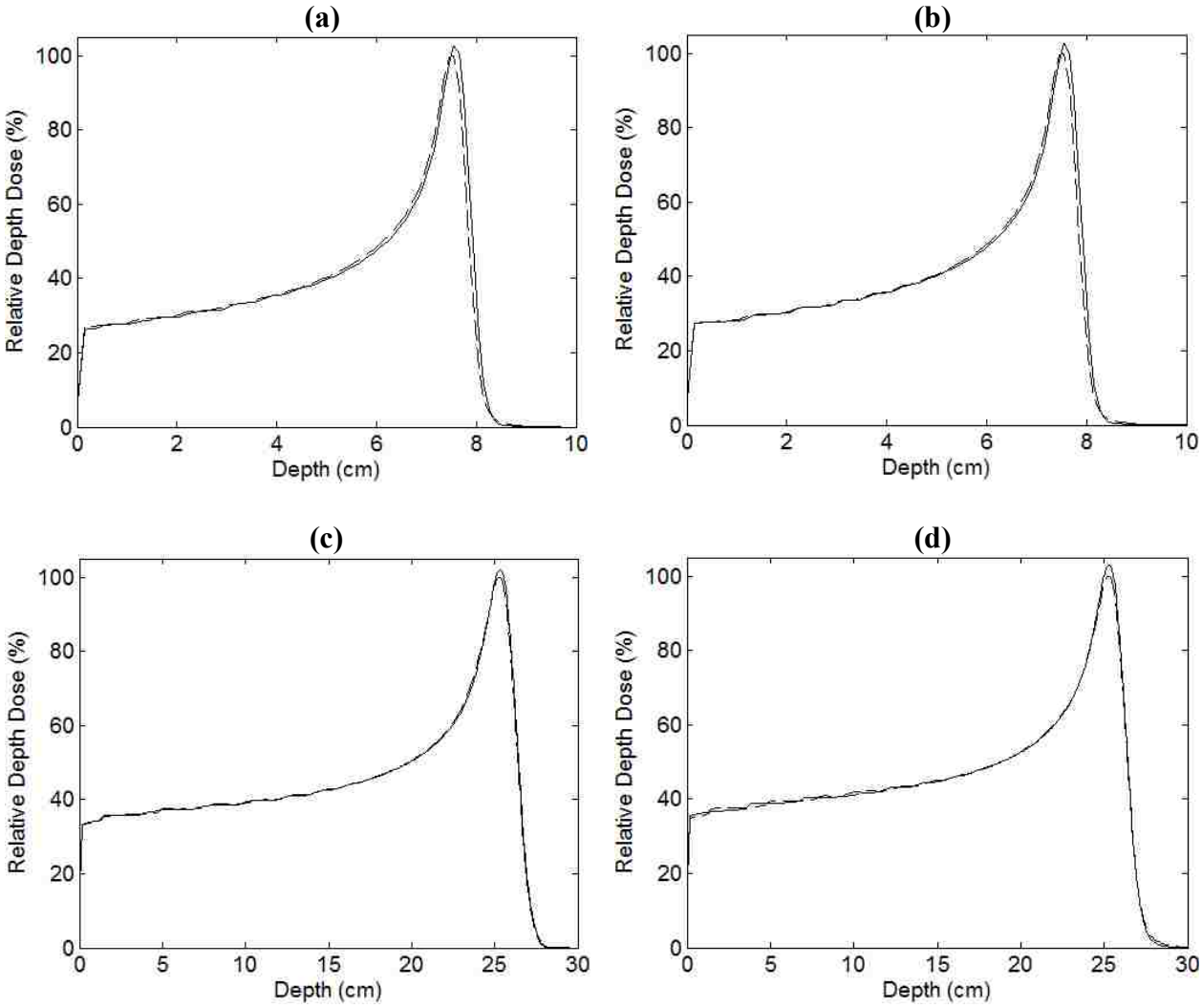

Figure 3.19: Central-axis profiles through the Bragg peak (in the beam frame) for the pencil beam algorithm (solid) and Monte Carlo calculations (dashed) in oblique phantoms at incident beam energies of 100 MeV (a,b) and 200 MeV (c,d). Simulations are shown with field sizes of 4x4 cm^2 (a,c) and 10x10 cm^2 (b,d).

To extract lateral profiles at the Bragg peak for the oblique simulations, (Figures 3.20 and 3.21), a coordinate rotation was applied to the data shown in Figures 3.17 and 3.18 so that the data was transformed to the frame of the beam. Lateral profiles at the Bragg peak are shown for 100 MeV (Figure 3.20) and 200 MeV (Figure 3.21).

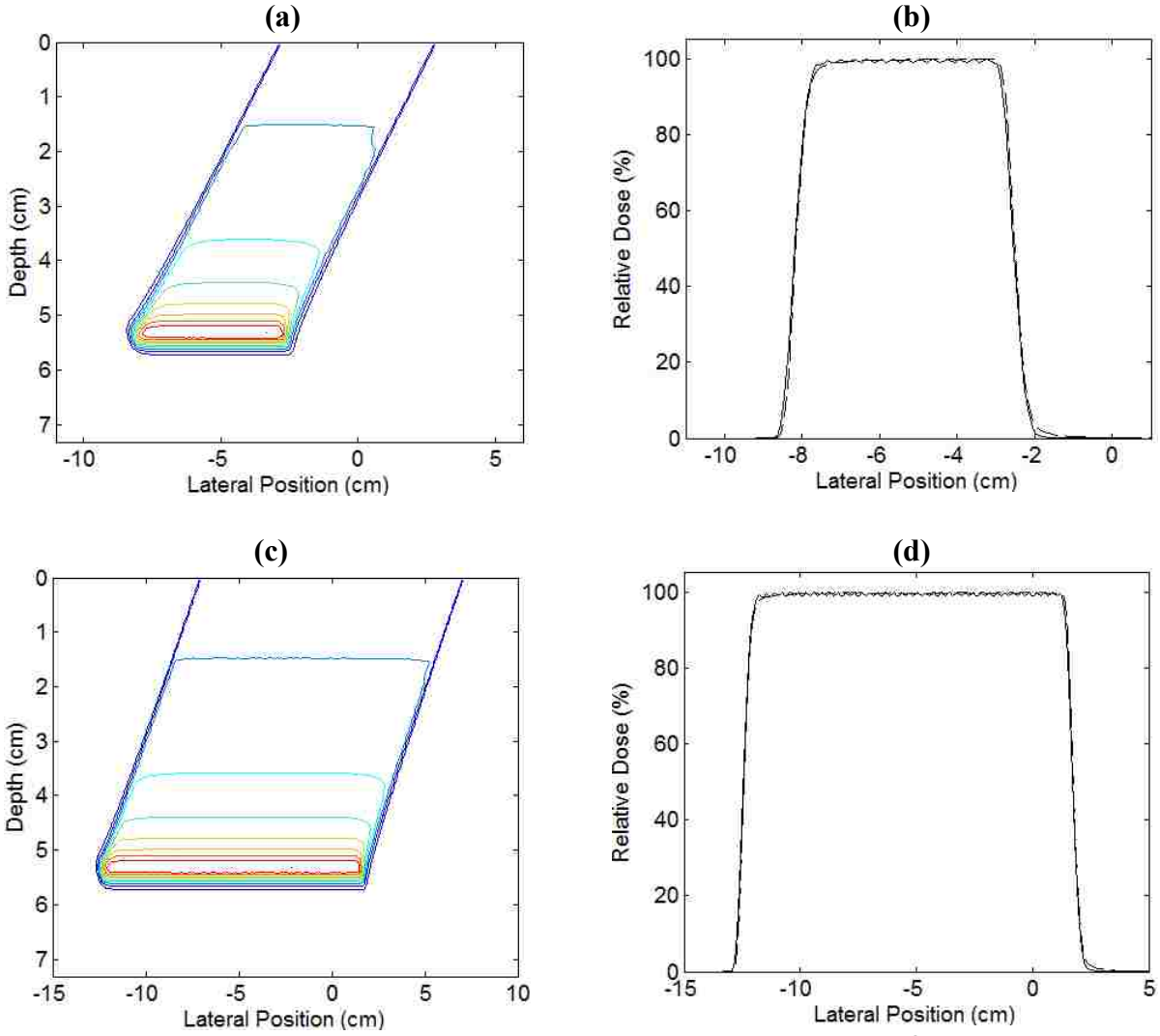

Figure 3.20: Oblique incidence simulations for 100 MeV beams for 4x4 cm^2 (a,b) and 10x10 cm^2 fields (c,d). Monte Carlo data is illustrated in the frame of the beam in (a, c) because this geometry was required to obtain lateral profiles through the Bragg peak in (b, d). The lateral profiles are shown for the pencil beam algorithm (PBA) (solid) and Monte Carlo (MC) (dashed) data. Rippling near the maximum dose area of the PBA appears because a coordinate rotation had to be applied to the PBA data in Figures 3.17(b) and 3.18(b).

Failures oriented towards the negative side of the central-axis (largest SSD), as discussed for Figures 3.17 and 3.18, are more evident in Figure 3.21 than 3.20; this relationship is

consistent with Figures 3.17 and 3.18 in that the loss of side scatter equilibrium is worsened for increasing incident beam energy and field size. In Figure 3.21(b) and (d), the MC data can be seen to drop below the values in the PBA data on the negative side of the central-axis and this effect is more noticeable for the 200 MeV 10x10 cm^2 field size (Figure 3.21(d)) over the 4x4 cm^2 field size (Figure 3.21(b)) simulation.

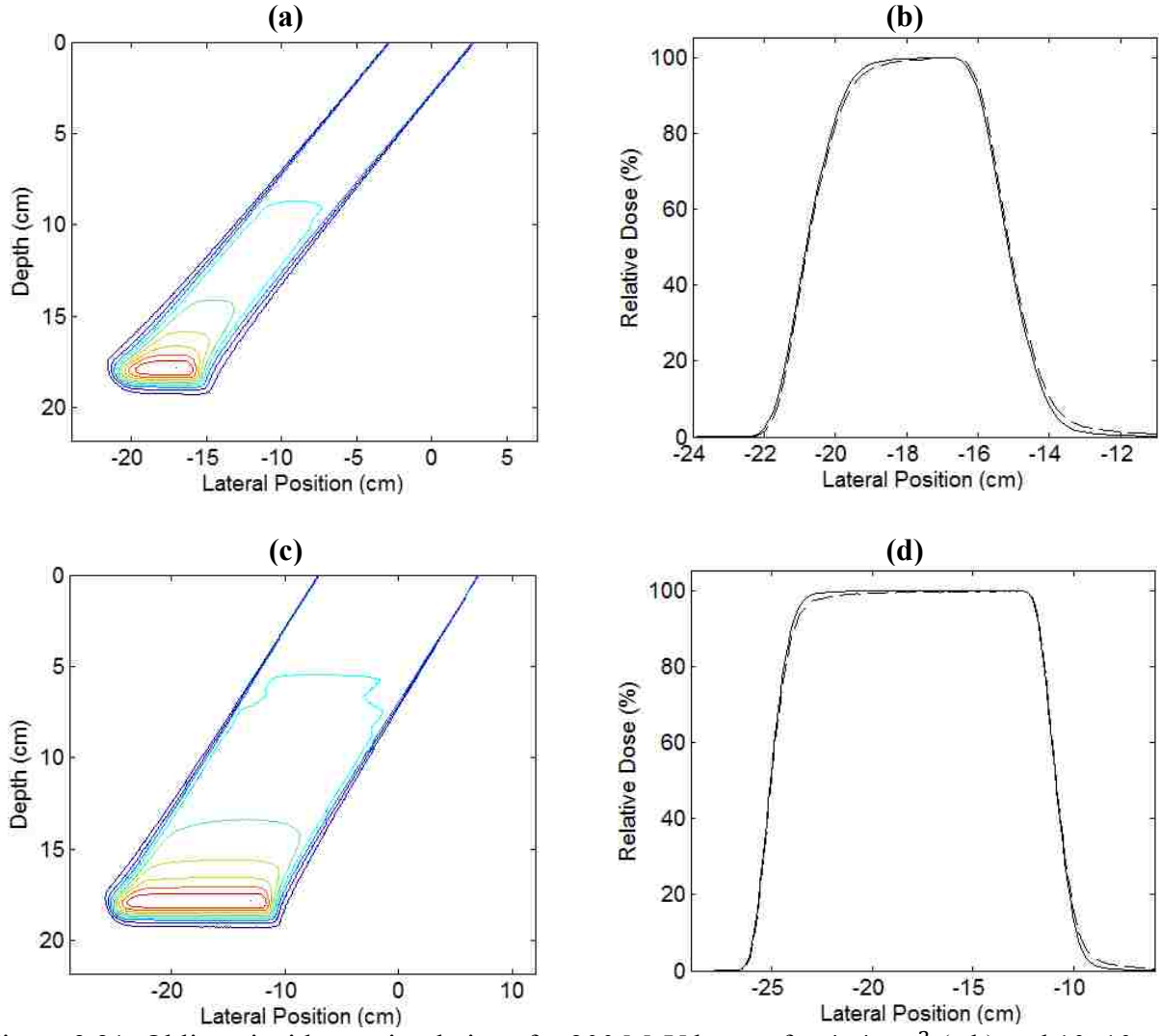

Figure 3.21: Oblique incidence simulations for 200 MeV beams for 4x4 cm^2 (a,b) and 10x10 cm^2 fields (c,d). Monte Carlo data is illustrated in the frame of the beam in (a, c) because this geometry was required to obtain lateral profiles through the Bragg peak in (b, d). The lateral profiles are shown for the pencil beam algorithm (PBA) (solid) and Monte Carlo (MC) (dashed) data. Rippling near the maximum dose area of the PBA appears because a coordinate rotation had to be applied to the PBA data in Figures 3.17(d) and 3.18(d).

3.3 Summary of Results

The percentages of passing points from all PBA simulations compared to MC data are presented in Table 3.1; as discussed in section 2.3.2, these percentages indicate DTA $\leq$ 1mm or dose difference $\leq$ 2% between the PBA and MC data. In general, the percentage of passing points decreases with increasing complexity of the dose calculation phantom, and with increasing incident energy. It is also apparent from Table 3.1 that failures in the oblique simulations worsen with increasing field size. As explained in section 3.2.3, the loss of side scatter equilibrium between adjacent pencil beams near the Bragg peak depth creates failures which worsen for pencil beams on the negative side of the central-axis (largest SSD); with an increasing field size, this effect is exacerbated because there are more pencil beams present that are not at side scatter equilibrium.

Table 3.1: Percentage of passing points for all simulations.

Field Size	**4x4 cm^2**				**10x10 cm^2**			
Energy (MeV)	**Flat**	**Step Height (cm)**		**Tilt (deg)**	**Flat**	**Step Height (cm)**		**Tilt (deg)**
		1	**4**	**45**		**1**	**4**	**45**
50	100	100	99.4	99.0	100	100	99.2	100
100	100	100	99.9	100	100	100	100	100
150	100	100	100	99.7	100	100	100	99.5
200	100	99.9	99.9	99.9	100	100	99.9	99.4
250	100	100	100	100	99.9	99.9	99.8	99.2

Some results in Table 3.1 may show a 100% pass rate with a corresponding figure that indicates red areas of failure; this occurred for some simulations because the pass rate was rounded to a single decimal place.

Neglecting the 50 MeV data (which was argued to have artificially low passing percentages in previous sections) and the oblique simulations for a 10x10 cm^2 field size, all

simulations pass with at least 99.7% of passing points; considering all data, the lowest pass rate was 99%. However, 25 of the 40 simulations performed for our dose model demonstrated 100% agreement with MC data.

CHAPTER 4. DISCUSSION AND CONCLUSIONS

4.1 Study Summary

We developed a proton pencil beam algorithm (PBA) which incorporates dose from primary protons and secondary protons created in nonelastic nuclear interactions. The beam width was estimated in the model by assuming Gaussian distributions for each pencil beam and we calculated the root mean square (RMS) value from Fermi-Eyges theory. The differential Moliere method introduced by Gottschalk (2010) was used to determine scattering power in the Fermi-Eyges calculations. The Fermi-Eyges equations were discretized by using recursion relations introduced by Hogstrom (1987). The sigmas needed for the nuclear pencil beams were obtained by a nonlinear least squares fit to Monte Carlo (MC) data (1x1 mm^2 field size) using the Levenberg-Marquardt method.

Central-axis data from MC simulations were used to commission the PBA, and analytical corrections were needed to force the central-axis dose predicted by the PBA to be equal to the input MC central-axis dose. Stopping power data was determined using PSTAR data and a ray-trace over the calculation grid to estimate the energy at each grid point (using the continuous slowing down approximation (CSDA)). Several material parameters were needed to include the desired materials into the PBA.

The accuracy of the PBA results was evaluated by comparing the distance-to-agreement (DTA) and the dose difference between the PBA and the MC values. To evaluate the versatility of the PBA, we ran simulations with perpendicularly incident beams and oblique beams, and we used flat and stepped phantom surfaces. Both the PBA and the MC distributions were normalized to the maximum dose in a flat water phantom (*i.e.,* the PBA was normalized to the maximum dose in a flat water phantom simulation by the PBA and the MC was normalized to the maximum dose in a flat water phantom simulation by MC), and assigned the value of 100%.

The agreement between the PBA and MC results were considered passing for DTA $\leq$ 1 mm or percent dose difference $\leq$ 2%. To evaluate the overall agreement between the PBA and MC results, we used the percentage of points that pass these criteria. To avoid erroneously high percent agreement results, we did not test points outside of 1% of the maximum dose in the MC distributions. In all the simulations that we performed, we found that 99% or greater of all the tested points pass these criteria. Therefore, we feel that our results show that the PBA is adequate for dose calculation.

4.2 Comparison with Literature

When compared with data from Ciangaru *et al.* (2005), our PBA showed improved Δ(20%-80%) penumbral widths (calculated as the difference between the PBA 20%-80% penumbral width and the MC 20%-80% penumbral width). These metrics were calculated for all three energies tested in the Ciangaru *et al.* (2005) model; results are shown in Figure 4.1 (only shown for the negative side of the central-axis since the profiles were symmetric) and presented in Table 4.1. In Figure 4.1, MC data from the Ciangaru *et al.* (2005) model is not shown since it was close to the data used in this work. The Ciangaru *et al.* (2005) model accounted for multiple Coulomb scatter, single scatter, and plural scatter but did not model nonelastic nuclear effects; we believe that the addition of our nonelastic nuclear model allowed improved results.

Table 4.1: Δ(20%-80%) penumbral width comparisons between our model and previous literature (Ciangaru *et al.* 2005).

Energy (MeV)	**Δ20%-80% Penumbral Widths (mm)**	
	This work	Ciangaru *et al.* (2005)
158.5	0.27	1.5
188.4	0.28	1.0
214.5	0.22	2.5

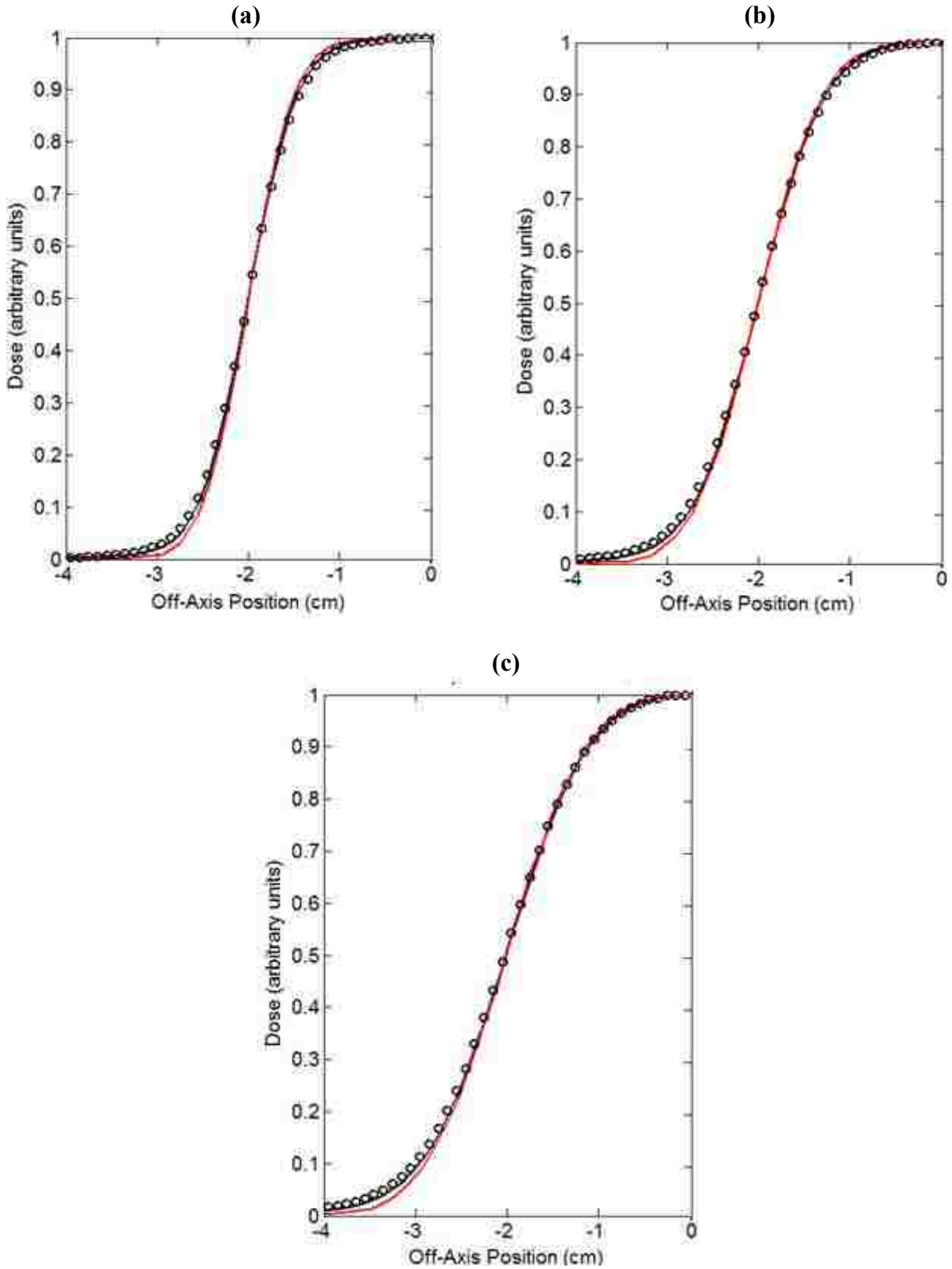

Figure 4.1: Comparison of Δ(20%-80%) penumbral widths between our model (black curve) and the Ciangaru *et al.* (2005) model (red curve) when compared to Monte Carlo data (black circles). Data is shown at incident energies of (a) 158.5, (b) 188.5, and (c) 214.5 MeV.

4.3 Recommendations for Algorithm Improvements

From section 3.1, it is clear that using two Gaussians to fit narrow field MC (1x1 mm^2 field size) data is not adequate to completely describe the distant falloff tails in the MC simulations, especially for shallow depths. However, for the simulations in this work, it seems that even though the nuclear halo is not modeled well at shallow depths, this effect is minimized over several pencil beams because a homogeneous water phantom was used. For mixed material simulations in the future, we will need to produce an improved nuclear model. In the next phase of this study, we intend to develop a first principles nuclear halo model that should more accurately account for the physics involved in nonelastic nuclear events.

Hanson's approximation, as used with the differential Moliere scattering power in our algorithm, seems to account for the majority of the primary dose in our simulations – out to about the 4% of maximum isodose level. It is clear from the lateral profiles shown in the results section that the falloff edges of the distribution in the PBA are sharper than that in the MC distributions. We attribute this to the limitations of Hanson's approximation of Moliere theory and the two-Gaussian fit to narrow field MC data. It is well known that Hanson's approximation, as a Gaussian, accounts for most of the Moliere distribution but at some point the Moliere distribution will falloff more gradually (the Hanson distribution is a best fit to Moliere theory out to the *1/e* width – see Appendix section D.2). Over several summed pencil beams, the limitations of the Gaussians used in pencil beam modeling will cause the dose falloff tails of broad field data to disagree. Figure 4.2 gives a graphical comparison of Hanson and Moliere theory.

4.4 Future Dose Calculation Studies

Research is underway in our clinic to directly simulate the nuclear halo distribution for a pencil beam from Monte Carlo N-Particle eXtended (MCNPX). In these studies, the nuclear

halo is being quantified at further lateral distances than was used in this work (-10 to 10 cm lateral to the central-axis). Additional modeling of the nuclear halo distribution will likely result in better quantification of the effects associated with the nuclear halo and overall better fits to MC data. Once we have obtained the fully quantified nuclear halo distribution, we intend to develop a first principles halo model and compare it with the distributions produced by MCNPX.

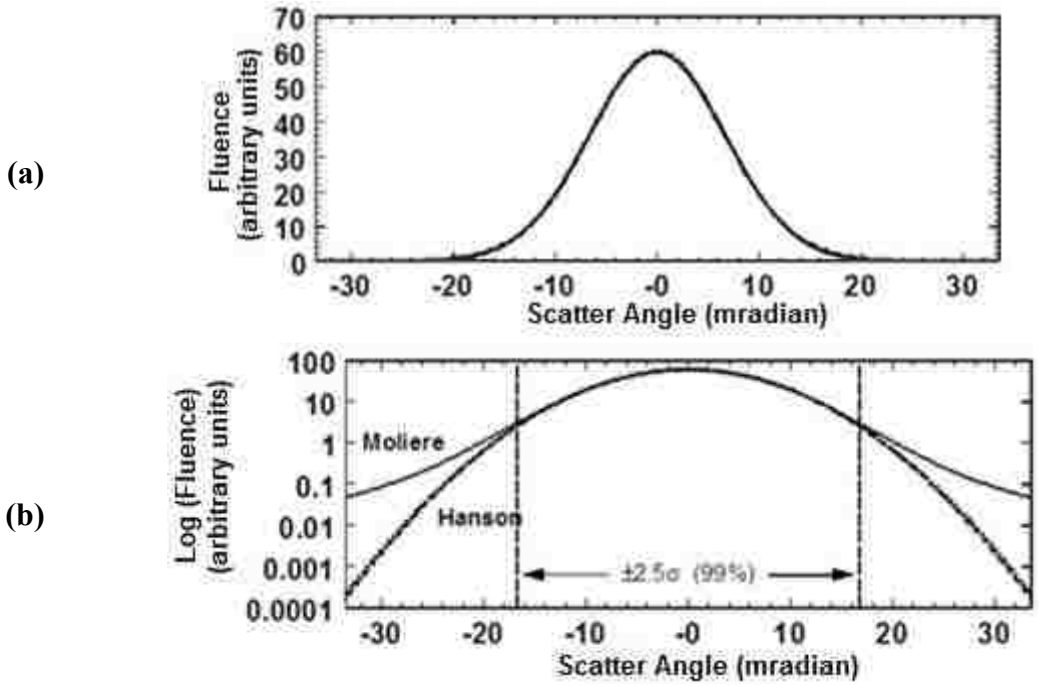

Figure 4.2: Comparison of Hanson and Moliere theory: (a) on a linear scale; (b) on a semi-logarithmic scale. Hanson's approximation begins to differ from the Moliere distribution at 2.5σ. These plots are shown at an energy of 160 MeV, but the relation between Hanson and Moliere theory is retained for other beam energies (Gottschalk 2011).

To extend our dose calculation model to more clinically relevant simulations, specific beam phase space parameters will need to be accounted for and benchmarked in patient-like inhomogeneous phantoms. Future models of this PBA should incorporate the necessary degrees of freedom to calculate dose from the increasingly abundant advanced accelerator technologies. Beam optimization, such as the use of spread-out Bragg peaks (SOBP) or more complicated active scanning optimization routines, is a logical step in extending the clinical relevance of the present PBA. One advantage of using beam optimization in our PBA is that the side scatter

equilibrium problems created at the Bragg peak depth (because of the pristine Bragg peaks used in our model) in our oblique simulations would likely disappear. The increased high dose area in an optimized beam would be expected to achieve side scatter equilibrium in these oblique simulations because the slight displacement of the center of the peaks would be small in comparison to the width of the high dose area.

Another consideration that will need to be incorporated in our model when it is extended to include beam phase space calculations is the air gap effects that cause pencil beams to poorly account for effects at the phantom surface. As mentioned in section 2.1.1, Hogstrom *et al.* (1981) solved this problem by using a deconvolution method. Such deconvolution methods will need to be implemented into our future PBA as well. The deconvolution method effectively redefines pencil beams at the surface of the phantom (or patient). The success of a single pencil beam redefinition on patient surface effects motivated the development of the pencil beam redefinition algorithm (PBRA) (Shiu and Hogstrom 1991) to improve limitations imposed by the central-axis semi-infinite slab approximation used for pencil beams. In the future, we plan to extend our PBA to a PBRA, using a methodology similar to Shiu and Hogstrom (1991). Even though protons travel in nearly straight lines until near the Bragg peak, we feel that redefinition will help in general patient simulations and will likely improve some limitations imposed in our PBA by the central-axis semi-infinite slab approximation; specifically, the failures in the step phantoms due to the central-axis approximation of pencil beams would be improved with a PBRA.

As a last improvement to our model, we will use a constant of proportionality in the dose equations of our future model and characterize it so that our model will determine directly absolute dose rather than relative dose, as calculated in the present PBA. Our future absolute dose calculation algorithm will follow the methodology of Koch *et al.* (2008).

REFERENCES

Berger, M.J., 1963. Monte Carlo calculation of the penetration and diffusion of fast charged particles. *Meth. Comp. Phys.*, 1, 135-215.

Berger, M.J., 1993. Penetration of proton beams through water I. Depth dose distribution, spectra and LET distribution. *NISTIR 5226.*

Berger, M.J., Coursey, J.S., Zucker, M.A., and Chang, J. (2005), *ESTAR, PSTAR, and ASTAR: Computer Programs for Calculating Stopping-Power and Range Tables for Electrons, Protons, and Helium Ions* (version 1.2.3). [Online] Available: http://physics.nist.gov/Star [2011, September 14], National Institute of Standards and Technology, Gaithersburg, MD.

Bethe, H.A., 1953. Moliere's theory of multiple scattering. *Phys. Rev.,* 89, 1256-66.

Bohr, N., 1948. The penetration of atomic particles through matter. *K. Dan. Vidensk. Selsk. Mat. Fys. Medd.*, 18(8), 1-144.

Chu W.T., Ludewigt B.A., and Renner T.R., 1993. Instrumentation for treatment of cancer using proton and light-ion beams. *Rev. Sci. Instrum.,* 64, 2055-2122.

Ciangaru G., Polf J.C., Bues M., and Smith A.R., 2005. Benchmarking analytical calculations of proton doses in heterogeneous matter. *Med. Phys.,* 32(12), 3511-23.

Deasy, J.O., 1998. A proton dose calculation algorithm for conformal therapy simulations based on Moliere's theory of lateral deflections. *Med. Phys.,* 25(4), 476-83.

Eyges, L., 1948. Multiple scattering with energy loss. *Phys. Rev.,* 74, 1534-35.

Fano, U., 1954. Inelastic collisions and the Moliere theory of multiple scattering. *Phys. Rev.,* 93, 117-120.

Gottschalk B., Koehler A. M., Schneider R. J., Sisterson J. M., and Wagner, M. S., 1993. Multiple Coulomb scattering of 160 MeV protons. *Nucl. Instr. Meth.* B74, 467-90.

Gottschalk, B., 2004. Passive Beam Spreading in Proton Radiation Therapy. *Unpublished book.* Available: http://physics.harvard.edu/~gottschalk.

Gottschalk, B., 2010. On the scattering power of radiotherapy protons. *Med. Phys.,* 37(1), 352-67.

Gottschalk, B., 2011. *Scattering.* [PowerPoint slides]. Harvard: Harvard University. Available at: Bernard Gottschalk's Harvard University Physics Site. Module 8. <http://physics.harvard.edu/~gottschalk> (accessed 13 October, 2011).

Hanson A.O., Lanzl L.H., Lyman E.M., and Scott M.B., 1951. Measurement of multiple scattering of 15.7-MeV electrons. *Phys. Rev.,* 84, 634-37.

Highland, V.L., 1975. Some practical remarks on multiple scattering. *Nucl. Instr. Meth.,* 129, 497-499.

Hogstrom K.R., Mills M.D., and Almond P.R., 1981. Electron beam dose calculations. *Phys. Med. Biol.,* 26, 445-59.

Hogstrom, K.R., 1987. Evaluation of electron pencil beam dose calculations. In: J. Kereiakes, H. Elson and C. Born (eds). Radiation Oncology Physics – 1986: Proceedings of the 1986 Summer School of the AAPM, 532-57, New York; American Institute of Physics, 1987.

Hogstrom, K.R., 2003. Electron beam therapy: dosimetry, planning, and techniques. *Principles and Practice of Radiation Oncology,* eds. C. Perez, I. Brady, E. Halperin and R. Schmidt-Ullrich, 252-82 Baltimore: Lippinkott, Williams, and Wilkins.

Hong L., Goitein M., Bucciolini M., Comiskey R., Gottschalk B., Rosenthal S., Serago C., and Urie M., 1996. A pencil beam algorithm for proton dose calculations. *Phys. Med Biol.*, 41, 1305-1330.

ICRU, 1984. Radiation dosimetry: electron beams with energies between 1 and 50 MeV, Technical Report no. 35, *International Commission on Radiation Units and Measurements, Inc.,* Washington, D.C.

ICRU, 1998. Clinical proton dosimetry – part I: beam production, beam delivery and measurement of absorbed dose, Technical Report no. 59, *International Commission on Radiation Units and Measurements, Inc*., Washington, D.C.

ICRU, 2000. Nuclear data for neutron and proton radiotherapy and for radiation protection, Technical Report no. 63*, International Commission on Radiation Units and Measurements, Inc.*, Washington, D.C.

Khan, F.M., 2010. *The Physics of Radiation Therapy*. 4th ed. Philadelpha: Wolters Kluwer Health / Lippincott Williams and Wilkins.

Koch N. and Newhauser W., 2005. Virtual commissioning of a treatment planning system for proton therapy of ocular cancers. *Radiat. Prot. Dosim.,* 115, 159-63.

Koch N., Newhauser W.D., Titt U., Gombos D., Coombes K., and Starkschall G., 2008. Monte Carlo calculations and measurements of absorbed dose per monitor unit for the treatment of uveal melanoma with proton therapy. *Phys. Med. Biol.,* 53, 1581-94.

Koehler A.M. and Preston W.M., 1972. Protons in radiation therapy. Comparative dose distributions for protons, photons, and electrons. *Radiology*, 104, 191-5.

Madsen K., et al., 2004. *Methods for Non-Linear Least Squares Problems*. Technical University of Denmark.

Mancuso, G. M., 2011. *Evaluation of Volumetric Modulated Arc Therapy (VMAT) Patient Specific Quality Assurance.* Thesis, (Masters). Louisiana State University. Available at http://etd.uis.lsu.edu/cgi-bin/ETD-browse/browse.

MCNPX, 2005. MCNPX user's manual. *Los Alamos National Laboratory,* Los Alamos, NM.

Newhauser W., 2001. Dosimetry for the gantry beams at the northeast proton therapy center: Part I: Dimensions and geometric relationships. *Mass. Gen. Hosp. Report HD-112.*

Newhauser W., Fontenot J., Koch N., Dong L., Lee A., Zheng Y., Waters L., and Mohan R., 2007a. Monte Carlo simulations of the dosimetric impact of radiopaque fiducial markers for proton radiotherapy of the prostate. *Phys. Med. Biol.,* 52, 2937-52.

Newhauser W., Fontenot J., Zheng Y., Polf J., Titt U., Koch N., Zhang X., and Mohan R., 2007b. Monte Carlo simulations for configuring and testing an analytical proton dose-calculation algorithm. *Phys. Med. Biol.,* 52, 4569-4584.

Overas H., 1960. On small angle multiple scattering in confined bodies. *CERN Yellow Report,* 60-18.

Pedroni E., Bacher R., Blattmann H., Bohringer T., Coray A., Lomax A., Lin S., Munkel G., Scheib S., Schneider U., and Tourovsky A., 1995. The 200 MeV proton therapy project at the Paul Scherrer Institute: Conceptual design and practical realization. *Med. Phys.,* 22(1), 37-53.

Pedroni E., Scheib S., Bohringer T., Coray A., Grossman M., Lin S. and Lomax A., 2005. Experimental characterization of physical modeling of the dose distribution of scanned proton pencil beams. *Phys Med. Biol.*, 50, 541-61.

Petti, P.L., 1991. Differential-pencil-beam dose calculations for charged particles. *Med. Phys.*, 19(1), 137-49.

PTCOG, 2012. *Particle therapy facilities in operation.* [Online] Available at: http://ptcog.web.psi.ch/ptcentres.html [Accessed 30 January 2010].

Rossi B. and Greisen K., 1941. Cosmic-Ray Theory. *Rev. Mod. Phys.,* 12, 240-309.

Russell K.R., Grussell E., and Montelius A., 1995. Dose calculations in proton beams: range straggling corrections and energy scaling. *Phys. Med. Biol.,* 40, 1031-1043.

Russell K.R., Isacsson U., Saxner M., Ahnesjo A., Montelius A., Grusell E., Dahlgren C.V., Lorin S., and Glimelius B., 2000. Implementation of pencil kernel and depth penetration algorithms for treatment planning of proton beams. *Phys. Med. Biol.,* 45, 9-27.

Schaffner B., Pedroni E., and Lomax A., 1999. Dose calculation models for proton treatment planning using a dynamic beam delivery system: an attempt to include density heterogeneity effects in the analytical dose calculation. *Phys. Med. Biol.,* 44, 27-41.

Schaffner, B., 2007. *Proton dose calculation algorithms and configuration data.* [PowerPoint slides]. *PTCOG 46*, Wanjie, China, Wanjie Proton Therapy Center. Available at: PTCOG website. <ptcog.web.psi.ch/ptcog46_talks.html> (accessed 15 March, 2012).

Schaffner, B., 2008. Proton dose calculation based on in-air fluence measurements. *Phys. Med. Biol.,* 53, 1545-62.

Scott, W.T., 1963. The theory of small-angle multiple scattering of fast charged particles. *Rev. Mod. Phys.,* 35, 231-313.

Seltzer, S.M., 1993. An assessment of the role of charged secondaries from nonelastic nuclear interactions by therapy proton beams in water. *NISTIR 5221*.

Shiu A.S. and Hogstrom K.R., 1991. Pencil-beam redefinition for electron dose distributions. *Med. Phys.,* 18(1), 7-18.

Sisterson J.M., Urie M., Koehler A.M., and Goitein M., 1989. Distal penetration of proton beams: the effects of air gaps between compensating bolus and patient. *Phys. Med. Biol.*, 34, 1309-15.

Slater J.M., Archambeau J.O., Miller D.W., Notaru M.I., Preston W., and Slater J.D., 1991. The proton treatment center at Loma Linda University Medical Center. *Int. J. Radiat. Oncol., Biol., Phys.,* 22, 383-89.

Soukup M., Fippel M., and Alber M., 2005. A pencil beam algorithm for intensity modulated proton therapy derived from Monte Carlo simulations. *Phys. Med. Biol.* 50, 5089-104.

Syzmanowski H. and Oelfke U., 2002. Two-dimensional pencil beam scaling: an improved proton dose algorithm for heterogeneous media. *Phys. Med. Biol.,* 47(18), 3313-30.

Terasawa T., Dvorak T., Ip S., Raman G., Lau J., and Trikalinos TA., 2009. Systematic review: charged-particle radiation therapy for cancer. *Ann. Intern. Med.*, 151(8), 556-65.

Tobias C.A., Lawrence J.H., Born J.L., McCombs R., Roberts J.E., Anger H.O., Low-Beer B.V.A., and Huggins C., 1958. Pituitary irradiation with high energy proton beams: a preliminary report. *Cancer Res.,* 18, 121-34.

Urie M., Goitein M., Holley W.R., and Chen G.T.Y., 1986a. Degradation of the Bragg peak due to inhomogeneities. *Phys. Med. Biol.,* 31, 1-15.

Urie M., Sisterson J.M., Koehler A.M., Goitein M., and Zoesman J., 1986b. Proton beam penumbra: effects of separation between patient and beam modifying devices. *Med Phys.*, 13, 734-41.

Wilson, R.R., 1946. Radiological use of fast protons. *Radiology*, 47, 487-91.

Yepes P., Randeniya S., Taddei P.J., and Newhauser W.D., 2008. A track-repeating algorithm for fast Monte Carlo dose calculations of proton radiotherapy. *Nucl. Technol.,* 168, 736-40.

Yepes P.P, Mirkovic D., and Taddei P.J., 2010. A GPU implementation of a track-repeating algorithm for proton radiotherapy dose calculations. *Phys. Med Biol.,* 55, 7107-7120.

Zhang R. and Newhauser W.D., 2009. Calculation of water equivalent thickness of materials of arbitrary density, elemental composition and thickness in proton beam irradiation. *Phys. Med. Biol.*, 54, 1383-95.

APPENDIX A. FLOWCHARTS SHOWING PENCIL BEAM ALGORITHM

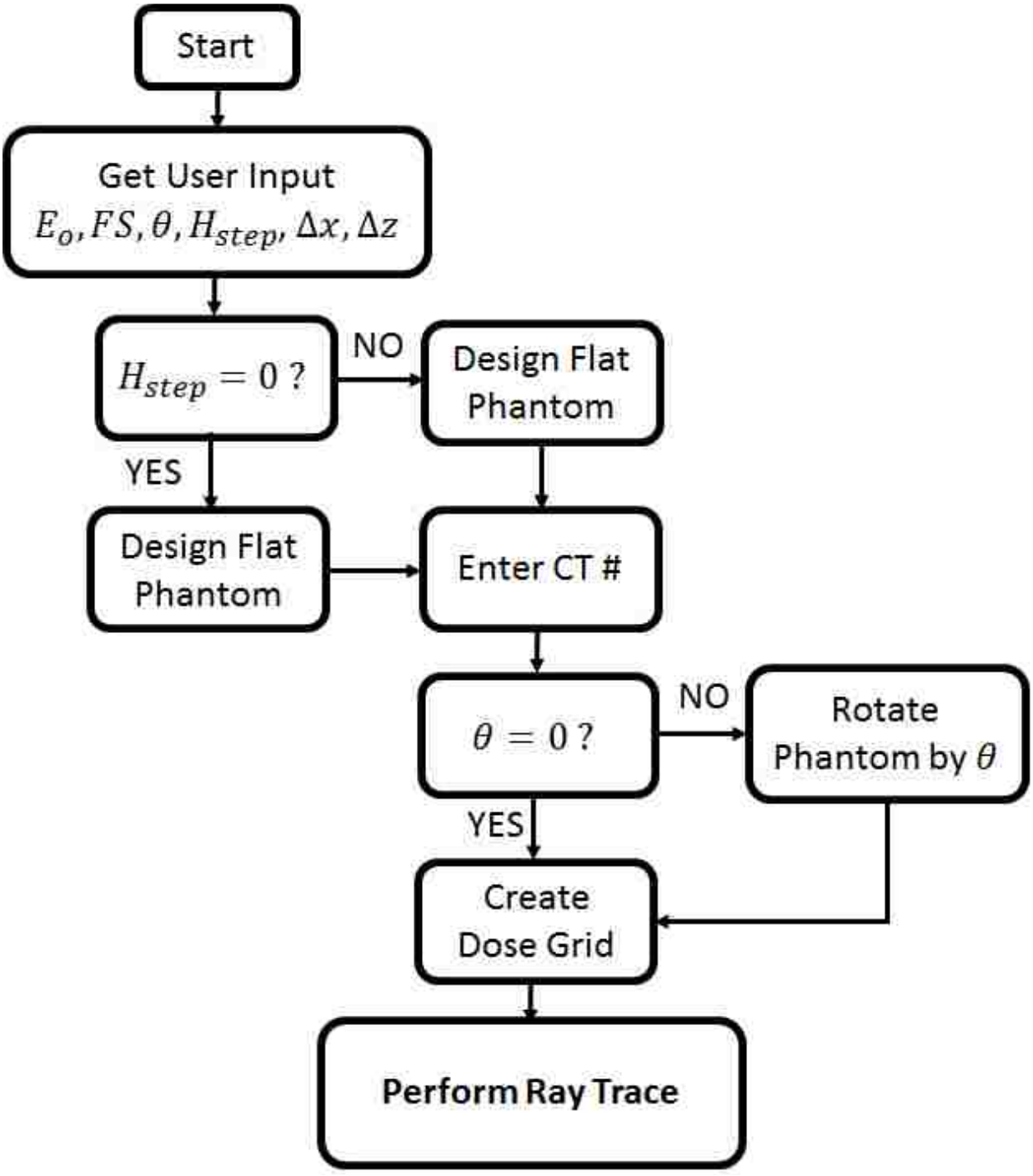

Figure A.1: Flowchart for the phantom design.

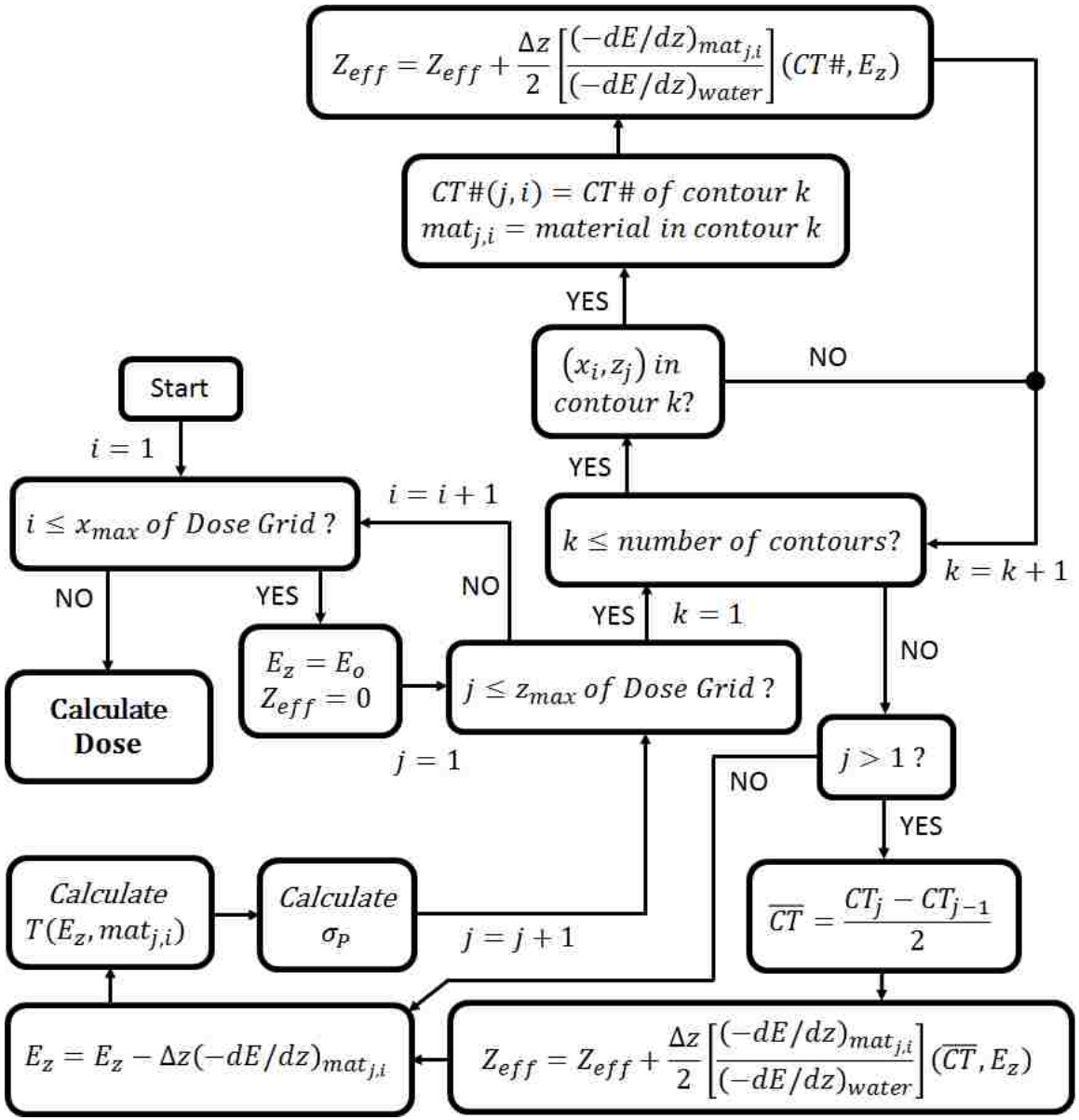

Figure A.2: Flowchart for the ray-trace.

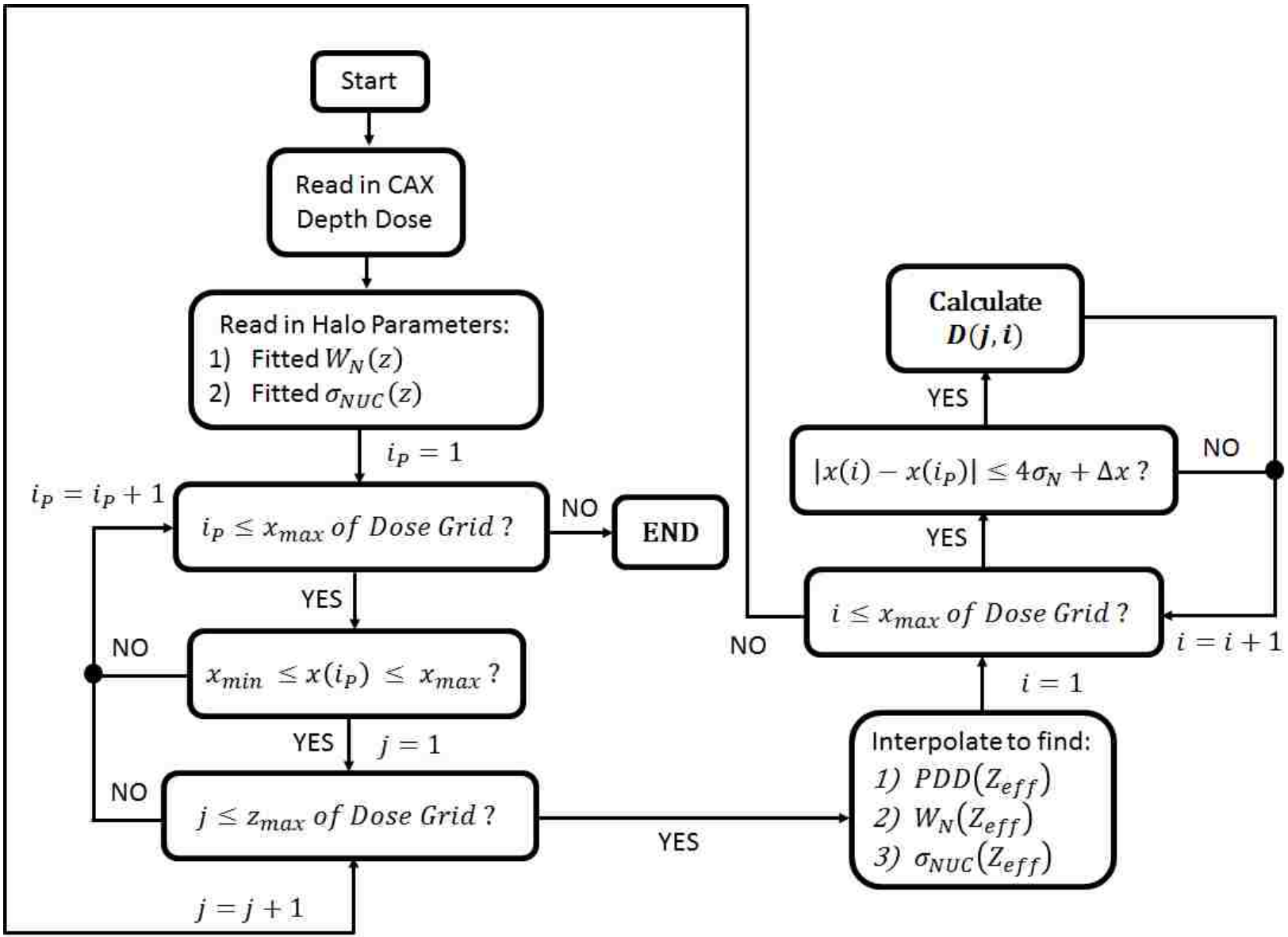

Figure A.3: Flowchart for the dose calculation.

APPENDIX B. DERIVATION OF PENCIL BEAM NORMALIZATION FACTORS

Given that the nuclear halo parameters were determined from a fit that incorporated the primary distribution, it would not be adequate to model the primary pencil beam out to $4\sigma_P$ and the nuclear halo pencil beam out to $4\sqrt{\sigma_P^2 + \sigma_N^2}$. Because the primary distribution is necessarily narrower than the halo distribution (it was fitted as such), then it will always be true that the 4-sigma width of the primary distribution (blue broken lines in Figure B.1) will be less than the 4-sigma width of the nuclear halo distribution (red broken lines in Figure B.1). Thus, it is necessary to model *both* distributions out to 4-sigma of the nuclear halo distribution. However, that implies that the width of the primary distribution that will be modeled will vary with depth (it will be dependent on the ratio of the primary sigma to the nuclear halo sigma and the 4-sigma width of the nuclear halo distribution). In this appendix, we will derive the equations necessary to describe the modeling width of the primary sigma and the resulting normalization equation.

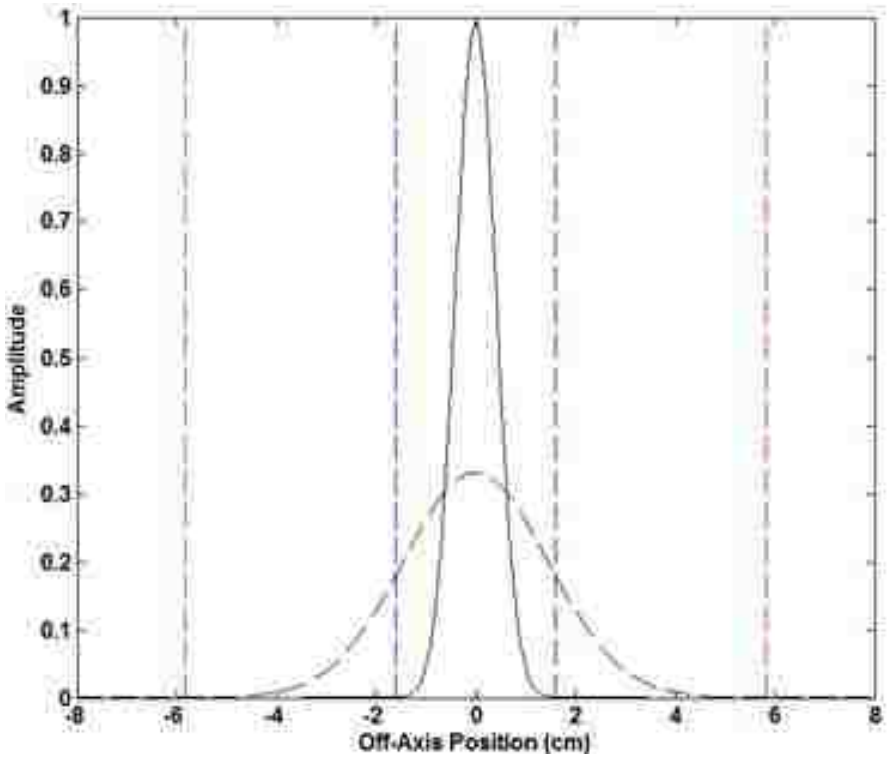

Figure B.1: Comparison of primary (solid black curve) and halo (broken black curve) pencil beam limits. The 4-sigma limits of the halo distribution are shown as red broken lines and the 4-sigma limits of the primary distribution are shown as blue broken lines.

To find the fluence for a primary pencil beam centered at $x = 0$ for an arbitrary off-axis location of $x = A\,\sigma_P$, we use

$$f_p(A\,\sigma_P, z) = \frac{1}{\sqrt{2\pi}\,\sigma_P}\exp\left(\frac{-A^2\sigma_P^2}{2\,\sigma_P^2}\right) = \frac{1}{\sqrt{2\pi}\,\sigma_P}\exp\left(\frac{-A^2}{2}\right). \tag{38}$$

Likewise, the fluence for a nuclear halo pencil beam centered at $x = 0$ for an arbitrary off-axis location of $x = B\sqrt{\sigma_P^2 + \sigma_N^2}$, we use

$$\begin{aligned} f_N\left(B\sqrt{\sigma_P^2 + \sigma_N^2}, z\right) &= \frac{1}{\sqrt{2\pi(\sigma_P^2 + \sigma_N^2)}}\exp\left(\frac{-B^2(\sigma_P^2 + \sigma_N^2)}{2\,(\sigma_P^2 + \sigma_N^2)}\right) \\ &= \frac{1}{\sqrt{2\pi(\sigma_P^2 + \sigma_N^2)}}\exp\left(\frac{-B^2}{2}\right). \end{aligned} \tag{39}$$

To find A, we simply recognize that the x-value that corresponds to B-sigma of the nuclear halo distribution must be equal to A-sigma of the primary distribution,

$$A = \frac{\sqrt{\sigma_P^2 + \sigma_N^2}}{\sigma_P}B = B\sqrt{1 + \left(\frac{\sigma_N}{\sigma_P}\right)^2}. \tag{40}$$

To derive the normalization factor for a given pencil beam distribution modeled out to Q-sigma, we begin by applying the standard normal coordinate,

$$Z = \frac{x}{\sigma} \tag{41}$$

and

$$dx = \sigma\,dz. \tag{42}$$

Then, to find the fluence out to Q-sigma, integration over the fluence from $-Q$ to Q is performed over the standard normal distribution

$$f(-Q < Z < Q) = \frac{1}{\sqrt{2\pi}}\int_{-Q}^{Q}\exp\left(\frac{-z'^2}{2}\right)dz'. \tag{43}$$

Letting

$$y = \frac{z'}{\sqrt{2}}, \tag{44}$$

we have

$$dz' = \sqrt{2}\, dy. \tag{45}$$

Then, the fluence equation becomes

$$\begin{aligned} f(-Q < Z < Q) &= \frac{1}{\sqrt{2\pi}} \int_{-Q/\sqrt{2}}^{Q/\sqrt{2}} \exp\left(\frac{-y^2}{2}\right) dy \\ &= \frac{1}{\sqrt{\pi}} \left[\int_0^{Q/\sqrt{2}} \exp(-y^2)\ dy - \int_0^{-Q/\sqrt{2}} \exp(-y^2)\ dy \right] \\ &= \frac{1}{2} \left[\operatorname{erf}\left(\frac{Q}{\sqrt{2}}\right) + \operatorname{erf}\left(\frac{Q}{\sqrt{2}}\right) \right] \\ &= \operatorname{erf}\left(\frac{Q}{\sqrt{2}}\right). \end{aligned} \tag{46}$$

To obtain a normalization factor,

$$Norm = \frac{1}{f(-Q < Z < Q)} = \left[\operatorname{erf}\left(\frac{Q}{\sqrt{2}}\right) \right]^{-1}. \tag{47}$$

Then, the normalization factor for 4-sigma over the nuclear halo distribution gives

$$Norm_N = \left[\operatorname{erf}\left(\frac{4}{\sqrt{2}}\right) \right]^{-1} = 1.0001. \tag{48}$$

Substituting equation (40) for the Q term in equation (47) with $B = 4$ gives the normalization factor for the primary pencil beam as

$$Norm_P = \left[\operatorname{erf}\left(\frac{4\sqrt{1 + \left(\frac{\sigma_N}{\sigma_P}\right)^2}}{\sqrt{2}} \right) \right]^{-1}. \tag{49}$$

APPENDIX C. ADDITIONAL PROFILES

C.1 Nuclear Halo Fit Depth Dose Components

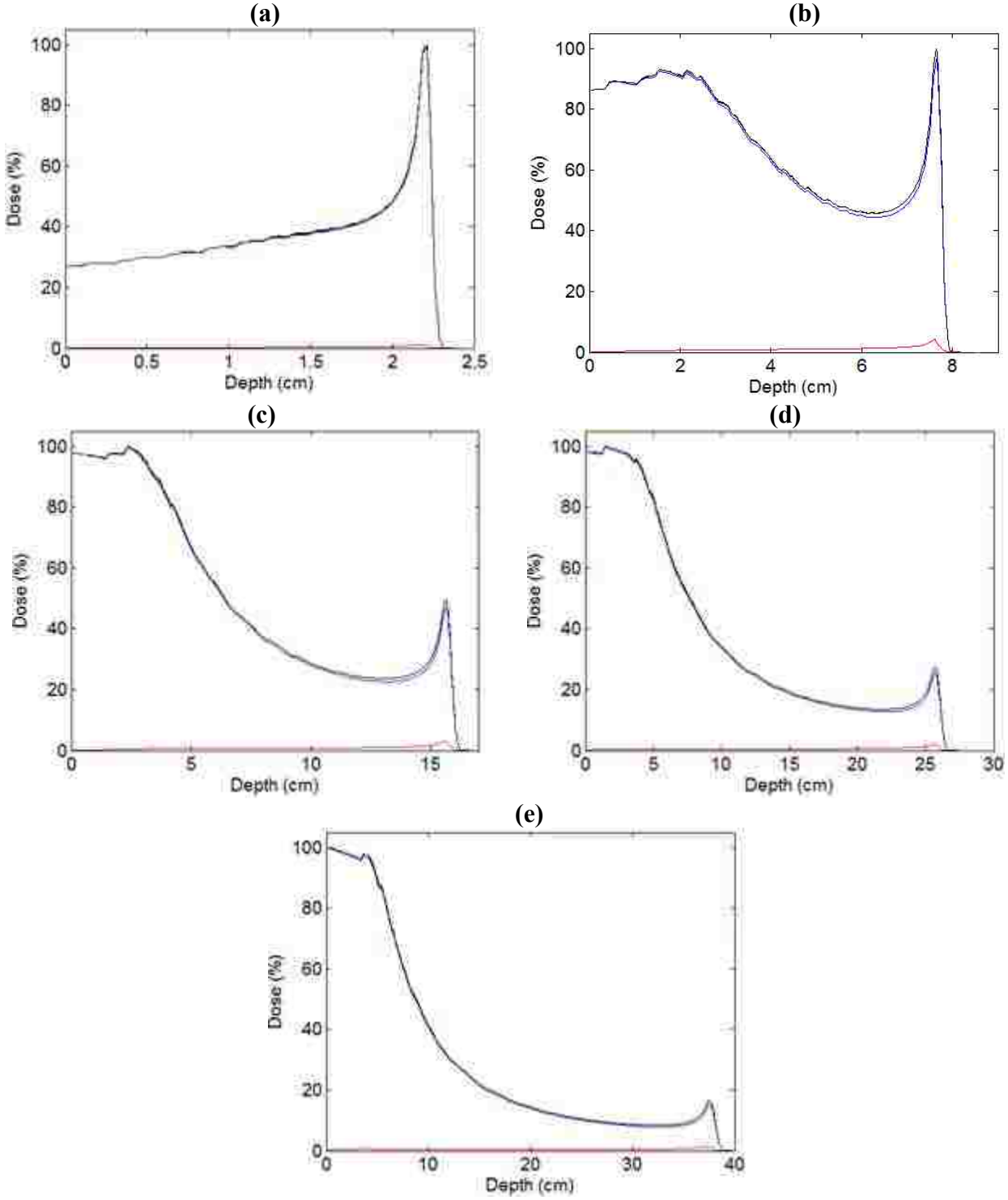

Figure C.1: Central-axis depth dose components from Levenberg-Marquardt (LM) fits to Monte Carlo (MC) data with a 1x1 mm^2 field size at energies of (a) 50, (b) 100, (c) 150, (d) 200, and (e) 250 MeV. Components shown include primary (blue) and halo (red) components of LM fit, the total LM fit (solid black), and MC data (black dashed).

C.2 Nuclear Halo Fit Lateral Profiles

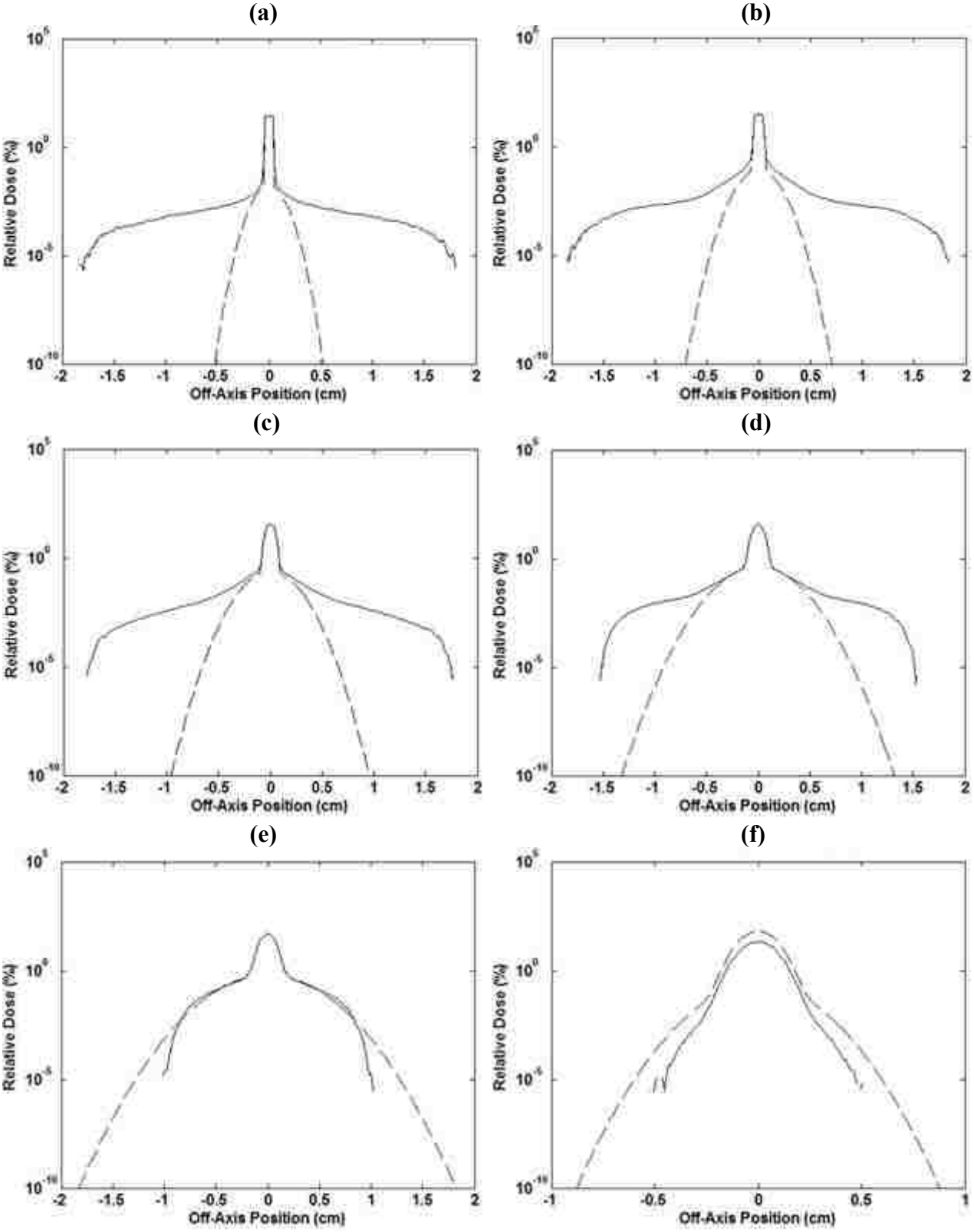

Figure C.2: Lateral profiles through 50 MeV Monte Carlo data (solid) and Levenberg-Marquardt fit data (dashed) at depths of (a) 0 cm, (b) 0.5 cm, (c) 1 cm, (d) 1.5 cm, (e) 2 cm, (f) 2.24 cm.

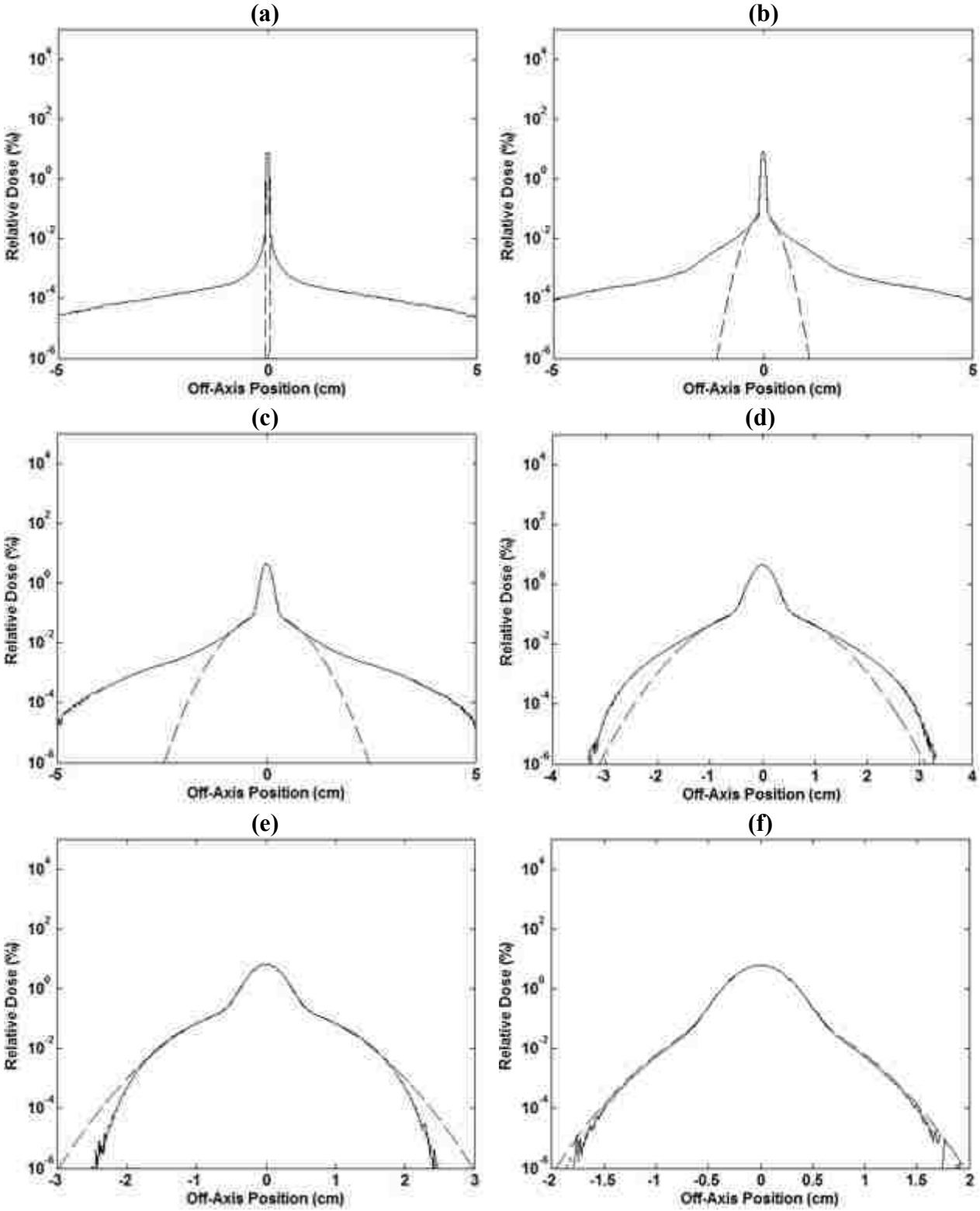

Figure C.3: Lateral profiles through 100 MeV Monte Carlo data (solid) and Levenberg-Marquardt fit data (dashed) at depths of (a) 0 cm, (b) 2 cm, (c) 5 cm, (d) 7 cm, (e) 7.5 cm, (f) 7.74 cm.

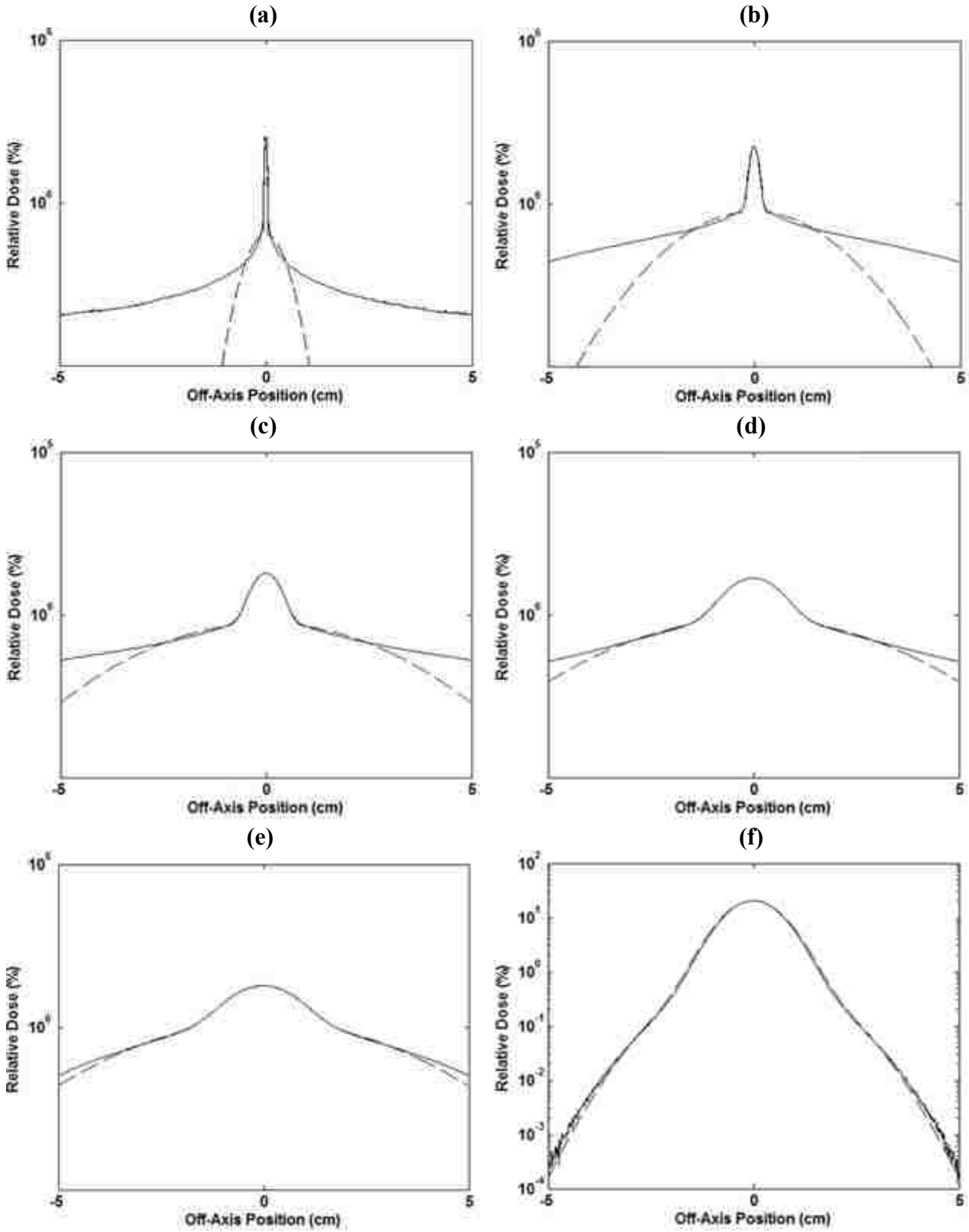

Figure C.4: Lateral profiles through 200 MeV Monte Carlo data (solid) and Levenberg-Marquardt fit data (dashed) at depths of (a) 0 cm, (b) 7 cm, (c) 15 cm, (d) 22 cm, (e) 25 cm, (f) 26 cm.

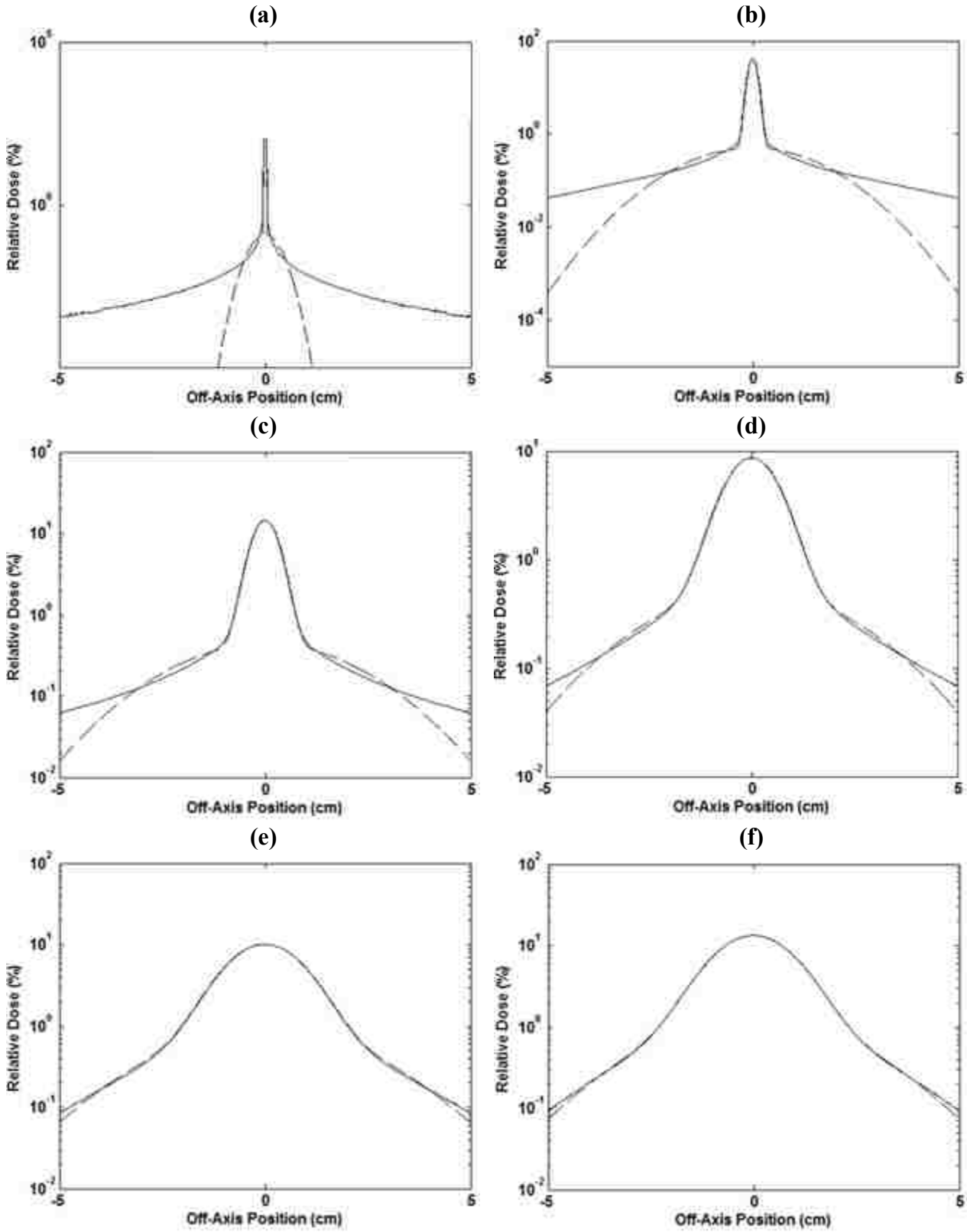

Figure C.5: Lateral profiles through 250 MeV Monte Carlo data (solid) and Levenberg-Marquardt fit data (dashed) at depths of (a) 0 cm, (b) 10 cm, (c) 20 cm, (d) 30 cm, (e) 36 cm, (f) 37 cm.

C.3 Central-Axis Data

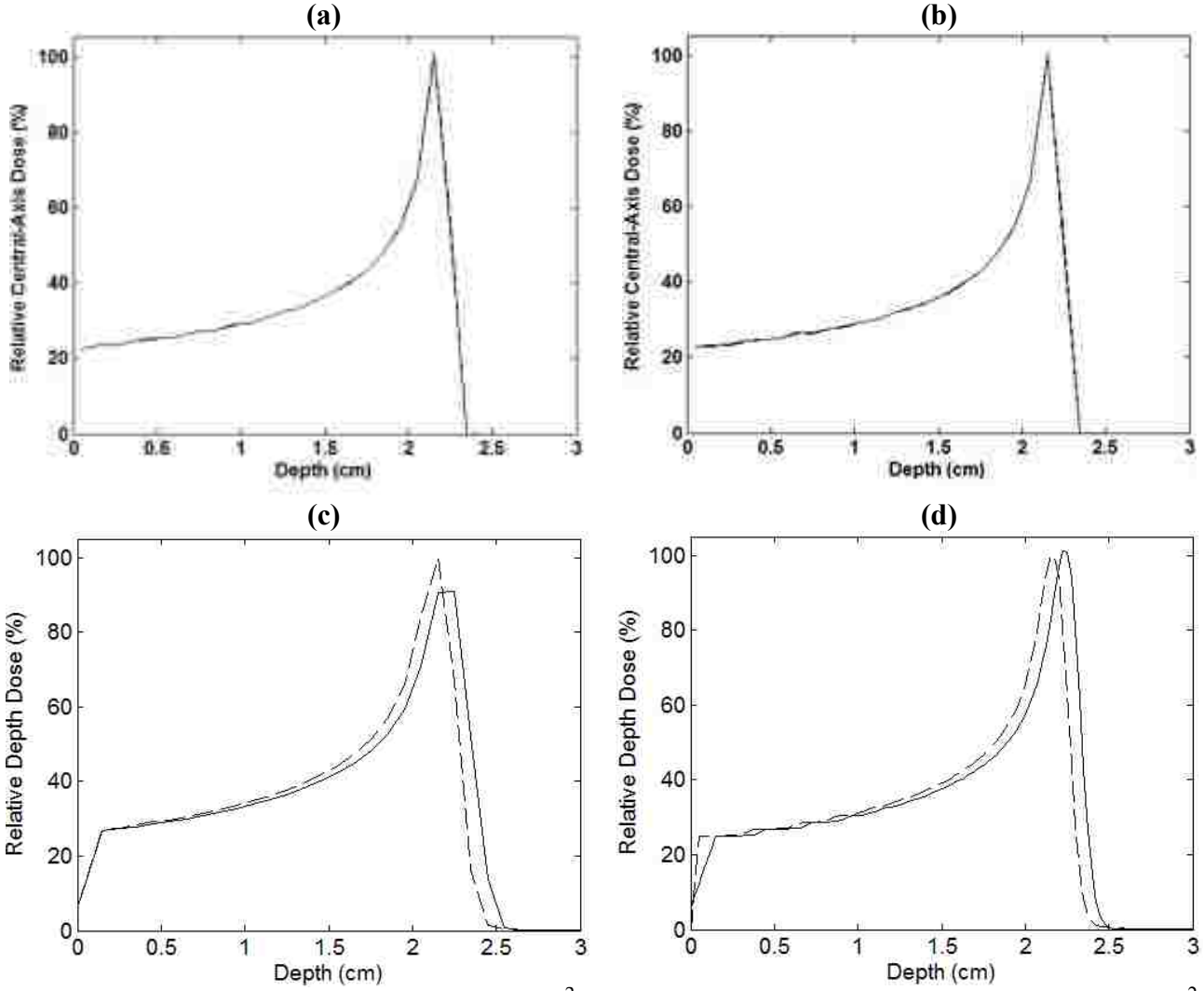

Figure C.6: Central-axis data for a 50 MeV beam with: (a) 4x4 cm^2 field size incident on a flat phantom; (b) 10x10 cm^2 field size incident on a flat phantom; (c) 4x4 cm^2 field size incident on a 45 degree oblique phantom; (d) 10x10 cm^2 field size incident on a 45 degree oblique phantom. PBA (solid) and MC (dashed) data are shown.

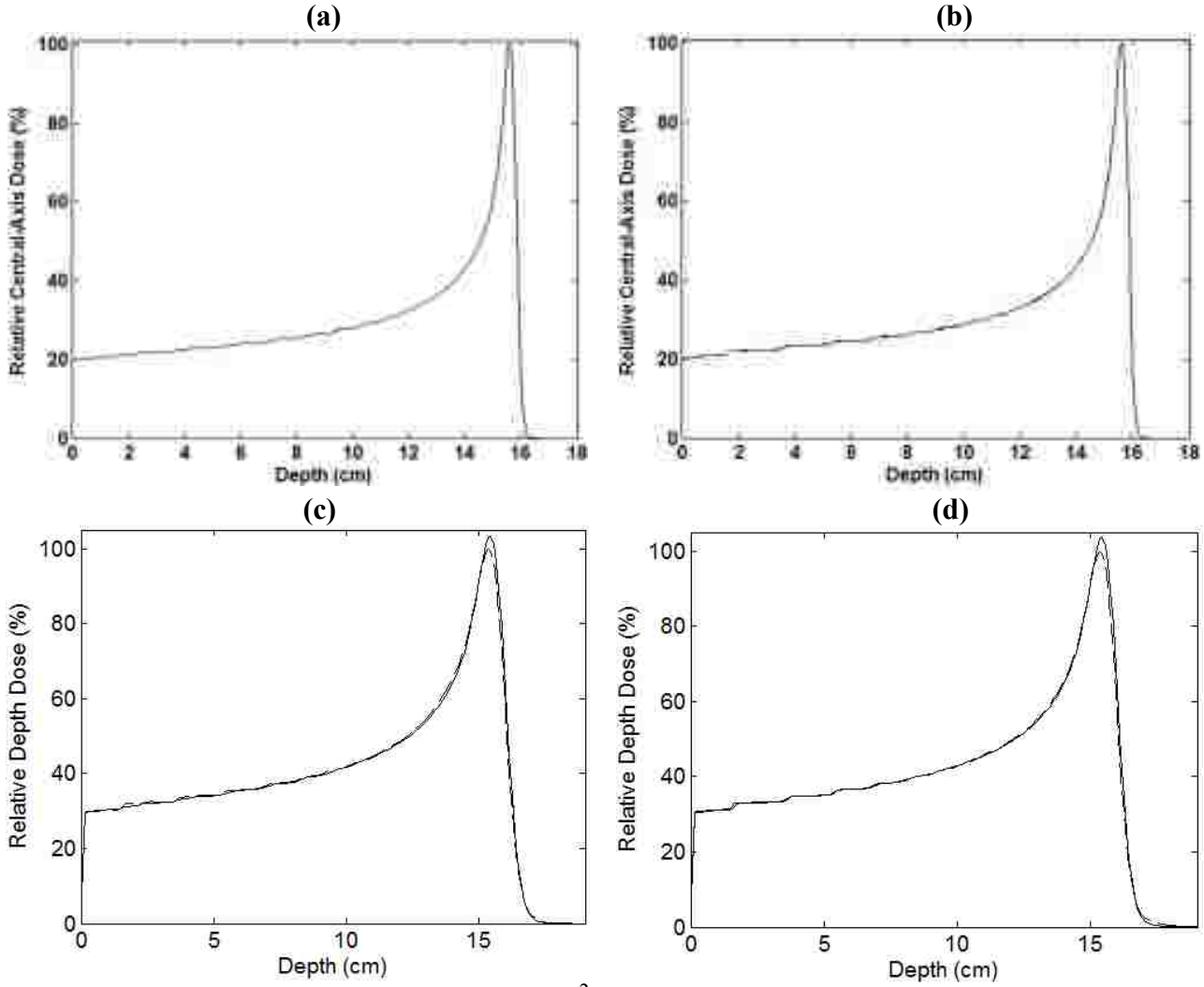

Figure C.7: Central-axis data for a 150 MeV beam with: (a) 4x4 cm^2 field size incident on a flat phantom; (b) 10x10 cm^2 field size incident on a flat phantom; (c) 4x4 cm^2 field size incident on a 45 degree oblique phantom; (d) 10x10 cm^2 field size incident on a 45 degree oblique phantom. PBA (solid) and MC (dashed) data are shown.

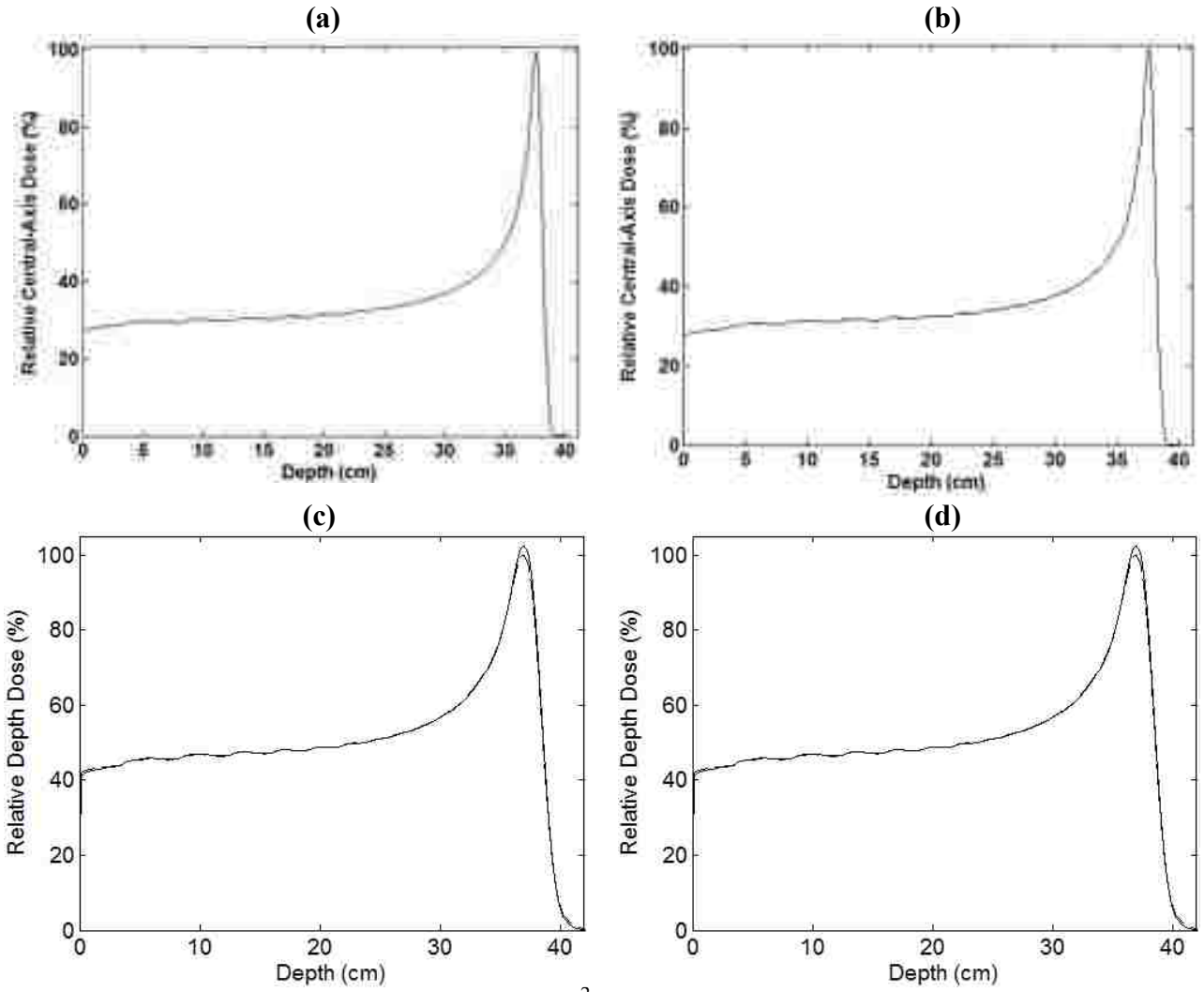

Figure C.8: Central-axis data for a 250 MeV beam with: (a) 4x4 cm^2 field size incident on a flat phantom; (b) 10x10 cm^2 field size incident on a flat phantom; (c) 4x4 cm^2 field size incident on a 45 degree oblique phantom; (d) 10x10 cm^2 field size incident on a 45 degree oblique phantom. PBA (solid) and MC (dashed) data are shown.

C.4 Lateral Profile Data

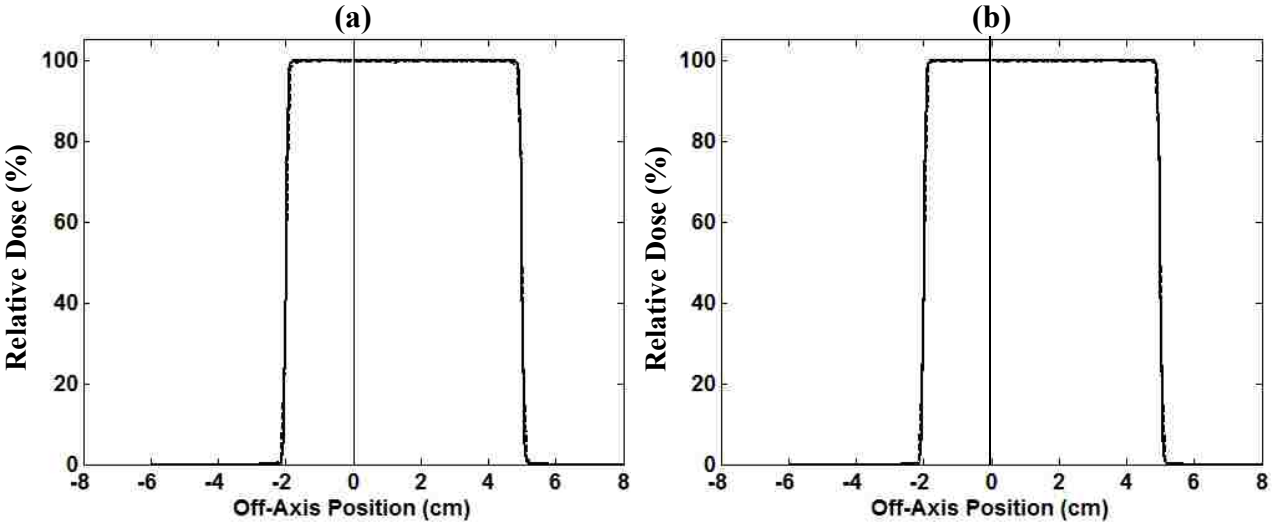

Figure C.9: Lateral profiles through flat phantom simulations from the pencil beam algorithm (solid) and Monte Carlo data (dashed) at 50 MeV. All profiles were symmetric about the central-axis; the thin vertical line in (a) and (b) indicates that the profiles shown on the left half of the line are taken through 4x4 cm^2 simulations and the profiles on the right half of the line are taken through 10x10 cm^2 simulations. Profiles are shown at depths of: (a) 80% of the maximum dose, and (b) maximum dose.

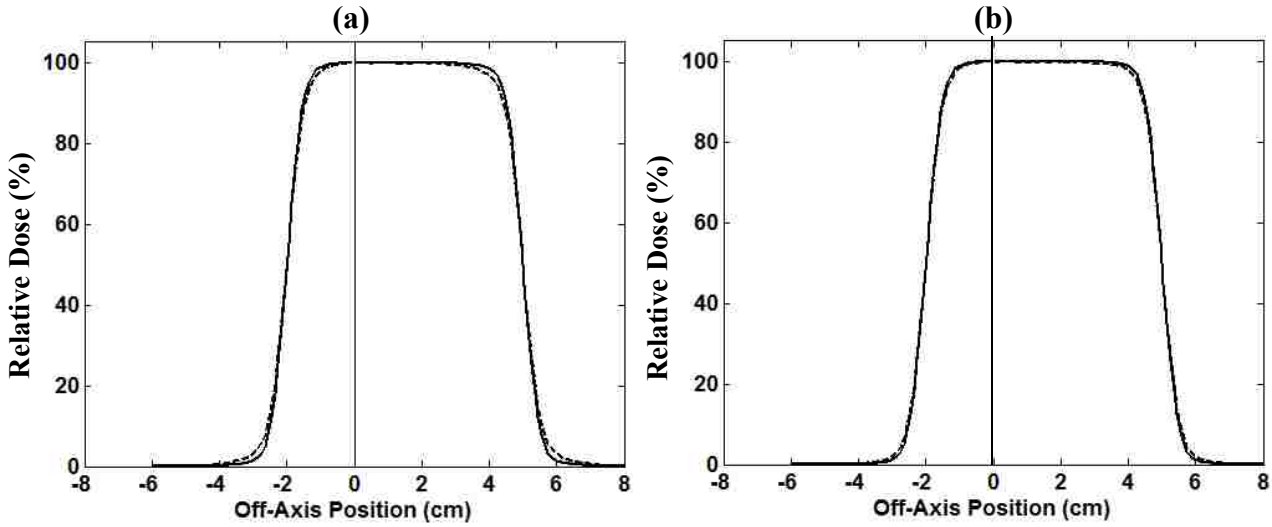

Figure C.10: Lateral profiles through flat phantom simulations from the pencil beam algorithm (solid) and Monte Carlo data (dashed) at 150 MeV. All profiles were symmetric about the central-axis; the thin vertical line in (a) and (b) indicates that the profiles shown on the left half of the line are taken through 4x4 cm^2 simulations and the profiles on the right half of the line are taken through 10x10 cm^2 simulations. Profiles are shown at depths of: (a) 80% of the maximum dose, and (b) maximum dose.

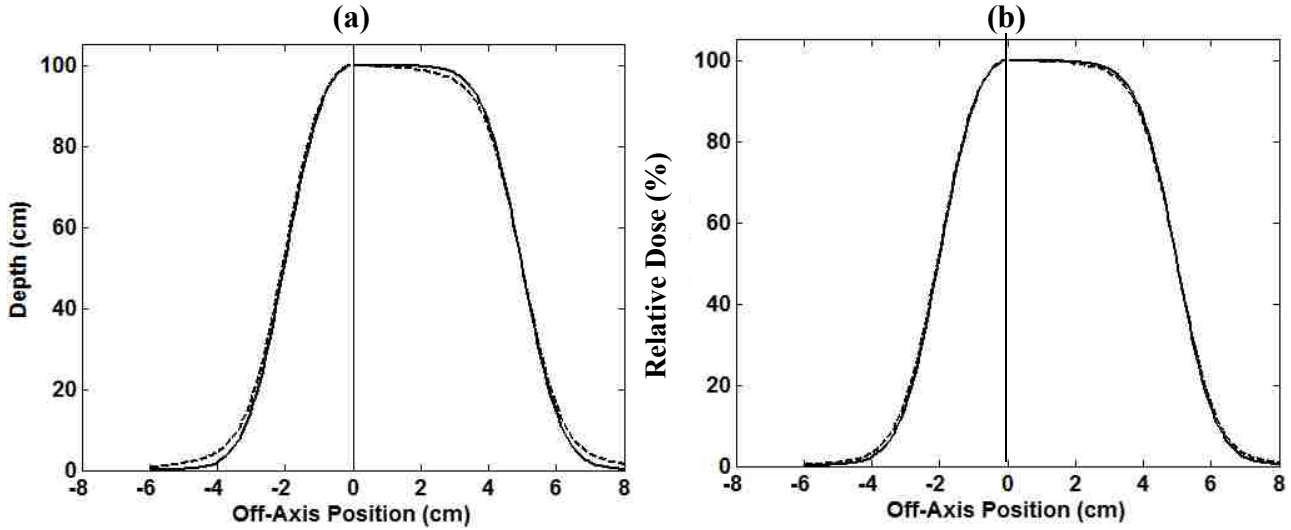

Figure C.11: Lateral profiles through flat phantom simulations from the pencil beam algorithm (solid) and Monte Carlo data (dashed) at 250 MeV. All profiles were symmetric about the central-axis; the thin vertical line in (a) and (b) indicates that the profiles shown on the left half of the line are taken through 4x4 cm^2 simulations and the profiles on the right half of the line are taken through 10x10 cm^2 simulations. Profiles are shown at depths of: (a) 80% of the maximum dose, and (b) maximum dose.

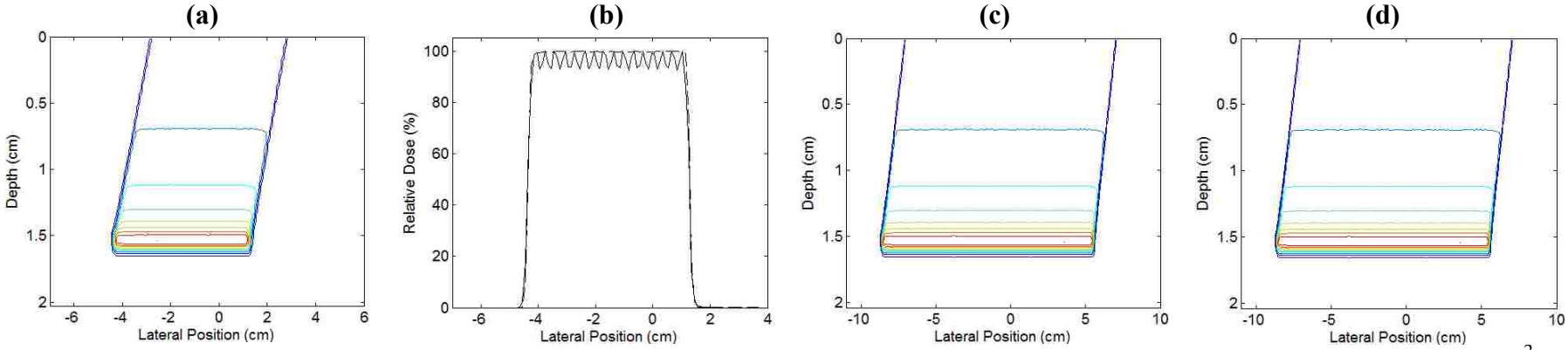

Figure C.12: Lateral profiles through the Bragg peak of a 50 MeV beam in a 45 degree oblique phantom with a field size of: (b) 4x4 cm^2, and (d) 10x10 cm^2. The dose distributions used to extract the lateral profiles are shown in (a,c).

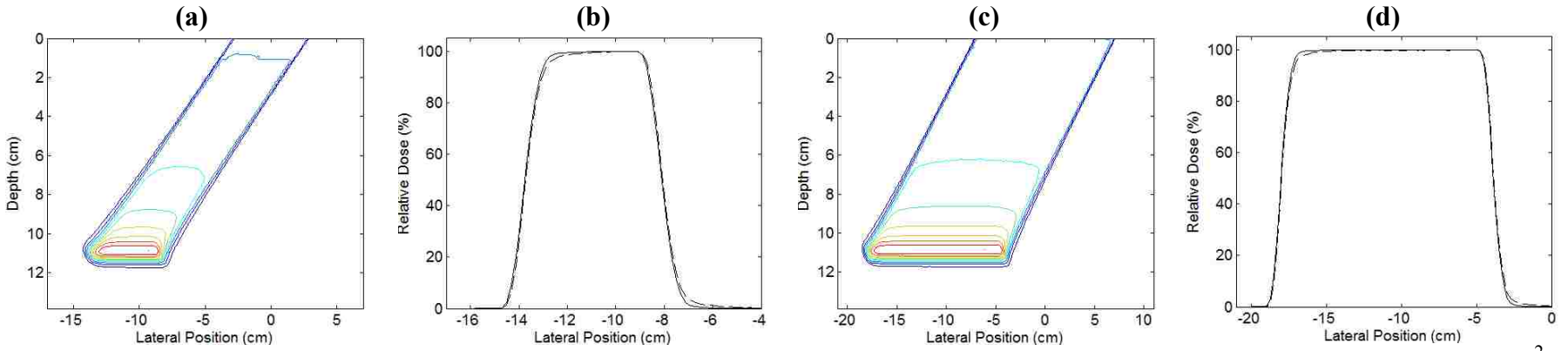

Figure C.13: Lateral profiles through the Bragg peak of a 150 MeV beam in a 45 degree oblique phantom with a field size of: (b) 4x4 cm^2, and (d) 10x10 cm^2. The dose distributions used to extract the lateral profiles are shown in (a,c).

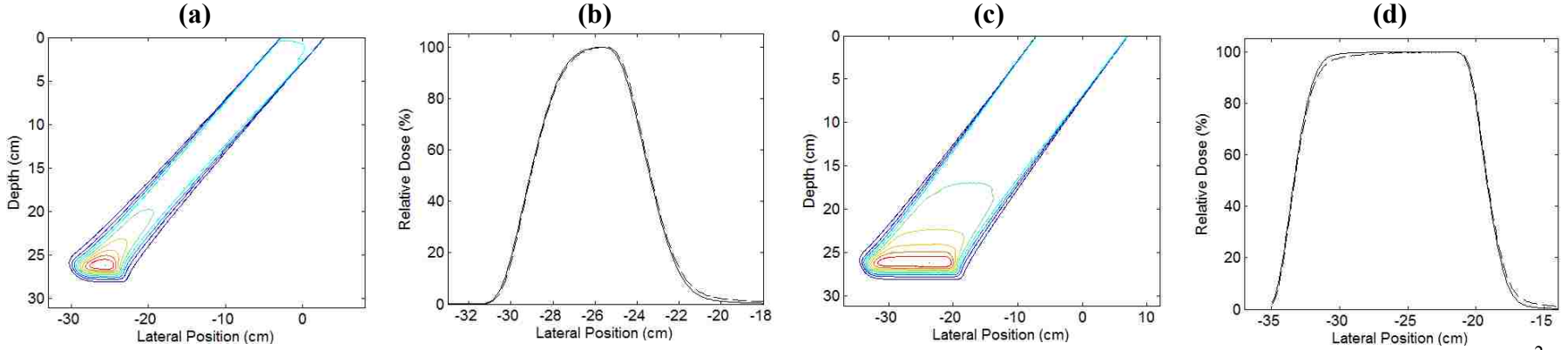

Figure C.14: Lateral profiles through the Bragg peak of a 250 MeV beam in a 45 degree oblique phantom with a field size of: (b) 4x4 cm^2, and (d) 10x10 cm^2. The dose distributions used to extract the lateral profiles are shown in (a,c).

APPENDIX D. SCATTER THEORY

The discussion on scatter theory that follows is limited in scope to Fermi-Eyges transport theory (Eyges 1948), Moliere/Hanson scatter theory (c.f. Bethe 1953, Hanson *et al.* 1951), and the Highland equation (Highland 1975). The reader is referred to these original publications for further details on these theories. Further, this section will highlight the equations that are important for this study while qualitatively presenting their significance. In the following discussion, χ is used to notate angles occurring from single scattering events and θ is used to notate angles due to multiple scatter events.

D.1 Fermi-Eyges Transport Theory

This theory was derived for multiple Coulomb scattering and therefore uses a single Gaussian for beam transport. However, the incorporation of a 'scattering power' term allows this theory to account for higher order scatter events; that is, the complexity of the scatter events are dictated by the scattering power and the Fermi-Eyges theory is used to transport these parameters. Fermi-Eyges theory is characterized by the determination of three scattering moments, which are related to the root mean square (RMS) angle of an angular distribution, a covariance term, and the RMS lateral spread of an angular distribution. All three of these moments can be calculated using equation (14) for $j = 1,2,3$. In these equations, the differential increase in RMS angle over an infinitesimally small depth, $T(E(z))$, is the scattering power of a given material and z indicates the depth at which the scatter is to be quantified. In general, the scattering power is a term that depends on both the beam energy at a given depth and the material in which the scattering occurs. Gottschalk (2010) has provided a comprehensive review of analytical scattering power formulas, some of which incorporate a single scattering correction factor for use with the formalism present in Fermi-Eyges theory. In this sense, these authors have derived parameters that account for both the central small-angle Gaussian distribution and

the slowly decaying single scattering tails to be adopted into the single Gaussian formulation of Fermi-Eyges theory.

Physically, a_o is the square of the RMS of the Gaussian angular distribution of protons, a_1 is a position-angle correlation term, and a_2 is the square of the RMS of the Gaussian spatial distribution. From these three moments the virtual source-to-surface distance (SSD) (*i.e.,* the point along the beam axis where all beam rays project back to) can be derived for a diverging beam as the quotient of the second moment to the first moment (equation (50)). The mean angle of a pencil beam can be determined from the Fermi-Eyges moments and the off-axis position *X* by equation (51). The spread about the mean angle can also be calculated from the Fermi-Eyges moments by equation (52). Further, Fermi-Eyges theory inherently accounts for the effect of every inhomogeneity and the specific location of each inhomogeneity because the integration in equation (14) sums the scatter effects for all integration steps *z'* and characterizes the effect that has on depth *z*; that is, the inclusion of the *(z-z')* term in an integral over *dz'* inherently includes these effects.

$$SSD_{vir} = \frac{a_2}{a_1} \tag{50}$$

$$\overline{\theta_x} = \left(\frac{a_1}{a_2}\right) X \tag{51}$$

$$\sigma_{\theta_X}^2 = a_o - \frac{a_1^2}{a_2} \tag{52}$$

Fermi-Eyges theory was derived for stacked semi-infinite slab geometry (as shown in Figure 2.3(b)). In this respect, Fermi-Eyges theory does not provide a result directly useful for patient inhomogeneities. However, if the incident beam is divided into a grid of smaller pencil beams, then the semi-infinite slab approximation more reliably models the surrounding material. Thus, Fermi-Eyges theory has become popular for PBAs.

D.2 Moliere / Hanson Scatter Theory

Moliere (c.f. Bethe 1953) proposed a scatter theory that has been shown to agree with measured data (Gottschalk *et al.* 1993). In Moliere theory, three terms are used to describe the scattered distribution of a beam of particles: (1) a small-angle multiple Coulomb scattering (MCS) Gaussian term, (2) a large-angle single scattering term, and (3) a correction term to account for an intermediate number of scatters (called plural scattering). The derivation of the Moliere theory of angular deflections (c.f. Bethe 1953) begins at the same starting point as the derivation of the Fermi-Eyges transport theory: the transport diffusion equation. However, rather than using the central-limit theorem to produce a Gaussian distribution as in Fermi-Eyges theory, the Moliere theory instead explicitly gives a method to calculate the limits beyond MCS events. One term, called the characteristic single scattering angle χ_c (equation (53)), accounts for collisions that occur very close to the nucleus (which causes a large scattering angle) because the nucleus is a distributed charge (not a point charge as in the Rutherford derivation). Another term in the Moliere theory, called the screening angle χ_a (equation (54)), accounts for collisions that occur far away from the nucleus (with a small scattering angle) because the nucleus is screened by electrons. Using the Fermi-Thomas model of the atom (related to equation 55) and the Fano (1954) correction for scattering from atomic electrons (equation (65)), the Moliere equations for a thin target (*i.e.,* little or no energy loss occurs in the target) are presented below.

$$\chi_{c,Thin}^2 = 4\pi N_A (\alpha \hbar c)^2 \frac{Z^2}{A} \frac{\rho\, z}{(pv)^2} \tag{53}$$

$$\chi_{a,Thin}^2 = 4\pi N_A (\alpha \hbar c)^2 G \tag{54}$$

$$G = \left(\frac{\alpha\, m_e c^2}{0.8853}\right)^2 \frac{\left[1.13 + 3.76\left(\frac{\alpha\, Z}{\beta}\right)^2\right] Z^{2/3}}{(pc)^2} \tag{55}$$

In the above equations, z is the calculation depth, N_A stands for Avogadro's number, α is the fine structure constant (1/137), Z is the atomic number and A is the atomic mass of the target material, ρ is the density of the material, $m_e c^2$ is the electron rest mass, ħ is Planck's constant divided by 2π, c is the speed of light in vacuum, and pv, pc, and β are kinematic factors related to the energy of the beam (equations (56)-(58)). The kinematic factors are related to the beam energy by

$$pv = \frac{E^2 - (m_p c^2)^2}{E} \tag{56}$$

$$\beta^2 = \frac{E^2 - (m_p c^2)^2}{E^2} \tag{57}$$

$$(pc)^2 = E^2 - (m_p c^2)^2 \tag{58}$$

where E stands for the total energy (kinetic plus rest mass) and $m_p c^2$ is the proton rest mass.

The physical interpretation of χ_c is that on average a particle will undergo only one scatter event that is greater than the angle χ_c throughout the entire target (Gottschalk *et al.* 1993). The physical interpretation of χ_a is that it is a cutoff angle for distant collisions (from the nucleus) for which there is a departure from the Rutherford law (which falls off as χ^{-4}) (Gottschalk *et al.* 1993). Equation (55) is an approximation introduced by Moliere for the electronic screening based on the Fermi-Thomas model of the atom.

Equations (53)-(58) give a library of functions to determine the final $\chi^2_{c,Thin}$ and $\chi^2_{a,Thin}$. From there, Moliere proposed a term that is the natural logarithm of the effective number of collisions in the target (equation (59)) (Gottschalk *et al.* 1993). This number can then be used to find the reduced target thickness, B (equation (60)) (Gottschalk *et al.* 1993). The characteristic *multiple* scattering angle θ_M, can then be found by equation (61). The iterative numerical

solution of B (equation (60)) can be avoided for clinical energies (3-300 MeV) by applying Scott's (1963) (equation (62)).

$$b = \ln\left(\frac{\chi_c^2}{1.167\ \chi_a^2}\right) \tag{59}$$

$$B - \ln B = b \tag{60}$$

$$\theta_M = \chi_c\sqrt{B} \tag{61}$$

$$B = 1.153 + 2.583\ \log_{10}\left(\frac{\chi_c^2}{\chi_a^2}\right) \tag{62}$$

In equations (59)-(62), we have represented χ_c and χ_a without the t*hin* to illustrate that these equations apply for any characteristic angle and any screening angle.

To adapt equations (53)-(55) to a thick target calculation (*i.e.*, in a semi-infinite slab geometry), energy loss and material dependency must be taken into account. These factors are presented in the original Moliere theory (c.f. Bethe 1953). Thus, the thick target characteristic single scattering angle is given by equation (63) and the thick target electronic screening angle is given by equation (64). In the calculation of the thick target electronic screening angle (equation (64)), the Moliere theory must be corrected for scattering from atomic electrons using Fano's (1954) correction factor (equation (65)). While Fano's original correction was only valid for a thin target, Scott (1963) extended Fano's correction factor for thick targets (equation (65)).

$$\chi_{c,Thick}^2 = 4\pi N_A(\alpha\hbar c)^2 \int_0^z \rho(z') \sum_j w_j(z') \frac{Z_j^2(z')}{A_j(z')}\left(\frac{1}{pv(z')}\right)^2 dz' \tag{63}$$

$$\begin{aligned}\ln\left[\chi_{a,Thick}^2\right] = \frac{4\pi N_A(\alpha\hbar c)^2}{\chi_{c,Thick}^2} \int_0^z \rho(z') \sum_j w_j(z') \frac{Z_j^2(z')}{A_j(z')} \\ x\left(\frac{1}{pv(z')}\right)^2 \left[\ln G_j(z') - \frac{F_j(z')}{Z_j(z')}\right] dz'\end{aligned} \tag{64}$$

$$F_j(z') = \ln\left[1130\, Z_j^{-\frac{4}{3}}(z')\left(\frac{\beta(z')}{1-\beta^2(z')}\right)^2\right] - u_j - \frac{1}{2}\beta^2(z') \qquad (65)$$

In equations (63)-(65), explicit depth dependence is included in several terms and a summation over elements of a given compound or mixture is also included (note that, for instance, A_j refers to the atomic mass of the *j*th element in the target compound). $G_j(z')$ is computed according to equation (55) by substituting Z with $Z_j(z')$ and replacing pc with $pc(z')$ and β with $\beta(z')$. The fluence for the Moliere distribution is then given by

$$f(\vartheta)\, d\vartheta = \vartheta\, d\vartheta\left[f^{(0)}(\vartheta) + \frac{f^{(1)}(\vartheta)}{B} + \frac{f^{(2)}(\vartheta)}{B^2}\right] \qquad (66)$$

where

$$f^{(n)}(\vartheta) = \frac{1}{n!}\int_0^\infty J_0(\vartheta y)\, y \exp\left(\frac{-y^2}{4}\right)\left(\frac{y^2}{4}\ln\frac{y^2}{4}\right)^n dy \qquad (67)$$

and

$$\vartheta = \frac{\theta}{\theta_M}. \qquad (68)$$

The function J_0 in equation (67) denotes a Bessel function. The first term in equation (66) is a standard Gaussian and the remaining two terms are corrections to account for large-angle scattering and plural scattering.

To find θ_M for the thick angle equations, we would again apply equations (59)-(61) using the thick target single-scattering angles in equations (63) and (64). However, this characteristic scattering angle must be used in the three-term fluence equation (equation (67)) presented by Moliere (c.f. Bethe 1953) and *cannot* be used in a Gaussian (because it was not derived to fit the form of a Gaussian). In order to take advantage of the Moliere calculation for single Gaussian transport, the Hanson *et al.* (1951) approximation is applied. The RMS width of the Hanson distribution is taken to be the width at which the total Moliere fluence falls to $1/e$ (here, *e* refers

to the natural number 2.7182…) of its maximum value; hence, the Hanson approximation provides a fitted Gaussian to the Moliere fluence distribution with a RMS width that is equivalent to the $1/e$ width of the Moliere distribution. Hanson's approximation, for the purposes of clinical dose calculation, sufficiently accounts for all three of the scatter terms included in the Moliere theory. Thus, the Hanson distribution will give an excellent description for the primary fluence of a pencil beam. Hanson's approximation is said to be within 2% of measurements (whereas Moliere theory is definitive) (Gottschalk *et al.* 1993).

The width of the Hanson angular distribution θ_H is related to the Moliere characteristic multiple scattering angle θ_M by

$$\theta_H = \theta_M \sqrt{1 - 1.2/B} \tag{69}$$

where the square root term is a factor to convert the width of the Moliere angular distribution to $1/e$ of its maximum value. The fluence for the Hanson distribution is given by

$$f(\theta)\, d\theta = \frac{1}{2\pi\, \theta_H} exp\left[\frac{-\theta^2}{2\, \theta_H}\right]. \tag{70}$$

D.3 Highland Equation

Some have regarded the task of performing a full Moliere calculation to be too complicated for practical implementation. To address this issue, Highland (1975) provided a simple parameterization of Hanson's approximation of Moliere theory which depends solely on radiation length in materials, which are contained in standard lookup tables for several materials. The thin target Highland equation is given by

$$\theta_{HL,Thin} = \frac{14.1}{pv} \sqrt{\frac{\rho z}{X_o}} \left[1 + \frac{1}{9} \log_{10}\left(\frac{\rho z}{X_o}\right)\right], \tag{71}$$

where X_o is the radiation length of the target. Gottschalk *et al.* (1993) extended this formula to thick targets by allowing *z* to become infinitesimally small and added contributions from $\theta_{HL,Thin}$

in quadrature, allowing the *pv* in the denominator to vary with depth. Thus, the Highland thick target formula is

$$\theta_{HL,Thick} = 14.1\left(1+\frac{1}{9}\log_{10}\frac{\rho z_{tot}}{X_o}\right)\sqrt{\int_0^z\left(\frac{1}{pv(z')}\right)^2\frac{\rho(z')}{Xo(z')}dz'} \qquad (72)$$

where the bracketed term in equation (71) has been taken out of the integral to serve as a correction on the entire target thickness (Gottschalk *et al.*1993). Highland theory is said to be within 5% of measurements (Highland (1975)).

VITA

John Chapman was born in Lake Charles, Louisiana, in 1984. He was raised in Westlake, Louisiana, and graduated from Westlake High School in May of 2002. Since 2004, he has taken courses at Louisiana State University, earning a Bachelor of Science in Electrical Engineering degree with a minor in mathematics and will soon complete the requirements for a Master of Science in Medical Physics degree. In the fall of 2012, he will enroll in the medical physics doctoral program at Louisiana State University. After completing his education, he hopes to pursue an academic medical physics career.